CRANFIELD UNIVERSITY

J. DANIEL SEBASTIÀ-SÁEZ

CFD MODELLING OF POST-COMBUSTION CARBON CAPTURE WITH AMINE SOLUTIONS IN STRUCTURED PACKING COLUMNS

SCHOOL OF ENERGY, ENVIRONMENT AND AGRIFOOD

PhD thesis
Academic Year: 2015–2016

Supervisor:
Professor Sai Gu
Dr. Beatriz Fidalgo-Fernández

June 2016

CRANFIELD UNIVERSITY

SCHOOL OF ENERGY, ENVIRONMENT AND AGRIFOOD

PhD thesis

Academic Year: 2015–2016

J. DANIEL SEBASTIÀ-SÁEZ

CFD modelling of post-combustion carbon capture with amine solutions in structured packing columns

Supervisor:
Professor Sai Gu
Dr. Beatriz Fidalgo-Fernández
June 2016

Abstract

The scope of the present thesis is the development of a Computational Fluid Dynamics model to describe the multiphase flow inside a structured packing absorber for post-combustion carbon capture. The work focuses mainly on two flow characteristics: the interface tracking and the reactive mass transfer between the gas and the liquid. The interface tracking brings the possibility of studying the liquid maldistribution phenomenon, which strongly affects the mass transfer performance. The development of a user-defined function to account for the reactive mass transfer between phases constitutes the second major concept considered in this thesis.

Numerical models found in the literature are divided into three scales due to the current computational capacity: small-, meso- and large-scale. Small-scale has usually dealt with interface tracking in 2D computational domains. Meso-scale has usually been considered to assess the dry pressure drop performance of the packing (considering only the gas phase). Large-scale studies the liquid distribution over the whole column assuming that the structured packing behaves as a porous medium.

This thesis focuses on small- and meso-scale. The novelty of this work lies in expanding the capabilities of the aforementioned scales. At small-scale, the interfacial tracking is implemented in a 3D domain, instead of 2D. The user-defined function that describes the reactive mass transfer of CO_2 into the aqueous MEA solution is also included to assess the influence of the liquid maldistribution on the mass transfer performance. At the meso-scale, the Volume of Fluid method for interface tracking is included (instead of only the gas phase) to describe flow characteristics such as the liquid hold-up, the interfacial area and the mass transfer.

At the theoretical level, this model presents the particularity of including both a mass and a momentum source term in the conservation equations. A comprehensive mathematical development shows the influence of the mass source terms on the momentum equation.

Keywords

Carbon capture and storage; post-combustion; structured packing; CFD; VOF; reactive mass transfer; multiphase flow, verification and validation.

Contents

List of Figures

List of Tables

List of Abbreviations

CCS	Carbon Capture and Storage
CSF	Continuum Surface Force model
CFD	Computational Fluid Dynamics
CPU	Central Processing Unit
EOR	Enhanced Oil Recovery
FDM	Finite Difference Method
FEM	Finite Element Method
FVM	Finite Volume Method
GCI	Grid Convergence Index
GHG	Greenhouse Gas
GWP	Global Warming Potential
HPC	High Performance Computing
IGCC	Integrated Gasification Combined Cycle
LBM	Lattice Boltzmann Method
MEA	Monoethanolamine
MDEA	Methyldiethanolamine
MOF	Metal-Organic Framework
NGCC	Natural Gas Combined Cycle
PDE	Partial Differential Equation

REU	Representative Elementary Unit
SEM	Scanning Electron Microscope
TEA	Triethanolamine
UDF	User-Defined Function
VLE	Vapour-Liquid Equilibrium
VOF	Volume of Fluid

Acknowledgements

I would like to express my sincere thanks to my supervisor Prof. Sai Gu for his guidance, encouragement and support during my PhD study at Cranfield University.

I am also grateful for the financial support from the Engineering and Physical Sciences Research Council (EPSRC) and Cranfield University for the complete funding of my studies.

Finally, I would like to thank my parents Juan Antonio Sebastià Hernández and María José Sáez Paredes, for everything.

Nomenclature

Latin characters

A_{eff}	Effective area (m^2)
A_{spf}	Specific area of the structured packing ($m^2 \cdot m^{-3}$)
c	Mass concentration ($kg \cdot m^{-3}$)
D	Mass diffusivity ($m^2 \cdot s^{-1}$)
E	Enhancement factor (-)
$\vec{F}$	Force (N)
F_s	Safety factor Richardson extrapolation (-)
$\vec{g}$	Gravity ($m \cdot s^{-2}$)
h	Grid spacing (m)
h_l	Liquid hold-up (-)
$\vec{i}, \vec{j}, \vec{k}$	Unit vectors in the Cartesian coordinate system
J	Mass flux ($kg \cdot m^{-2} \cdot s^{-1}$)
k_l, k_g	Mass transfer coefficients ($m \cdot s^{-1}$)
K_f	Second order reaction rate constant ($m^3 \cdot mol^{-1} \cdot s^{-1}$)
$\mathscr{L}$	Length of the liquid film (m)
$\dot{m}$	Mass flow rate ($kg \cdot s^{-1}$)
m	Mass (kg)

$\vec{n}$	Unit normal vector
p	Pressure (Pa)
P_m	Molecular weight ($g \cdot mol^{-1}$)
r	Reaction rate ($mol \cdot m^{-3} \cdot s^{-1}$)
$\vec{r}$	Position vector
R	Convergence ratio (-)
S_{mass}	Mass source term ($kg \cdot m^{-3} \cdot s^{-1}$)
S_μ	Momentum source term caused by the variation in viscosity ($N \cdot m^{-3}$)
S_σ	Momentum source term caused by the surface tension ($N \cdot m^{-3}$)
t	Time (s)
$\vec{t}$	Unit tangent vector
T	Temperature (K)
$\vec{v}$	Velocity vector ($m \cdot s^{-1}$)
V	Volume (m^3)
u, v, w	Velocity components in the Cartesian coordinate system ($m \cdot s^{-1}$)
x_i	Mole fraction (-)
x, y, z	Cartesian coordinate directions

Greek characters

α	Volume fraction $(-)$
δ_l	Liquid film thickness (m)
ε	Packing porosity (-)
θ	Contact angle ($^\circ$)
κ	Interface curvature (m^{-1})
μ	Dynamic viscosity ($Pa \cdot s$)
ρ	Density ($kg \cdot m^{-3}$)
σ	Axial stress ($N \cdot m^{-2}$)

τ	Shear stress ($N \cdot m^{-2}$)
φ	Inclination angle over the vertical direction (°)

Subscripts

g	Gas phase
int	Interface
l	Liquid phase
M	Refers to aqueous amine solution
$wall$	Refers to the packing surface
W	Refers to pure water

Dimensionless quantities

Ha	Hatta number
Re	Reynolds number
We	Weber number

Other symbols

∇	Nabla Operator

Chapter 1

Introduction

This chapter begins with a brief note on the concept of Carbon Capture and Storage (CCS) and the description of the different technologies available with a special focus on amine-based post-combustion CCS, which is the object of the present work. It also establishes the main scope of the thesis, the elements of novelty therein, and the progress of the research. The structure of the thesis, including a summary of each chapter follows. The chapter closes with the list of the journal articles produced.

1.1 Carbon Capture and Storage

Several strategies are being currently developed to mitigate harmful emissions to the atmosphere: the use of renewable energies (biomass, geothermal, wind and tidal power, hydraulic, etc.), the improvement of the efficiency of the current power generation systems, the change of the population habits and CCS [1]. At the present time, the latter represents the most attractive option to reduce the carbon emissions to the atmosphere [2]. Renewable energies would be the final zero-emission solution, but these technologies are still at an early stage of development and their costs cannot compete with conventional

energy resources [3–5]. At the same time, the world's population is rapidly increasing, as well as the number of emerging economies. All this leads to a fast growth in the energy demand around the globe. Currently, up to 85% of the global energy demand is provided by fossil fuels and the forecasts are that this trend is going to continue in the forthcoming decades due mainly to the abundance of fossil fuels, their high energy density and the dependence of modern society economy on these energy resources [6–8]. The use of fossil fuels yields large amounts of CO_2 as waste product. Consequently, the CO_2 concentration in the atmosphere has noticeably increased from 280 ppm at the beginning of the industrial era (c. 1750) to 390 ppm (c. 2010) [9]. Although carbon dioxide is not the greenhouse gas (GHG) with the highest global-warming potential (GWP), it constitutes the largest amount of emissions compared to other GHGs, such as methane or hydrofluorocarbons. With this scenario, and the fact that fossil fuels are going to continue playing an important role in power generating in the foreseeable future (with carbon representing 30% of the total energy production), a prominent position is given to the development of CCS in order to meet the UK target of reducing GHG emissions by 80% (at the 1990 base level) in 2050 [10, 11].

CCS is the industrial process that deals with the separation of CO_2 at large industrial sources such as power plants, its transport by shipping or through pipelines and finally its storage in convenient geological formations [12–14] or its use for Enhanced Oil Recovery (EOR) [15, 17–21, 126].

Three different strategies exist in order to decrease carbon dioxide emissions into the atmosphere: pre-, post-combustion carbon capture and oxy-fuel technology [22–24]. Pre-combustion consists in the removal of carbon from the fuel before its combustion [25,26]. This process is based on the gasification of the fuel, which renders carbon dioxide and hydrogen as products. CO_2 can be separated hereafter using physical absorption due to the big CO_2 partial pressure under these conditions. Pre-combustion CCS is normally inte-

grated within IGCC power plants [27, 28]. In conventional combined cycles the residual heat from the combustion, which otherwise would be emitted to the atmosphere, is used to produce steam to run a turbine, hence providing extra power. At the same time, the syngas produced during the gasification must undergo a cooling process before the separation of its carbon dioxide, which produces an extra amount of steam the energy of which can also be used to run the turbine. Hydrogen is burnt afterwards in the conventional way, resulting in power and water, the latter being easily manageable [29]. Oxy-fuel technology consists in burning the fuel in an almost pure oxygen atmosphere [30–32]. Cryogenic processes are used to separate the oxygen from air, which results in a substantial energy penalty. Such conditions in the combustion give a mixture of carbon dioxide and water as the sole products of the reaction. Therefore, the CO_2 can be simply removed by physical separation processes such as condensation. The separation technology to be used is, in this way, simpler than in pre- and post-combustion CCS since it does not require any chemical solvent. Other advantages of this technology are the small size of the equipment and the possibility of being retrofitted to existing power plants. Post-combustion carbon capture involves the removal of carbon dioxide from the flue gas after the combustion has taken place in the conventional way [33–42]. The most common post-combustion processes are: adsorption, cryogenic separation, membrane absorption and physical and chemical absorption. Adsorption consists in the attachment of the carbon dioxide molecules to the surface of solid materials such as alumina or zeolites. MOFs are the latest advance in this field [43–49]. However, the most common method for post-combustion remains the reactive absorption by means of amine solutions. The amine scrubbing patent dates from 1930, but it was first evaluated in 1991, when it began replacing limestone slurry scrubbing. It is expected to become the main carbon capture emissions reduction technology by 2030 [50].

A post-combustion facility consists of two columns: the absorber and the stripper, i.e.

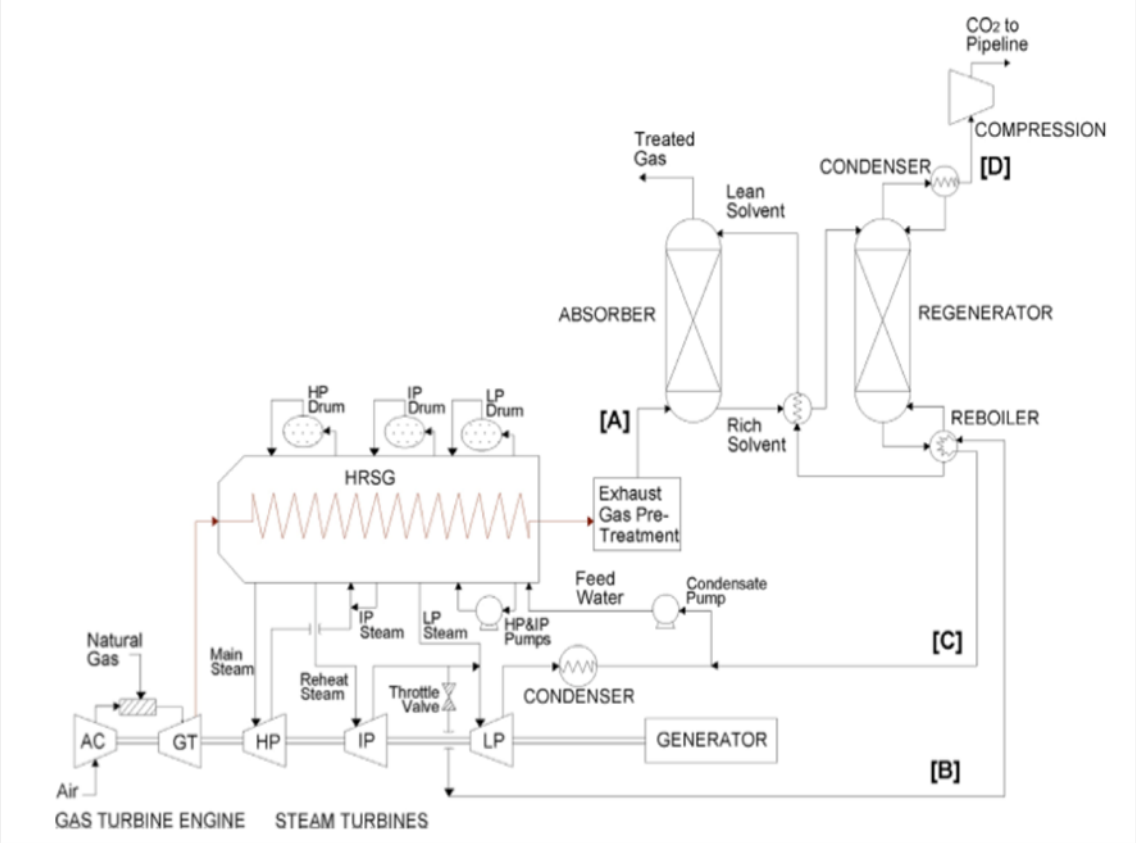

Figure 1.1: Schematic of an integrated NGCC and post-combustion CCS facility [51].

the latter also known as regenerator. Figure 1.1 shows a schematic of an integrated Natural Gas Combined Cycle (NGCC) power plant with post-combustion amine scrubbing, where both columns and their auxiliary equipment can be observed. The absorber is filled with either random or structured packing materials, the latter being preferred due to a previously demonstrated smaller pressure loss and better separation efficiency compared to random packings [52]. The flue gas coming from the combustion chamber is injected through the bottom of the reactor whereas the aqueous amine solution is poured at the top of the column. MEA (monoethanolamine, C_2H_7NO), MDEA (methyldiethanolamine, $C_5H_{13}NO_2$) and TEA (triethanolamine, $C_6H_{15}NO_3$) are the most common chemicals used for this purpose. Both phases, gas and liquid, run in counter-current configuration, com-

ing into contact and giving way to an absorption process enhanced by the occurrence of the chemical reaction. The output from the absorber is a CO_2-rich amine solution and a carbon-free flue gas ready to be emitted to the atmosphere. At this stage, the loaded amine solution enters the stripper, where it is regenerated applying steam, which breaks the weak bonds between the carbon dioxide and the amine. The regeneration of the solvent accounts for between 60% and 80% of the total cost of post-combustion CCS by chemical absorption and constitutes its main drawback [53, 54].

Despite the energy penalty, chemical absorption has a big potential to be applied for carbon capture due to its maturity and its suitability to treat large amounts of flue gas with a low carbon dioxide concentration as it happens in the case of NGCC power plants. Proof of this is the opening of the Boundary Dam Integrated Carbon Capture and Storage Demonstration, owned by SaskPower, in 2014. This project represents the first chemical absorption CCS plant at industrial scale and, at the moment of its commissioning, it was working at a capacity of 2300 tonnes/day of CO_2, which were being pumped into Cenovus Energy's EOR pipeline in Saskatchewan (Canada) [55–58].

1.2 Thesis subject and objectives

The scope of the present thesis is to develop a CFD model capable of describing the key parameters needed to characterise the reactive mass transfer that takes place between the liquid and the gas phases within a post-combustion structured packing column for CCS. The model will take into account both the mass transfer due to the absorption and the kinetics of the CO_2-MEA chemical system. Hydrodynamic features such as liquid hold-up, effective area and pressure drop, which highly influence the absorption performance of the process, will be also considered. Once the model is fully developed, it can be used as a design tool in order to either select the most suitable packing for a particular column

or to develop new geometries.

Multiphase flow occurs in a wide spectrum of industrial applications ranging from spray drying, pneumatic transport, fluidised beds, free surface flows and in general any kind of flow involving two or more immiscible fluids, which can also include solids. The analysis of these multiphase flows can be tackled in three ways: by means of experimental work, with theoretical equations or using numerical models. Occasionally, it is possible to run tests with full industrial scale facilities but in most cases smaller size lab-scale devices are used, making numerical and theoretical studies a necessity in order to complement the analysis and to extrapolate the results to full scale. Models for multiphase flows are normally used to analyse flow characteristics that cannot be assessed using experimental techniques. In the case of chemical absorption in structured packings, numerical models can be used to quantify aspects such as liquid film thickness and velocities, concentration profiles of any particular chemical species within the liquid film, dry and wet pressure drop of the packing, liquid holdup, liquid spreading and maldistribution and interfacial area per unit volume of packing. All these features would be practically impossible to analyse inserting probes into the experimental devices without interfering with the flow.

However, the current capacity of modern computers makes it impossible to capture every detail of the flow in a single, full-scale simulation. The numerical study should be then divided into three scales (e.g. small-, meso- and large-scale), the results of which can be used to feed one another [59, 60]. A detailed description of the three scales approach is given in Chapter 2, along with a specific analysis of their capabilities.

In this thesis, the numerical study of structured packing reactors will be also divided into three scales to assess the aforementioned aspects of the flow. The model describes the formation and evolution of a multicomponent liquid film over the solid wall of the structured packing along with its interaction with the gas flow in terms of hydrodynamics and chemical absorption. The commercial software ANSYS® Fluent v.14.0 is used to

run the simulations. A subroutine (i.e. also known as user-defined function or UDF) written in C programming language is developed to account for the other specifics of the flow that are not considered in the general code of the software. The main body of the UDF is dedicated to the implementation of the mass source terms that describe the mass transfer due to absorption first and the peculiarities of the CO_2-MEA chemical system after. Therefore, the reactive absorption of CO_2 into the liquid solution is modelled according to a particular rate of creation of mass per unit time and per unit volume in each computational cell. The source terms are applied to the interface between the fluids, being the component diffused into the bulk of the liquid after the absorption. Hereafter, extra source terms are applied to account for the consumption of the reactants and the creation of products of the chemical reaction between the carbon dioxide and the amine solution. In addition, the UDF is further used to implement velocity profiles at the gas inlet. The purpose of this is to avoid numerical instabilities caused by a sharp transition in the velocity values at the interface cells.

The present thesis is therefore dedicated to the development of the UDF and the analysis of the subsequent results obtained by its application. Specially, the analysis of the results will focus on the following aspects:

- The irregular development of the falling liquid film at small-scale (i.e. liquid maldistribution), giving place to the formation of droplets and rivulets that affect the amount of solid area actually covered by the liquid phase.

- The creation/consumption of the reaction products/reactants, with special focus on the evolution of the concentration profiles of the different species and the concentration at outlet conditions.

- The correct representation of the tendencies describing the liquid hold-up and the

interfacial area as a function of the liquid load over a section of commercial structured packing material.

- The interaction between the different parameters involved in the process: liquid load, liquid viscosity, flow configuration, gas pressure, gas velocity, solid-liquid contact angles, etc.

1.3 Elements of novelty

The present work aims at introducing the following new results regarding small- and meso-scale CFD modelling:

- Regarding small-scale, a comprehensive literature survey has shown that the current state of the modelling process of falling liquid films has a special focus on the hydrodynamics. In most of the published work so far, the tracking of the interface between the gas and the liquid phases is often restricted to 2D studies and even a smaller amount of work is done regarding small 3D plane geometries that cannot entirely feature the particularities of the flow within actual structured packing materials. Regarding reactive mass transfer, a couple of papers have been found dealing with the implementation of a generic second order reaction but restricted to a 2D computational domain. This thesis extends the implementation of the reactive absorption process to a 3D geometry, which makes it possible to further study the effect of important features such as liquid maldistribution.

- At meso-scale, the articles found deal mainly with the pressure drop per unit length of the column in real sections of structured packing material. The gas-liquid flow is not relevant as the simulations do not track the interface between the fluids and its implications, e.g. effect on the absorption performance. In this thesis, the tracking

of the interface is extended to meso-scale, showing liquid maldistribution and liquid hold-up.

- The present work also presents the novelty of including simultaneously both a mass and a momentum source term in the conservation equations. The mathematical development of the conservation equations solved in this work is included in Chapter 3. The conclusion is that the mass source term represents an additional source of momentum in the Navier-Stokes equations.

- There is a lack of literature regarding systematic grid convergence studies for multiphase flow simulations. This thesis presents a grid convergence study based on the Richardson extrapolation. Experimental data available in the literature for comparison and validation is scarce hence the importance of carrying out a systematic grid convergence assessment that proves the reliability of the model.

In short, the current thesis aims at presenting an integral CFD analysis of the chemical absorption process in an amine-based, post-combustion CCS facility with structured packing columns; presenting some capabilities that have not been explored in the literature yet.

1.4 Progress of the research

The research began with the familiarisation with the CCS process, the technologies available and the kinetics of the reaction between the carbon dioxide and the amine solutions. Regarding the modelling, the different strategies used hitherto and their limitations were investigated (i.e. the three-scale strategy).

Some preliminary results were obtained using simple geometries, reproducing the results already reported in the literature about the evolution of the wetted area as a function

of the liquid load over a simple inclined metallic plate. The research followed with the development of the UDF. A substantial effort was dedicated to the proper understanding of the lying structure of a UDF and its macros. First of all, the non-reactive mass transfer theory was implemented in the UDF, giving the possibility of analysing it as a function of the liquid load and the wetted area. This analysis gave the first publishable results. The study went on with a parametric analysis of the evolution of liquid films in 3D geometries and the interaction with the surrounding gas phase. Thereupon, the reaction kinetics were also studied and incorporated in the code with the appropriate simplifications. This part of the study was focused on the obtention of the concentration profiles of the species and the enhancement factors that result from the application of chemical absorption with respect to non-reactive absorption. The parametric analysis and the implementation of the reaction kinetics were worth two more publications that were effectively available to the public in the middle and final months of 2014 respectively. Hereafter, the study proceeded to meso-scale analysis, where also the Volume of Fluid (VOF) method was included to track the interface between the fluids. This brought the possibility of studying features of the flow that could not be analysed so far with the single-phase simulations found in the literature. Such flow characteristics include the liquid hold-up and the amount of contact area between both gas and the liquid phases. A simple analysis of non-reactive mass transfer was also carried out using constant values for the mass source terms but the simulations proved to be quite computationally expensive. The results were compiled in another article.

Finally, during the PhD period, synergies with other research groups from across the UK have been developed, fruit from an active networking activity and participation in the UK CCS Research Centre meetings.

1.5 Structure of the thesis

The thesis is organised in nine chapters and an appendix. The appendix shows the UDF used to perform the calculations. The first four chapters present the foundations of the thesis:

- Chapter 1 introduces the context of the PhD project, describing the technology of amine-based post-combustion CCS. The chapter also highlights the objectives of the project, its elements of novelty, the progress during the three years period of the PhD. A list of the publications produced in this work is also given at the end of Chapter 1.

- Chapter 2 constitutes the literature survey. The aforesaid three scales strategy for the modelling of the structured packing column is further explained, showing the results obtained by previous authors and identifying the gaps and limitations. The chapter also presents a review of the different approaches found in the literature to describe the kinetics of the reaction between the carbon dioxide and the amines as well as other considerations that should be included in the UDF such as the absorption theory and correlations used for the solubility and diffusivity of carbon capture in water/amine mixtures.

- Chapter 3 develops the mathematics associated to the model. The chapter begins with the derivation of the conservation equations used in this model, highlighting the appearance of the additional momentum source term caused by the presence of the reactive absorption mass source term. The chapter follows with the mathematical description of the mass source terms themselves and the pressure drop along the column.

- Chapter 4 includes details on the verification and validation of the present model.

Verification is assessed by means of a grid convergence study for several flow parameters such as velocity, pressure, film thickness and interfacial area. Validation is carried out using experimental data available in the literature.

The following chapters present the results obtained with the model. They correspond to the four journal papers that the present thesis has produced plus the conclusions and final considerations:

- Chapter 5 focuses on the hydrodynamics at small-scale and also presents some results about non-reactive mass transfer. The interface tracking in a small metallic inclined plate is shown and compared with the results reported in the literature in terms of wetted area and velocity profiles. The effect of surface texture of the plate and liquid viscosity on the wetted area is also assessed. Non-reactive mass transfer is implemented and validated against theoretical and experimental correlations.

- Chapter 6 extends the results previously obtained regarding the non-reactive mass transfer. It presents the influence of liquid viscosity, gas pressure, gas velocity, flow configuration, plate textures and contact angles on the mass transfer rate.

- Chapter 7 includes the reactive mass transfer for the CO_2-MEA in a 3D computational domain. It presents the results for the concentration profiles within the liquid film and the quantification of the enhancement that the presence of the reaction causes in the absorption rate.

- Chapter 8 focuses on meso-scale. Dry pressure calculations are obtained and compared to those reported in the literature. The liquid phase is introduced afterwards to assess the liquid hold-up and the effective area over the structured packing. The effects of liquid viscosity and contact angle are also considered.

- Chapter 9 presents the conclusions and the final considerations regarding the capabilities of the application of CFD to structured packing columns. This final chapter closes with the recommendations for future work.

1.6 List of publications

The research presented in this thesis has produced the following journal articles, which correspond to the aforementioned chapters 4, 5, 6, and 7:

1. Sebastia-Saez, D., Gu, S., Ranganathan, P. and Papadikis, K. 2013. 3D modelling of hydrodynamics and physical mass transfer characteristics of liquid film flows in structured packing elements. *International Journal of Greenhouse Gas Control*, 19, pp. 492–502.

2. Sebastia-Saez, D., Gu, S., Ranganathan, P. and Papadikis, K. 2014. Micro-scale CFD study about the influence of operative parameters on physical mass transfer within structured packing elements. *International Journal of Greenhouse Gas Control*, 28, pp. 180–188.

3. Sebastia-Saez, D., Gu, S. and Ranganathan, P. 2014. Volume of fluid modelling of the reactive mass transfer of CO_2 into aqueous amine solutions in structured packed elements at micro-scale. *Energy Procedia*, 63, pp. 1229–1242.

4. Sebastia-Saez, D., Gu, S., Ranganathan, P. and Papadikis, K. 2015. Micro-scale CFD modelling of reactive mass transfer in falling liquid films within structured packing materials. *International Journal of Greenhouse Gas Control*, 33, 40–50.

5. Sebastia-Saez, D., Gu, S., Ranganathan, P. and Papadikis, K. 2015. Meso-scale CFD study of the dry pressure drop, liquid hold-up, interfacial area and mass trans-

fer of structured packing materials. *International Journal of Greenhouse Gas Control*, 42, 388–399.

This work has also been presented at the International Conference of Greenhouse Gas Technologies (GHGT-12), held in Austin (TX) from October 6th to 9th, 2014.

Chapter 2

Literature Review

This chapter presents a critical discussion about the previous studies found in the literature regarding CFD applied to post-combustion CCS in order to find the potential gaps in the research. Information about how to tackle the modelling is provided by discussing the three scales approach, highlighting their capabilities and limitations.

Since one of the novelties of this work is to implement the reaction kinetics of the CO_2-MEA system and to study its association with liquid maldistribution, it is necessary to discuss the different approaches found in the literature regarding the chemistry of reactive amine absorption. Therefore, a review of the reaction kinetics studies found in the literature is also given, emphasising on how to implement them on the CFD simulations.

2.1 Multiphase CFD modelling

Many examples of multiphase flows can be found in technological applications, including:

- Bubbly flow reactors: where bubbles are used to enhance the mixing of the reactants. Other examples of this type of flow include distillation columns, heat transfer problems (liquid getting in contact with a hot surface hence removing heat by phase

change), or more technologically advanced applications such as reducing viscous drag in marine vehicles.

- Droplet flow: such as those encountered in industrial dryers to produce powder materials.

- Slug flow: which appear in the oil and gas industry. This type of flow contains large gas bubbles and slugs of liquid with dispersed gas bubbles. The importance of its study lies in the dangerous pressure variations that take place during its occurrence and that can jeopardise the structural integrity of pipelines.

- Free-surface flows: where a clear interface between the fluids appears and its behaviour is the main aspect to study.

- Particle-laden flows: transport of solid particles within a gaseous phase. Examples are pollutant dispersion analysis and aerosol deposition.

- Fluidised beds: in which a granular material is forced to acquire a dynamic fluid-like behaviour. This type of flow is used in fluidised bed reactors, fluidised bed combustion chambers, etc.

- Sedimentation: particles in suspension in a liquid phase that settle and remain against the walls of the containing vessel. Sedimentation mechanisms include gravity, centrifugal force, etc. Sedimentation in water treatment plants is a widespread example.

Two approaches exist to tackle multiphase modelling: the Euler-Euler and the Euler-Lagrange approach. In the Euler-Lagrange approach the Navier-Stokes equations are solved for the continuous phase whereas a number of particles of the dispersed phase are tracked, exchanging mass, momentum and energy with the continuous phase. This

approach is not appropriate in general for any application in which the volume fraction of the secondary phase cannot be omitted, i.e. such is the case of free-surface flows. On the other hand, in the Euler-Euler approach the concept of volume fraction of the different phases is introduced, which makes this approach suitable to track the interface between the fluids involved. The volume fraction constitutes a field of scalar values in space and time. The sum of the volume fraction of all the phases cannot be over one. Three different Euler-Euler models can be used in CFD [61]:

- The VOF model [62] solves a single set of momentum and mass conservation equations which is shared by the fluids. The interface is tracked using an additional transport equation for the volume fraction. This method is used when the tracking of the interface is interesting as it is the case in the present thesis.

- The mixture model also treats the phases as interpenetrating continua and prescribes relative velocities between the dispersed and the primary phase. This model is used for particle-laden and bubbly flows with low loading.

- The Eulerian model solves a set of momentum and mass conservation equations for each phase, coupling them with the interface exchange coefficients. The application range of this model is similar to that of the mixture model, including also fluidised beds and sedimentation.

The simulations performed in this thesis utilize the VOF method for the interface tracking of the free-surface flow within amine scrubbers.

2.2 CFD modelling of structured packing absorbers

Although the expansion of the calculation power of modern computers has been remarkable in the last decades, the three-scales strategy results from the incapability of current

computers to perform simulations of the whole absorption column focusing on every relevant detail of the flow. This strategy has already been applied in the literature [59, 60].

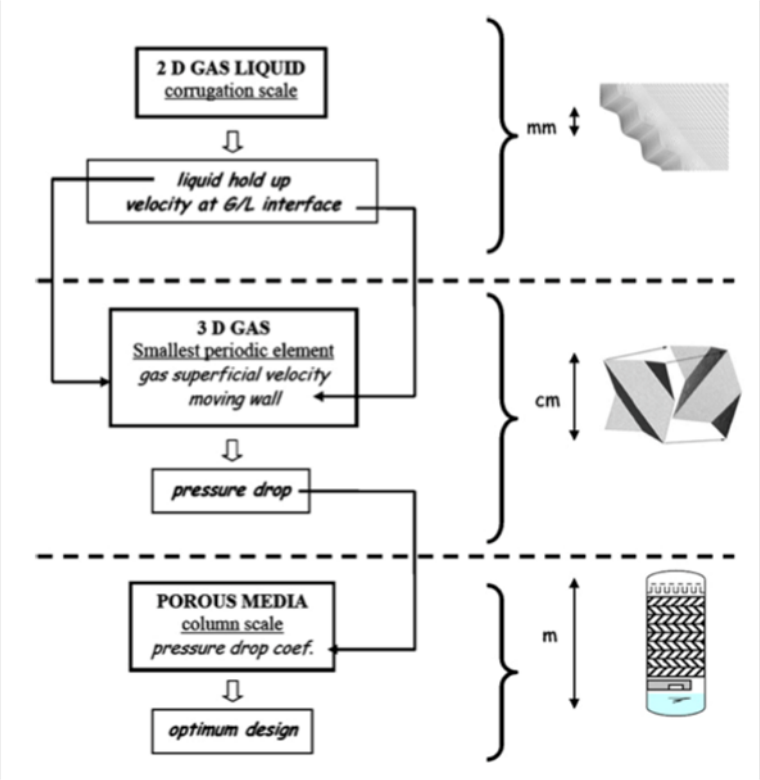

Figure 2.1: The three scales strategy for CFD modelling of structured packing materials [59].

The three scales are summarised in Figure 2.1 and are defined as follows:

- Small-scale, which consists in small 2D or 3D computational domains, often in the range of millimetres and up to about 10 centimetres. At this scale it is possible to implement an interface tracking method without an excessive computational cost due to the reduced size of the domain. Therefore, it is possible to describe the interaction between phases, solving aspects such as liquid spreading and maldistribution, liquid dragging phenomena or reactive mass transfer. Also the simplicity of the geometry allows the user to implement a structured mesh, which considerably reduces the required computational time.

- Meso-scale models consist of a limited set of representative elementary units (REUs), normally used to analyse dry pressure drop by means of single-phase simulations, i.e. including only the gas phase. A small set of REUs presents the same dry pressure drop per unit length as the entire column. This is used to assess the performance of the structured packing in this regard. After the dry pressure drop is obtained, the wet pressure drop can be calculated using correction factors that take into account the effect of the presence of the liquid phase.

- Large-scale models simulate the entire reactor assuming that the structured packing behaves as a porous medium with a high void fraction, i.e. with the porosity in the range of 0.95–0.98, in terms of liquid spreading. Large-scale simulations can also be used to study the influence of the different geometrical features such as liquid distributors, walls, etc. on the gas flow patterns.

Finally, process simulations constitute the highest modelling scale, although out of the purview of CFD methods. Process simulations are performed with specific software and focus on the interaction between the different pieces of equipment in a chemical process facility. The different devices are treated as a black box, where the output is calculated as a function of a series of input data [63–72]. Thus, in process simulations, there is no possibility of accessing any information about the characteristics of the internal flow, making CFD a necessity in order to gain further insight on the phenomena that take place inside the equipment.

A description of the CFD work done so far at the aforementioned different scales is included in the following sections.

2.2.1 Small-scale modelling

Small-scale modelling focuses mainly on tracking the interface between the fluids using small computational domains. By doing so, important flow features like liquid hold-up and the interaction between phases can be described with a high degree of detail, e.g. influence of geometric surface texture, diffusion of species into the liquid film, formation of droplets, waves and other liquid structures, etc [73–77]. The discussion of the literature at small-scale that follows focuses first on the hydrodynamics and continues with the reactive mass transfer.

The analysis of the hydrodynamics can be carried out with 2D or 3D simulations. 2D simulations offer the possibility of studying texture patterns on the solid surface and the development of the falling liquid film, i.e. velocity profiles and liquid film thickness can be assessed [78]. The liquid hold-up is hereafter calculated assuming that a perfectly developed liquid film covers the entire surface of the packing. The liquid hold-up is thus obtained multiplying the liquid film thickness from the simulations by the specific area of the packing. 3D simulations extend the capabilities of 2D, allowing to assess the formation of liquid irregularities (i.e. rivulets and droplets) that strongly influence the amount of interfacial area and the absorption rate. The formation of liquid irregularities within the liquid phase is known as liquid maldistribution and needs the tracking of the interface to be assessed.

An attempt to use small-scale VOF simulations to determine the liquid hold-up on structured packings was carried out by Raynal and Royon-Lebeaud [59]. The authors consider a 2D computational domain with both a smooth wall and a wavy corrugation pattern simulating the texture of the wall along which the falling liquid film is developed. The two surface texture patterns used by the authors can be observed in Figure 2.2. The fact that the liquid film thickness has the same order of magnitude as the amplitude of

the texture in the walls, i.e. approximately 0.3 mm, brings the hypothesis that the texture itself can heavily influence the development of the liquid film and the mass transfer [79].

Apart from the substantial increase in the computational resources that the VOF model requires, the fact that a sufficiently fine mesh has to be applied in those areas of the domain where important gradients are to be found, constitutes a justification of the three-scales strategy. As a matter of fact, such degree of detail provided by a very refined mesh at the vicinity of the wall could not be attained in meso- or large-scale domains.

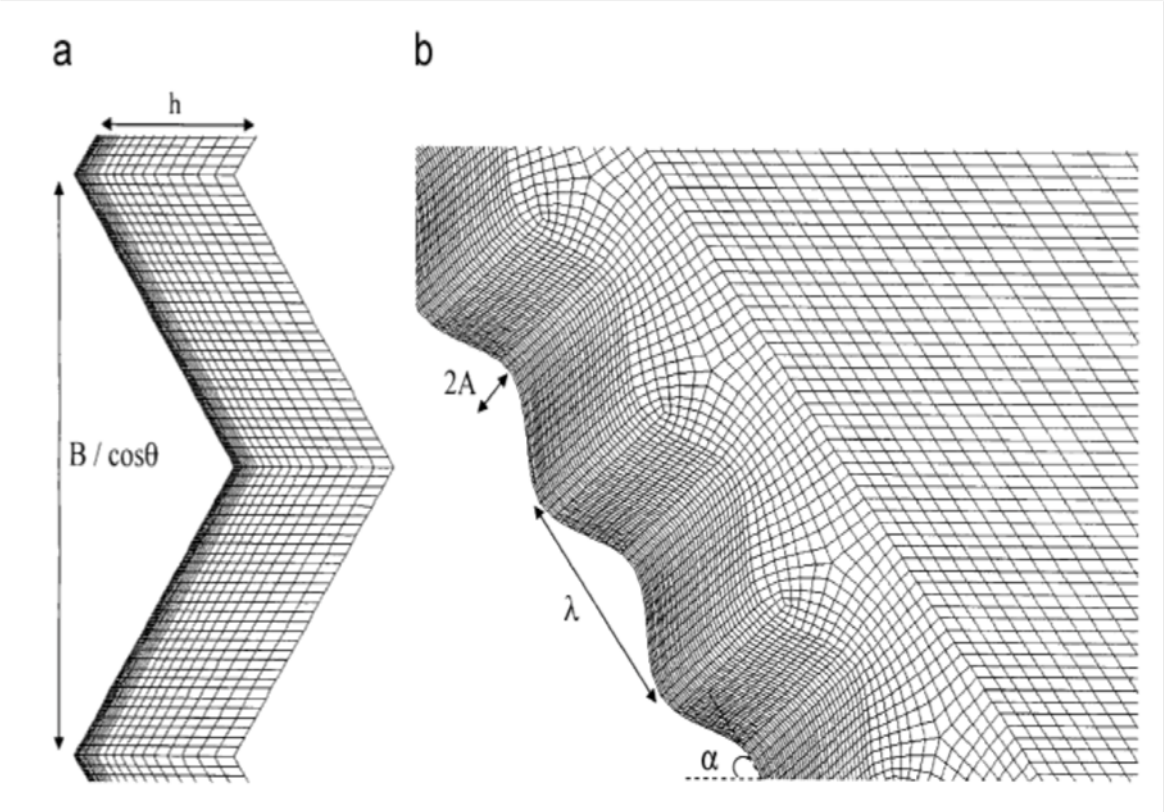

Figure 2.2: Surface textures tested in 2D small-scale simulations: a) flat pattern and b) wavy pattern [59].

The results obtained with the wall texture are in closer agreement with the experimental values than the results for the smooth wall, whilst some discrepancy is still found between both surface textures and the experiments. An analysis of the velocity field in-

side the liquid film is also carried out, coming to the conclusion that recirculation zones are generated at the valleys of the corrugation. This would explain, according to the authors, the higher liquid hold-up obtained in the simulations with rough walls compared to smooth walls, hence explaining the difference between them in terms of liquid hold-up. The appearance of those recirculation zones suggests the occurrence of two different components that added to one another result in the total liquid hold-up: the static and the dynamic liquid hold-up. Later, Zakeri et al [80] also suggested the appearance of the static and dynamic components. They defined the static liquid hold-up as the amount of liquid phase that cannot be renewed with the flow since it remains stuck at corners and dead spots.

The work from Raynal and Royon-Lebeaud [59] proves itself as a good tool to predict the liquid hold-up. However, the 2D approximation used presents a clear disadvantage since the geometry of the domain itself can vary depending on the cross-section considered on the packing. Secondly, 2D simulations use strict counter-current flow inside the domain whereas a complicated combination of co- and counter-current flow regimes actually takes place in a complex geometry such as a structured packing, with channels forming a particular angle with the vertical and between confronted channels belonging to different metallic sheets.

To avoid the drawbacks presented by 2D simulations, Zhang et al [81] studied the flow in an entire channel. Although this study represents a good approximation to reality, it does not take into account the entire geometry of a representative elementary unit (REU) yet. The study is a first approximation to the development of an interface tracking model at meso-scale, but still focuses on hydrodynamics, analysing liquid film thickness and pressure drop and not considering the actual repeating pattern in the packing.

Other work at small-scale includes 3D VOF simulations of the liquid film formation over an inclined metallic plate. For instance, Iso et al [82] reproduced the wetting regimes

achieved in the experiments as a function of the liquid load. They conclude that the amount of area of the plate covered by the liquid depends on the relationship between gravity and the surface tension, which is known as the Weber number. Large values of the Weber number result in a better liquid spreading whereas the interfacial area tends to the minimum energy state when surface tension prevails over gravity, giving way to the formation of round structures such as rivulets and droplets. Surface textures can help the fluid avoiding channelling phenomena, increasing the amount of area available to produce mass transfer. The authors, in this work, move from CFD analysis at small-scale to an experiment on a pilot-scale absorption column in order to check whether or not the assumption of including a particular texture on the surface of the packing could improve the CO_2 separation performance. The experiments confirmed the hypothesis of a better absorption rate for the textured pattern.

The maldistribution phenomenon due to the prevalence of distortive forces over cohesive forces is therefore one of the most important flow characteristics that can be observed at 3D small-scale CFD simulations and then extrapolated to full-scale. A significant amount of work has been found in the literature [83–87] dealing with the visualisation of the irregular distribution of liquid within the plate by measuring the liquid hold-up and the liquid spreading with gamma-ray, neutron radiography and X-ray tomography. The occurrence of this phenomenon was also tested by Olujić and Jansen [88] , who support the fact that surface tension is a key concept affecting proper liquid distribution over a packing material. The effect of surface tension is emphasised in their work, concluding that improving the wetting conditions enhances the mass transfer performance.

Small-scale numerical studies are mainly focused, as has been discussed, on the hydrodynamics and the tracking of the gas-liquid interface. However, small-scale presents itself as an adequate technique to implement reactive absorption and to test its effects inside the liquid film by contrast with the implementation of chemical reactions that has

been already observed at large-scale [89]. As is discussed in a later section, at large scale, it is possible to measure concentrations of a particular substance at the outlet and at different cross-sections of the reactor whereas an implementation of chemical reactions using the VOF method allows to reproduce the concentration profiles of a species along the thickness of the liquid film, giving a higher degree of detail. Three attempts have been made by Haroun et al [90, 91] and Haelssig et al [92] to describe the reactive mass transfer of a gas species into liquid films but both papers are limited to 2D computational domains, hence the impossibility of assessing the effect of liquid maldistribution. In their work, the authors present an analysis of the concentration profiles within the liquid film for a generic second order chemical reaction. The influence of the Hatta number and the contact time between the phases is observed in the different results obtained for the concentration profiles, distinguishing three regimes: one with an enhancement factor approximately equal to one, where the occurrence of the chemical reaction has no effect on the absorption rate; a second regime with a behaviour comparable to a first order reaction, hence the name pseudo-first order regime; and a third regime in which the enhancement factor is higher than one but does not vary with the Hatta number anymore.

2.2.2 Meso-scale modelling

The analysis of the dry pressure drop in the packing has been the target of meso-scale simulations as has been demonstrated that a reduced number of REUs presents the same pressure drop per unit length than the whole column [93–100]. The pressure drop along the absorber can be calculated with an expression analogous to the Darcy-Weisbach equation, i.e. pressure loss as a function of the kinetic energy of the gas and a proportionality constant called friction factor. The friction factor is a property of the particular geometry considered.

Larachi et al [94] presented the different types or REUs that can be observed in Figure 2.3. The most used REU is the one shown in Figure 2.3a, which corresponds to the bulk of the packing, being the others a representation of the geometries found near the column walls, below the liquid distributor at the top part of the column, etc.

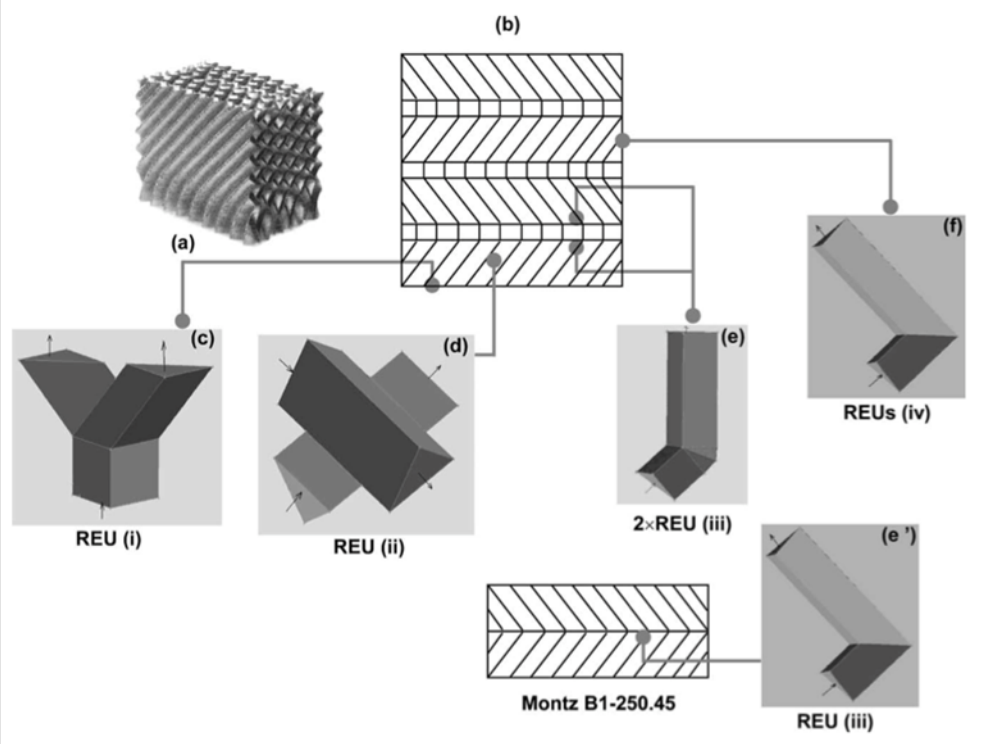

Figure 2.3: Different REUs used for meso-scale CFD analysis: a) Image of the MontzPak B1-250.45 packing, b) packing schematic to show the situation of the different REUs, c) entrance region, d) criss-crossing junction, e) and e') interlayer transition f) channel-wall transition [94].

Most of the work regarding pressure drop along the absorber has been experimental, resulting in empirical correlations only applicable to a limited range of conditions. The work reported in the literature is extensive in this regard [101–103]. Dry pressure drop inside the packing can be obtained as the sum of two components: the drag component and the friction component. The drag component is due to changes in the direction of the flow near the column walls and in the transition area between two packing layers,

which are rotated 90° with respect to each other. The friction component encompasses the interaction between the different gas flows inside the triangular channels that form the metallic sheets and the pressure loss caused by the friction with the packing walls. It is believed that, in the case of packings with a specific area above 250 m^2/m^3, the frictional force is the predominant component. Said et al [93] studied the pressure drop due to the friction term in a reduced number of REUs. The main contribution of their work was to establish a correlation for the pressure drop as a function of the dimensions of the packing itself. The influence of several turbulence models was also assessed. Recently, Boccardo et al [104] presented a new methodology that can be applied either for random packings or catalytic beds, which the authors claim to be time and computationally more effective. The geometry is reproduced with the open source computer graphics code Blender^{TM}. This code allows the user to reproduce more complex geometries than using other techniques such as microcomputer tomography or Scanning Electron Microscope (SEM). The methodology is applied to the prediction of the void fraction inside the bed and the dry pressure drop.

As a conclusion, meso-scale CFD work has focused on single-phase simulations to reproduce the dry pressure performance of the packing. Figure 2.4 presents a typical dry pressure vs. F-factor characteristic for a structured packing section. As is described in the mathematical description, the dry pressure drop follows a law analogous to the Darcy-Weisbach equation. The pressure drop is thus proportional to the kinetic energy of the gas, i.e. the kinetic energy depends on the velocity squared. This fact justifies the non-linear behaviour shown in Figure 2.4.

Empirical correlations and theoretical studies have been necessary *a posteriori* to get information about the pressure drop that appears in the column under the presence of the liquid phase, i.e. wet pressure conditions. Wet pressure drop is always higher than dry pressure drop due to the presence of the liquid. The formation of the liquid film over the

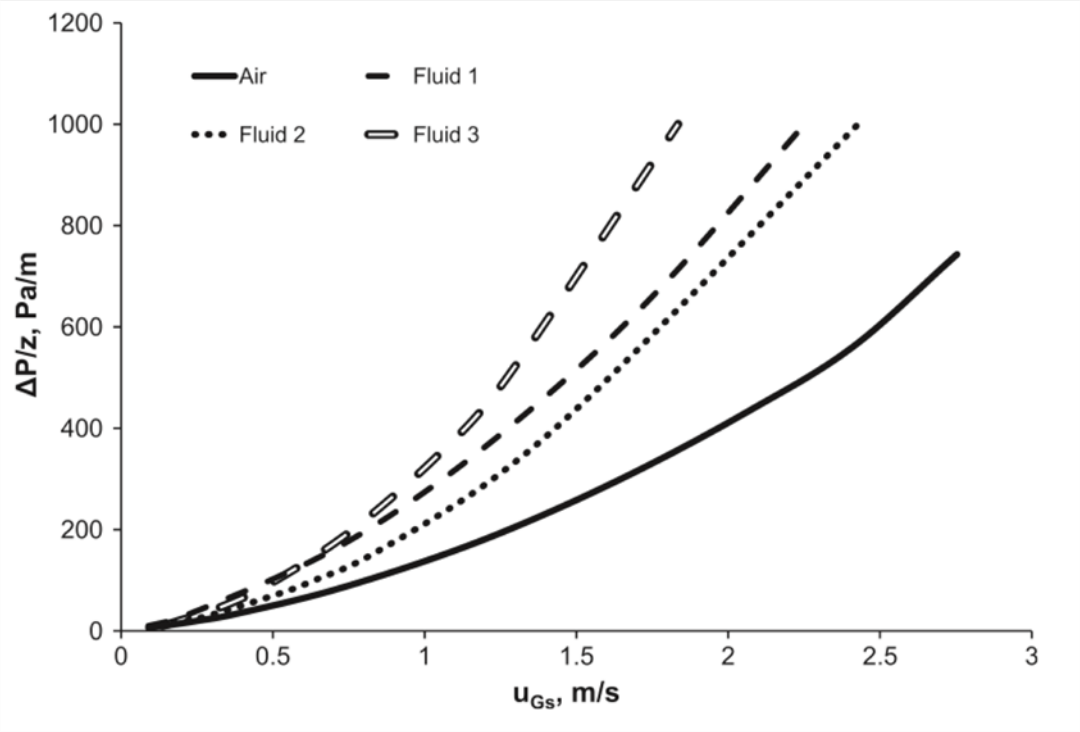

Figure 2.4: Example of dry pressure drop per unit length of column $\Delta P/z$ vs. gas superficial velocity $u_{G,s}$ in a structured packing column [93].

packing narrows the channels through which the gas flows inside the column, accelerating it and resulting in a lower void fraction and an increased gas velocity. The procedure to obtain the wet pressure drop from single-phase simulations reads as follows:

1. The curve of the dry pressure drop as a function of the F-factor is obtained. The F-factor is the result of multiplying the squared root of the density by the velocity of the gas.

2. The velocity of the gas is corrected by a factor that considers the presence of the liquid. To be more specific, what this factor takes into account is the correction of the void fraction due to the presence of the liquid. As a matter of fact, the void fraction of the packing modified by the liquid hold-up appears in the correction term. The liquid hold-up is the volume of liquid phase per unit volume of the

structured packing.

3. After the velocity has been corrected, the same dry pressure graph can be used to obtain the wet pressure drop by introducing the value of the corrected velocity.

The main source of error in the described procedure is the calculation of the liquid hold-up. Normally, the liquid hold-up is obtained upon the assumption of a perfectly formed liquid film over the packing, i.e. as the product of the liquid film thickness times the specific area of the packing [105]. This assumption has been proven not to be accurate enough as it will be analysed in Chapter 7. A new two-phase CFD model with interface tracking, able to reproduce the magnitude of the liquid hold-up correctly, could save this step and be used to predict the wet pressure drop.

Moreover, such a model could also be used to predict the loading conditions. The loading conditions are the threshold beyond which the drag caused by the gas phase can affect the behaviour of the liquid phase. Figure 2.5 represents a generic liquid hold-up vs. gas phase velocity graph for a structured packing column. Before the loading conditions are reached, the velocity of the gas does not affect the liquid hold-up, which is only a function of the liquid load. Beyond the loading conditions, the increase on the shear stress at the interface results in the liquid being hold inside the column, increasing the liquid hold-up and the pressure drop according to an exponential law. In the graph, this is represented with the range of values marked as loading region. The increase in the liquid hold-up is exponential under those conditions. Finally, the drag caused by the gas phase can totally impede the flow of the liquid, in what is called flooding conditions. In the graph, this is represented by the horizontal line marked as $h_{l,FL}$.

As a conclusion, with the aforementioned scenario, the gap in the research at meso-scale is still to implement an interface tracking method able to reproduce the interfacial area (i.e. contact area between both phases, in which the mass transfer process actually

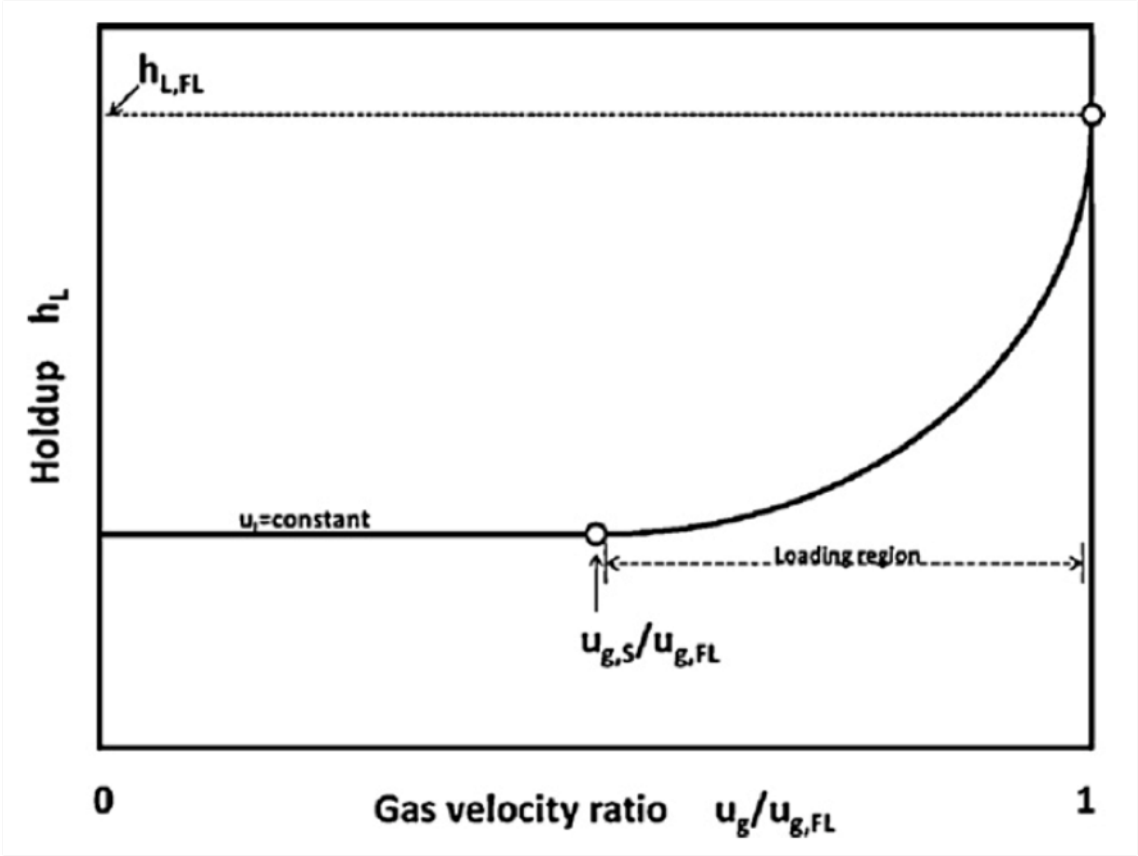

Figure 2.5: Liquid hold-up h_L vs. adimensional superficial gas velocity $u_g/u_{g,FL}$. The superficial gas velocity u_g is adimensionalised using the value that causes flooding $u_{g,FL}$ [80].

takes place), the liquid hold-up and the wet pressure drop. Such a modelling tool could be applied to the optimisation of the existing packings and the research for new and improved geometries. This gap in the research is intended to be investigated in Chapter 7, where a meso-scale model with interface tracking is presented, allowing the user to visualise liquid maldistribution over the packing and to calculate both the liquid hold-up and the interfacial area per unit volume of packing.

2.2.3 Large-scale modelling

As previously explained, liquid maldistribution constitutes one of the most important characteristics to be studied regarding the performance of structured packing absorbers since it directly affects pressure drop, which is one of the highest energy penalties in post-combustion CCS facilities. The study of this characteristic has been mostly reserved to small-scale simulations due to the fact that an interface tracking method can only be implemented at this scale with a reasonable computational cost. In this work, the study is extended to meso-scale, allowing the possibility of visualising the effect of gravity and surface tension on the formation of liquid films in actual commercial geometries.

Liquid maldistribution can also be assessed with CFD simulations at large-scale. In this direction, Fourati et al [106] expanded their study with gamma-ray tomography taking a correlation used by Lappalainen et al [107–109] to predict the variation of the liquid hold-up as a function of the viscosity. The authors implemented it in a Eulerian two-fluid CFD model. Figure 2.6 shows the results obtained in the experimental work from the authors [83]. Each horizontal series of images represents the liquid dispersion found in cross sections of the packing at different heights. All the images in the figure are taken for the same value of the liquid load and each horizontal series of images represents a different value of the F-factor. The images on the left-hand side correspond to the top section of the column whereas the images on the right-hand side correspond to those at the bottom. It can be seen how the liquid is better distributed as it approaches the lowest part of the column. In addition, it is also possible to see the heterogeneous distribution, which gives an idea of the liquid maldistribution at the whole column scale.

As a conclusion, the agreement of their simulations with the experimental work is generally good but there is still some difference between them. In their discussion the authors state that the distribution of the liquid within the packing is caused by two mechanisms:

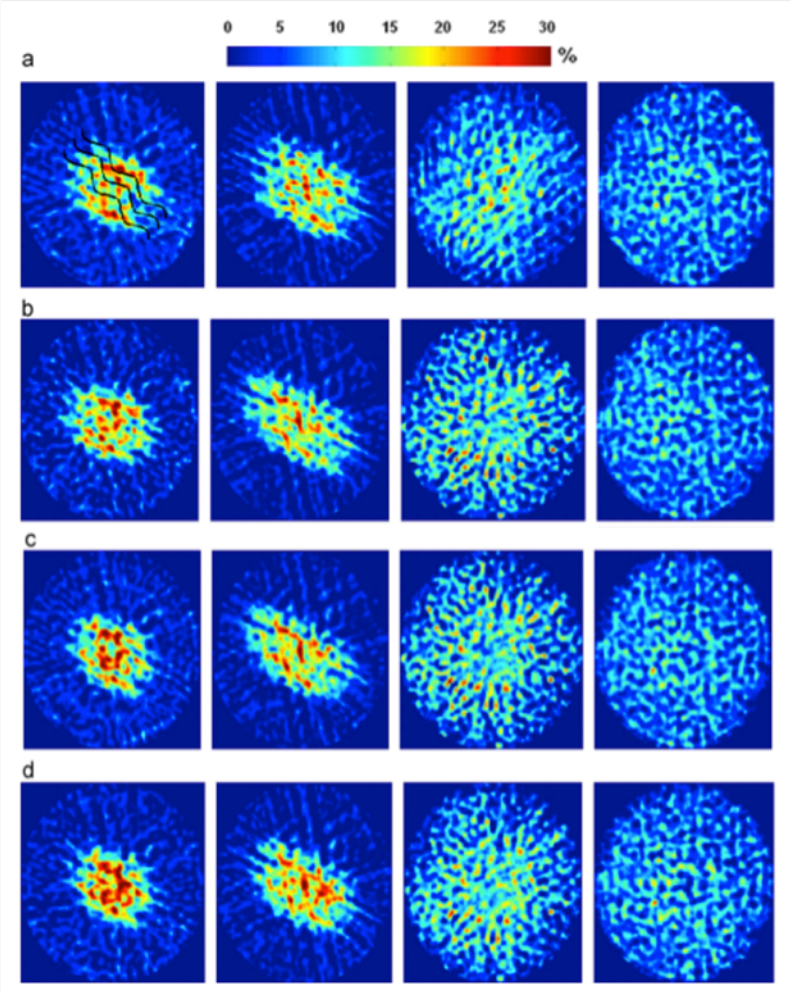

Figure 2.6: Visualisation of liquid maldistribution obtained with gamma-ray tomography [83].

- Advection: in the model the value of the velocity used is volume-averaged and this does not represent the reality with a good degree of accuracy, causing the difference between the CFD model and the experiments.

- Capillarity: which cannot be properly represented in a porous medium. The influence of capillarity in the liquid dispersion is also acknowledged by Soulaine et al [110], who also developed a 3D porous medium model to study the dispersion of liquid over the structured packing. Capillarity effects are more pronounced in the

area surrounding the contact points between the metallic sheets. This was proved by Alekseenko et al [111], who used optic fibre sensors to measure the liquid film thickness inside the packing and discovered the formation of menisci near the contact points, which are the origin of the redistribution of liquid over the channels. This effect at the contact points cannot be represented in a porous medium simulation hence loosing the representation of this effect. The capillarity analysis also reinforces the need of including not only one metallic sheet but more than one in the computational domain at meso-scale to reproduce the effect of the contact points between sheets in the numerical studies.

The research reported at large-scale shows the importance of the liquid maldistribution phenomenon and suggests the need to develop models at lower scales in order to study it.

2.2.4 Interconnection between scales

The different scales are not exclusive. The last published studies have been devoted to connecting them, hence expanding their capabilities [112–114]. In this direction Pham et al [115] and Asendrych et al [116] developed a large-scale model to analyse porous resistance and liquid dispersion including reactive mass transfer inside the liquid phase. The authors also include an estimation of the wet pressure drop per unit length in the absorber as a function of the F-factor. Liquid hold-up vs. liquid load along the porous medium is also represented and compared against experimental data with a high degree of accuracy. Regarding reactive mass transfer, the model is able to reproduce the concentration of CO_2 in the gas phase along the reactor and the concentration at the outlet with a high degree of certainty. Their work constitutes, in this way, a valuable approximation to an integral model of the gas-liquid flow inside the absorber, integrating features that were initially reserved to lower scales in the literature. Therefore, the capabilities

of large-scale modelling are expanded in this paper but it can still be noticed that some details like the concentration profiles within the liquid film or the distribution of the liquid over the metallic walls of the packing cannot be reached with this approach mainly due to the fact that the geometry of the packing material is approximated to a porous medium and does not include the actual geometry. Small-scale simulations are, consequently, still necessary to assess aspects such as liquid film development and its interaction with the surrounding gas phase.

Another example of interconnection between scales has been presented by Haroun et al [117], who managed to track the interface between fluids using the VOF method on a metallic sheet of MontzPak B1-250. The authors reproduce experimental results concerning the gas-liquid interface tracking, interfacial area and film thickness in a limited set of REUs of the commercial packing. This constitutes a substantial improvement with respect to previous studies at meso-scale, which focused only in dry pressure calculations. Finally, the authors use their model to analyse the influence of contact angles on the interfacial area. The contact angles are used to mimic the effect of surface roughness and textures on the packing wall. However, in this study, the liquid film falls along only one sheet of the structured packing whereas in a real case, the metallic sheets are confronted, with their channels forming a 90° angle between them. This results in the appearance of contacting points between the metallic sheets that strongly influence the development of the liquid flow inside the structured packing. Despite this, the model reproduces the variation of interfacial area with the liquid load, which is validated against experimental results presented by Tsai et al [118].

Process simulations can also be linked to CFD in order to get a comprehensive description of CCS facilities. The work of Brinkmann et al [119], Fei et al [120], and Edge et al [121] deal with this co-simulation approach.

2.3 Reactive mass transfer into a falling liquid film

This section is dedicated to the review of the different aspects relevant for the development of the present CFD model. This section will be divided in two subsections: one regarding the absorption mass transfer and another one reserved to the reaction kinetics:

- Absorption mass transfer: first of all the different theories for interfacial mass transfer are discussed and the choice is justified by its suitability to be easily coded on a UDF.

- Reaction kinetics: there is some controversy among the scientific community about the correct description of the kinetics of the CO_2-MEA chemical system. Between the two more widespread mechanisms, the choice is done so that the minimum number of species is implemented in the model, hence reducing the computational load.

The review of these aspects is also based on how to implement them on the UDF.

2.3.1 Mass transfer

Different approaches have been reported in the literature for the description of the interfacial mass transfer that takes place during the absorption process. All of them assume unidirectional diffusion. The most utilised option in CFD modelling studies has been the penetration theory due to its suitability to describe transient systems:

- The two-film model [122]

  This model is based on the assumption that a stagnant film with a finite thickness exists at both sides of the interface, for the liquid and the gas, respectively.

Mass transport takes place under steady state conditions within this film via diffusion mechanisms whereas convection is considered to be negligible. Outside the film complete mixing of the species occurs, eliminating any concentration gradient within.

- The penetration theory [123]

  This theory assumes that the diffusion of the gas into the film is an unsteady process by virtue of the random motion of the solute molecules. This theory seems suitable to be adapted to the present simulations due to the fact that the mass transfer is described as a transient process.

- The surface renewal model [124]

  This model was presented as an extension for Higbie's penetration theory and the main difference lies in the fact that the contact time is not the same at every moment but it follows a particular distribution function. Perlmutter [125] reviewed this theory taking into account eddy residence time distributions and other aspects such as transient interfaces, changes in the value of the diffusivity near the interface, dead zones in which local laminar flows are developed and multiple capacitance effects.

Higbie's penetration theory remains the most accepted theory among CFD models for mass transfer processes and will also be used to carry out the present work.

Although some authors state that the change in the solubility with the concentration of MEA in the aqueous solution can be neglected [126], some models have been reported in the literature to calculate it accurately. The solubility of any gas into a liquid is calculated using Henry's law, which states that the maximum concentration of the gas species within the liquid phase when the VLE conditions are reached is proportional to the partial pressure of the gas species in the bulk of the gas phase. The proportionality constant is

called Henry's law constant and its calculation for carbon dioxide into aqueous mixtures of alkanolamines has been widely investigated in the literature [127–136], in most of the cases using the N_2O analogy. This analogy is based on the fact that, since carbon dioxide reacts with the liquid solution, its solubility cannot be directly measured without the inherent error posed by the mass transfer enhancement that the chemical reaction causes. Hence, the solubility of a similar inert molecule needs to be calculated and the results need to be extrapolated to the original molecule of interest. Some authors are critical with this strategy, though. Monteiro and Svendsen [137] state that *"there is no sound evidence in literature that the ratios of the solubility of N_2O to that of CO_2 in water can be used for correlating the solubilities of the two gases in systems of industrial interest for post-combustion carbon capture"* and that the ratio may be restricted to aqueous solutions much more diluted than the ones used at industrial scale, i.e. the reference case and the most widely studied is 5 M MEA solution (30% wt.). However, the N_2O analogy is still extensively used by authors to investigate solubility.

Penttilä et al [138] present in their work an exhaustive correlation that encompasses both binary and tertiary amine solutions of particular interest for CCS applications. Measurements of the solubility of carbon dioxide in amine solutions have been focused on limited values of temperature and amine concentration in the literature. The authors extended the temperature range to up to 393 K, at which the regeneration of the amine occurs in the stripper. Such an extension of the temperature range was needed in order to encompass all the temperatures encountered in a post-combustion CCS facility and not only in the absorber. The MEA concentrations go up to 45% wt., which also covers the operating range of concentrations. The correlation presented by Penttilä et al [138] is used in the present work to calculate the solubility of carbon dioxide in aqueous amine solutions whereas the Wilke-Chang equation is used to obtain the values of the diffusivity.

2.3.2 Reaction kinetics

The concept of reactive absorption was developed early in the XX^{th} century (c. 1930) to remove acidic gases from waste gas effluents using amines, hence it is a mature technology that can, furthermore, be retrofitted to existing power plants at a small extra cost [50]. The advantage presented by reactive absorption lies in the fact that the existence of the chemical reaction enhances the absorption process, making it suitable to treat gas streams with a low concentration of CO_2 such as those that result from the combustion of fossil fuels. Although screening of new substances to improve the reactive absorption of CO_2 is an open field and new solvents are continuously being investigated [139–143], aqueous solutions of alkanolamines are considered as an especially attractive option [144–146]. Monoethanolamine (MEA) is widely used as the reference to compare new mixtures and solvents [6].

The CO_2-MEA chemical system consists of a sequence of finite rate and instantaneous reactions in which the combination of MEA with carbon dioxide to form a carbamate is considered as the controlling step of the system. This carbamate holds the carbon within the liquid solution, which is regenerated in the stripper to retrieve the pure CO_2. Although a detailed knowledge of the reaction mechanism is needed in order to allow designing more efficient absorbers, there is still some controversy about the exact steps that take place during the formation of the carbamate. This affects the CFD modelling due to the fact that the computational time is altered by the number of species being involved. Therefore, from the CFD modelling point of view it is more interesting to condensate the chemistry of the system in the lowest possible number of reactions. Currently, two different reaction mechanisms are being considered in the literature:

- The zwitterion mechanism was first introduced by Caplow [147] and reviewed later by Danckwerts [124]. This mechanism is based on the existence of an intermediate

step in which a dipolar molecule called zwitterion is formed. Subsequently, the zwitterion is deprotonated by a base, which can be either water, or the hydroxyl ion or the amine itself. The following reactions describe the formation, i.e. equation (2.1), and the deprotonation of the zwitterion to give the carbamate, i.e. equation (2.2). Both reactions can be expressed as

$$CO_2 + RNH_2 \longleftrightarrow RNH_2{}^+COO^-, \tag{2.1}$$

and

$$RNH_2{}^+COO^- + B \longleftrightarrow RNHCOO^- + BH^+. \tag{2.2}$$

- The termolecular single-step mechanism skips the intermediate step by which the formation of the zwitterion takes place [148]. Therefore, the chemical reaction can be written as

$$CO_2 + H_2O^+ RNH_2 \longleftrightarrow RNHCOO^- + H_3O^+. \tag{2.3}$$

The zwitterion mechanism has been widely accepted [149–151] since it was first put forward in 1968. Xie et al [152] indicated that none of the experiments carried out up to that date had detected the presence of such molecule. However, they concluded that their results are in accordance to the presence of a two-step reaction to form the carbamate, with the middle step being the formation of a zwitterion, giving experimental evidence of its existence. Han et al [151] also back the hypothesis of the existence of the zwitterion. Veersteg et al [153] support the hypothesis of the formation of the zwitterion, in which the first step of the reaction, i.e. equation (2.1), would be the limiting step of the system.

Conversely, the direct mechanism has been supported by experimental evidence given by da Silva and Svendsen [154] and Aboudheir et al [155] whose experimental data do not reveal the existence of any zwitterion whatsoever.

Some controversy is also found regarding the order of the reaction. In the work of da Silva and Svendsen [154] suggested third order kinetics whereas Xie et al [152] establish that a first order mechanism is the most accepted among the scientific community. Versteg et al [153] defends the second order approximation. Therefore, it seems that the only consensus is that the reaction leads to the final formation of a carbamate.

In this work, the direct single-step approximation is used since the objective is to study the overall rate of absorption of CO_2 rather than the intermediate steps of the chemical system. The chemical reaction as it appears in the work published by Kale et al [156] is used in the present simulations. According to the authors, the chemical system consists of two finite rate reactions and five instantaneous reactions. Only finite rate reactions can be modelled with UDF source terms whereas the concentrations of the species involved at equilibrium should be previously introduced at the liquid inlet boundary conditions to take into account the instantaneous reactions. The two finite-rate reactions considered by these authors as

$$CO_2 + OH^- \longleftrightarrow HCO_3{}^-, \tag{2.4}$$

and

$$CO_2 + MEA + H_2O \longleftrightarrow MEACOO^- + H_3O^+. \tag{2.5}$$

In the reaction (2.4), a carbon dioxide molecule reacts with a hydroxide ion to form a bicarbonate ion. Reaction (2.5) is the carbamate formation, in which carbon dioxide reacts with the monoethanolamine to form the carbamate after its deprotonation. The proton from the zwitterion is attached to a water molecule forming a hydronium ion.

The carbamate formation reaction is the controlling step due to its fast kinetics com-

pared to the bicarbonate formation. The system can be described as following second order kinetics [157]. Therefore, the carbamate formation reaction is implemented in the source terms of the present simulations.

As was mentioned before, the existence of the chemical reaction results in an enhanced overall mass transfer rate from the gas to the liquid phase. The consumption of the solute helps keeping a high value of the concentration gradient of that particular species between the bulk of the liquid and the saturation value. This greater difference in the concentration gradient results in an increased mass transfer rate. Plus, the mass transfer rate increases with the velocity of the reaction. The enhancement factor measures the difference in the absorption rate with and without chemical reaction [158–160]. The enhancement factor can also be expressed as a function of the Hatta number, which quantifies the relationship between the reaction rate and the mass transfer coefficient. Figure 2.7 shows the relationship between the enhancement factor and the Hatta number.

Three different regimes can be distinguished in the graph depending on the value of the Hatta number, which also affects the necessity for a finer computational mesh within the liquid film in order to capture the concentration gradients [161]:

- The reaction is slow when the Hatta number presents values lower than one. In this case there is enough time for the solute to be diffused into the liquid film once it has been absorbed. Under this assumption, the chemical reaction takes place within the entire liquid film thickness. The concentration gradient between the bulk liquid phase and the saturation conditions, i.e. at the interface, is kept to a minimum and no improvement in the absorption rate appears, which translates in enhancement factors close or slightly bigger than one.

- An intermediately fast reaction occurs when the Hatta number presents higher values. In this case, the reaction is fast enough to provide an enhancement in the

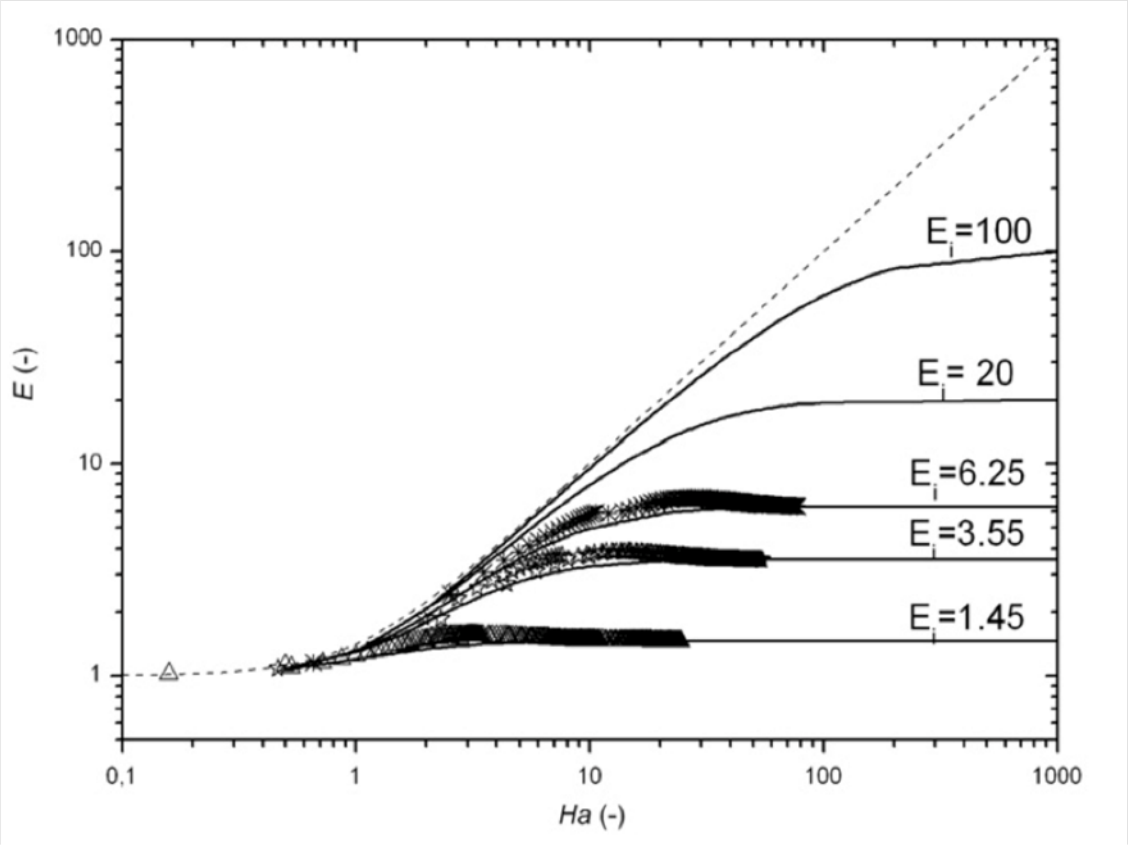

Figure 2.7: Enhancement factor E vs. Hatta number Ha for a generic second order chemical reaction. The parameter E_i denotes the enhancement factor for an instantaneous reaction [91].

absorption rate. The system follows the pseudo-first order reaction regime in which the value of the enhancement factor can be approximated to the Hatta number. The range of values of the Hatta number for this stage goes from 1 to a value that depends on the theoretical enhancement factor for an instantaneous irreversible reaction, i.e. E_i in Figure 2.7. In the CO_2-MEA system, the latter is a function of the difference in concentration between the monoethanolamine and the carbon dioxide.

- A very fast or instantaneous reaction takes place if the Hatta number keeps augmenting. Under these conditions the chemical reaction is so fast that there is no time for the solute to be diffused into the bulk of the liquid as it is consumed as

soon as it penetrates into the liquid. Therefore, the reaction takes place only at the gas-liquid interface. If the concentration of the amine is very high, i.e. as is the case in industrial applications such as CCS, compared to the value of the solubility of the solute in the aqueous solution, the reaction also presents a pseudo-first order behaviour, hence fast pseudo-first order [162]. If that is not the case then the enhancement factor is not a function of the Hatta number anymore but presents a constant value due to the depletion of the alkanolamine.

The CO_2-MEA chemical system represented in the present thesis follows the behaviour explained in the third bullet point, i.e. fast pseudo-first order. The fact that the chemical reaction takes place only at the vicinity of the interface will be used to check the coherence of the model.

Chapter 3

Mathematical Theory

The mathematical theory that describes the modelling of the multiphase flow inside structured packing columns is presented in this chapter. The discussion begins with a short note about CFD and follows with the derivation of the mass and momentum conservation equations that govern the present model. This work presents the novelty of combining both a momentum source term describing surface tension and a mass source term describing reactive mass absorption. The conservation equations are combined into a single equation that governs the multiphase flow with reactive absorption, highlighting the influence of the mass source term on the momentum conservation equation. Further down, the chapter deals with the theoretical development of the mass source terms, the description of the reaction kinetics, the solubility, and the diffusivity of the CO_2-MEA chemical system. Finally, the chapter closes with the equations that describe the pressure drop inside the absorber.

3.1 Computational Fluid Dynamics

CFD is the use of applied mathematics and computer codes to obtain the velocity and pressure fields that describe any flow. Additional software, i.e. a post-processor, is used afterwards to visualise the characteristics of the flow obtained with the solver. CFD applies computing algorithms to solve the Navier-Stokes equations numerically. An alternative CFD technique that is gaining popularity nowadays is the Lattice-Boltzmann method (LBM). LBM solves the discretised form of the Boltzmann equation instead of the Navier-Stokes equations. Despite the increasing popularity of the LBM method, it presents some limitations when applied to some particular types of flow such as those with high Mach numbers and multiphase problems [163]. With this scenario, LBM is discarded for the application in the present thesis due to its limitations to treat multiphase flows. Instead, the simulations discussed in this work are performed using the commercial software ANSYS® Fluent v14.0, which solves the Navier-Stokes equations. Three different techniques exist for the discretisation of the conservation equations for mass and momentum: the finite difference method (FDM), the finite volume method (FVM) and the finite element method (FEM). The most widely used method to solve fluid dynamics problems is the FVM technique. The FVM method is thus used in the present thesis.

Multiphase flows are at the forefront of the CFD research nowadays. Most of the research is focused on the development of accurate techniques to track the interface between fluids in an accurate manner. With the introduction of supercomputers in the 1960s and their ulterior development, it has been possible to solve more complicated problems. This work is intended to be one more step in the exploration of the capabilities of applying CFD and interface tracking techniques to free-surface flows with chemical absorption. The present model uses the VOF method as the interface tracking technique to solving the multiphase flow inside a post-combustion CCS absorber. In this method a single set

of mass and momentum equations is discretised according to the aforementioned FVM method and subsequently solved simultaneously for all the fluids involved. Accordingly, all the fluids share the velocity and the pressure fields obtained.

In order to accomplish the interface tracking, the VOF method introduces an additional variable called volume fraction α, which is a scalar function that denotes the membership of a particular computational cell to a certain subset, i.e. each subset constitutes each of the phases involved, within the numerical domain. The position of the interface can thus be tracked by solving an additional transport equation for the volume fraction of the i^{th} phase which can be written as

$$\frac{\partial \alpha_i}{\partial t} + \vec{v} \cdot \nabla \alpha_i = 0, \tag{3.1}$$

where α_i is the volume fraction of the i^{th} phase, and $\vec{v}$ is the velocity vector. The primary phase needs to be defined in the set-up of the simulation. The continuity equation is solved for the rest of the phases present in the case. The volume fraction of the primary phase is thus computed by difference, taking into account that the sum of the volume fraction of the N phases in each particular computational cell has to be equal to one as

$$\sum_{i}^{N} \alpha_i = 1. \tag{3.2}$$

Two phases are defined in the present simulations: the liquid phase, i.e. an aqueous MEA solution, and a gas phase containing CO_2. The gas phase is set as the primary phase. Once the volume fraction field is obtained, a value of zero means that the cell belongs to the gas phase whereas a value of one means that the cell is occupied by the liquid phase. Subsequently, cells whose volume fraction lies between 0 and 1 correspond to the interface. Although widely used in the literature, this treatment, in which the interface is formed by a finite number of cells, constitutes a source of error. The reason is that the

interface is a progressive zone where the volume fraction adopts a continuum of values and not a discontinuity as it happens in reality. Mesh refining methods such as the one introduced by Cooke et al [164] are needed in the vicinity of the interface in order to approximate the solution as much as possible to the actual discontinuous behaviour found in nature.

Once the volume fraction is computed in each cell, its value is used to determine the averaged values of the material properties. Therefore, the density ρ and the dynamic viscosity μ are computed as

$$\rho = \rho_l \alpha_l + \rho_g \alpha_g, \tag{3.3}$$

and

$$\mu = \mu_l \alpha_l + \mu_g \alpha_g. \tag{3.4}$$

After the obtention of the volume fraction field, the next step is the reconstruction of the interface, which is accomplished in this model using the Geometric-Reconstruction method [165–167].

3.2 Mass and momentum conservation equations

The mass and momentum equations that govern the model are derived in this section. The present model presents the novelty of combining both a momentum and a mass source term in the same set of conservation equations. This, combined with the use of the VOF method, results in the acceleration of the differential volume being a function of the mass source term. A comprehensive derivation of the conservation equations is shown in this section to highlight this feature.

3.2.1 Mass conservation equation

The mass conservation equation is derived considering the mass balance in a differential volume dV defined by a particular value of the density $\rho = f\left(\vec{r},t\right)$ and the velocity vector $\vec{v}$ at the centre of the volume (Figure 3.1) according to

$$\vec{v} = u\vec{i} + v\vec{j} + w\vec{k}. \tag{3.5}$$

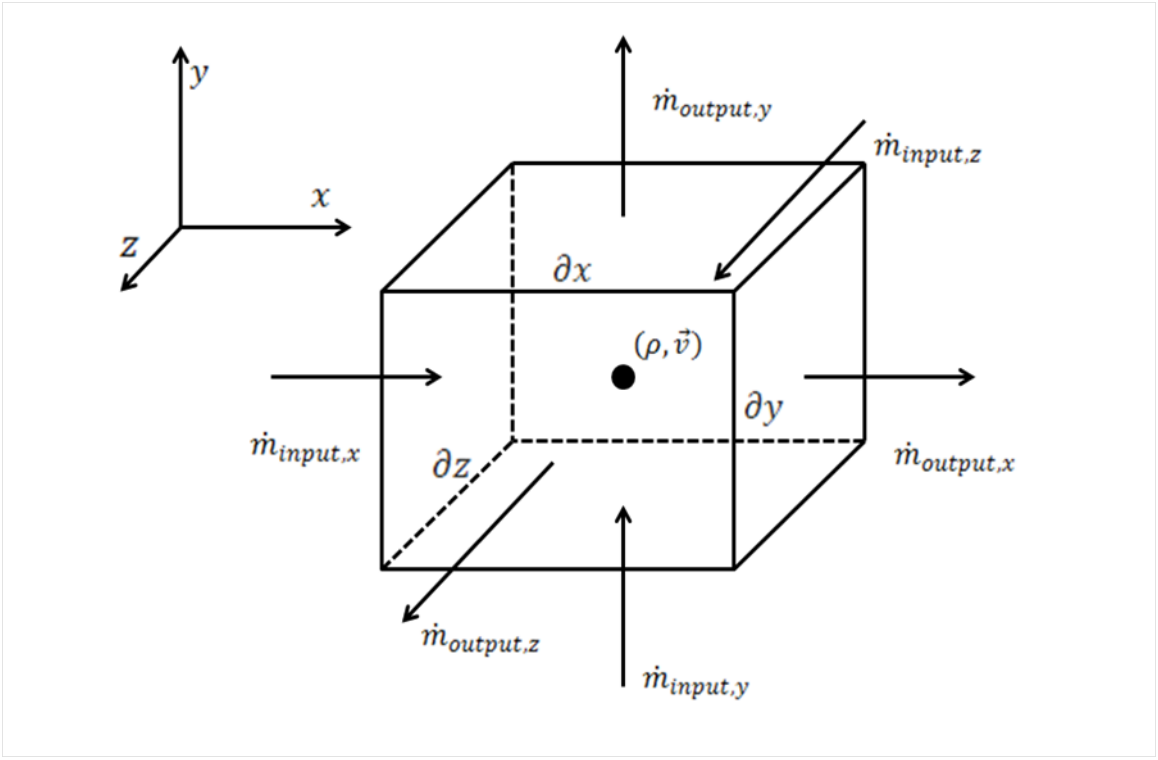

Figure 3.1: Mass flux through a differential volume dV.

In the x-axis the mass flow rate $\dot{m}$ leaving the differential volume is obtained as the mass flux at the cube face times the area of the face. The mass flow rate at the face is calculated from the value at the centre of the differential volume using the Taylor expansion series as

$$\dot{m}_{output,x} = \left[(\rho u) + \frac{\partial(\rho u)}{\partial x}\frac{\partial x}{2}\right]\partial y \partial z. \tag{3.6}$$

In a similar way the mass flow rate entering the differential volume is described as

$$\dot{m}_{input,x} = \left[(\rho u) - \frac{\partial(\rho u)}{\partial x}\frac{\partial x}{2}\right]\partial y \partial z. \tag{3.7}$$

Analogously, for the y-axis the expressions are

$$\dot{m}_{output,y} = \left[(\rho v) + \frac{\partial(\rho v)}{\partial y}\frac{\partial y}{2}\right]\partial x \partial z, \tag{3.8}$$

and

$$\dot{m}_{input,y} = \left[(\rho v) - \frac{\partial(\rho v)}{\partial y}\frac{\partial y}{2}\right]\partial x \partial z. \tag{3.9}$$

For the z-axis, the mass output and input read, respectively,

$$\dot{m}_{output,z} = \left[(\rho w) + \frac{\partial(\rho w)}{\partial z}\frac{\partial z}{2}\right]\partial x \partial y, \tag{3.10}$$

and

$$\dot{m}_{input,z} = \left[(\rho w) - \frac{\partial(\rho w)}{\partial z}\frac{\partial z}{2}\right]\partial x \partial y. \tag{3.11}$$

Finally, the complete mass balance in the differential volume states that the accumulation of mass equals the difference between mass input and output plus the contribution from any mass source S_{mass} as

$$\frac{\partial \rho}{\partial t} = \dot{m}_{input} - \dot{m}_{output} + S_{mass}. \tag{3.12}$$

Inserting equations (3.6) through (3.11) into (3.12) and rearranging we obtain

$$\frac{\partial \rho}{\partial t} + \left[\frac{\partial (\rho u)}{\partial x} + \frac{\partial (\rho v)}{\partial y} + \frac{\partial (\rho w)}{\partial z} \right] = S_{mass}, \tag{3.13}$$

where the mass source term accounts for the mass created per unit time and per unit volume due to the reactive absorption process. The equation (3.13) can be rewritten using vector notation as

$$\frac{\partial \rho}{\partial t} + \nabla \cdot \left(\rho \vec{v} \right) = S_{mass}. \tag{3.14}$$

The present model uses the VOF method to solve the tracking of the interface. Since the VOF method solves the same set of mass and momentum conservation equations for both fluids, the density and the viscosity are not constant throughout the domain despite the fact that two incompressible fluids are analysed. Instead, the physical properties are a function of the volume fraction and are calculated using the equations (3.3) and (3.4). Consequently, the divergence of the mass flux can be further developed according to:

$$\nabla \cdot (\rho \vec{v}) = \rho \frac{\partial u}{\partial x} + u \frac{\partial \rho}{\partial x} + \rho \frac{\partial v}{\partial y} + v \frac{\partial \rho}{\partial y} + \rho \frac{\partial w}{\partial z} + w \frac{\partial \rho}{\partial z}. \tag{3.15}$$

Introducing equation (3.15) into the mass balance equation (3.14) yields

$$\frac{\partial \rho}{\partial t} + \rho \frac{\partial u}{\partial x} + u \frac{\partial \rho}{\partial x} + \rho \frac{\partial v}{\partial y} + v \frac{\partial \rho}{\partial y} + \rho \frac{\partial w}{\partial z} + w \frac{\partial \rho}{\partial z} = S_{mass}, \tag{3.16}$$

whose terms can be rearranged to give

$$\frac{\partial \rho}{\partial t} + \rho \left(\frac{\partial u}{\partial x} + \frac{\partial v}{\partial y} + \frac{\partial w}{\partial z} \right) + \left(u \frac{\partial \rho}{\partial x} + v \frac{\partial \rho}{\partial y} + w \frac{\partial \rho}{\partial z} \right) = S_{mass}. \tag{3.17}$$

Using the definition of material derivative the final form of the mass conservation

equation solved in the present model is

$$\frac{D\rho}{Dt} + \rho\left(\frac{\partial u}{\partial x} + \frac{\partial v}{\partial y} + \frac{\partial w}{\partial z}\right) = S_{mass}. \tag{3.18}$$

Or using vector notation,

$$\frac{D\rho}{Dt} + \rho\left(\nabla \cdot \vec{v}\right) = S_{mass}. \tag{3.19}$$

The last expression (3.19) is combined with the momentum conservation equation in the following section 3.2.2. As will be seen, the mass source term also contributes to the momentum balance over the differential volume.

3.2.2 Momentum conservation equation

The momentum conservation equation results from applying Newton's second law of motion to the differential volume of fluid. The sum of all the forces acting on the differential volume must equal the material derivative of linear momentum of the differential volume according to

$$\sum\left(\vec{F}_{body} + \vec{F}_{surface} + \vec{F}_{additional}\right) = \frac{D\left(\vec{v}dm\right)}{Dt}, \tag{3.20}$$

where gravity is included as the only body force $\vec{F}_{body}$. The additional term $\vec{F}_{additional}$ accounts for the surface tension, which is included as a momentum source term.

For a Newtonian, incompressible fluid, the Cauchy stress tensor is used to calculate the surface forces $\vec{F}_{surface}$. Pressure and viscous stresses are considered (Figure 3.2) as shown in the following equation

$$\begin{bmatrix} \sigma_{xx} & \tau_{xy} & \tau_{xz} \\ \tau_{yx} & \sigma_{yy} & \tau_{yz} \\ \tau_{zx} & \tau_{zy} & \sigma_{zz} \end{bmatrix} = \begin{bmatrix} -p & 0 & 0 \\ 0 & -p & 0 \\ 0 & 0 & -p \end{bmatrix} + \mu \left(\nabla \vec{v} + \nabla \vec{v}^T \right), \tag{3.21}$$

with the viscous stress tensor being

$$\nabla \vec{v} = \nabla \vec{v}^T = \begin{bmatrix} \frac{\partial u}{\partial x} & \frac{1}{2}\left(\frac{\partial u}{\partial y} + \frac{\partial v}{\partial x}\right) & \frac{1}{2}\left(\frac{\partial u}{\partial z} + \frac{\partial w}{\partial x}\right) \\ \frac{1}{2}\left(\frac{\partial u}{\partial y} + \frac{\partial v}{\partial x}\right) & \frac{\partial v}{\partial y} & \frac{1}{2}\left(\frac{\partial v}{\partial z} + \frac{\partial w}{\partial y}\right) \\ \frac{1}{2}\left(\frac{\partial u}{\partial z} + \frac{\partial w}{\partial x}\right) & \frac{1}{2}\left(\frac{\partial v}{\partial z} + \frac{\partial w}{\partial y}\right) & \frac{\partial w}{\partial z} \end{bmatrix}. \tag{3.22}$$

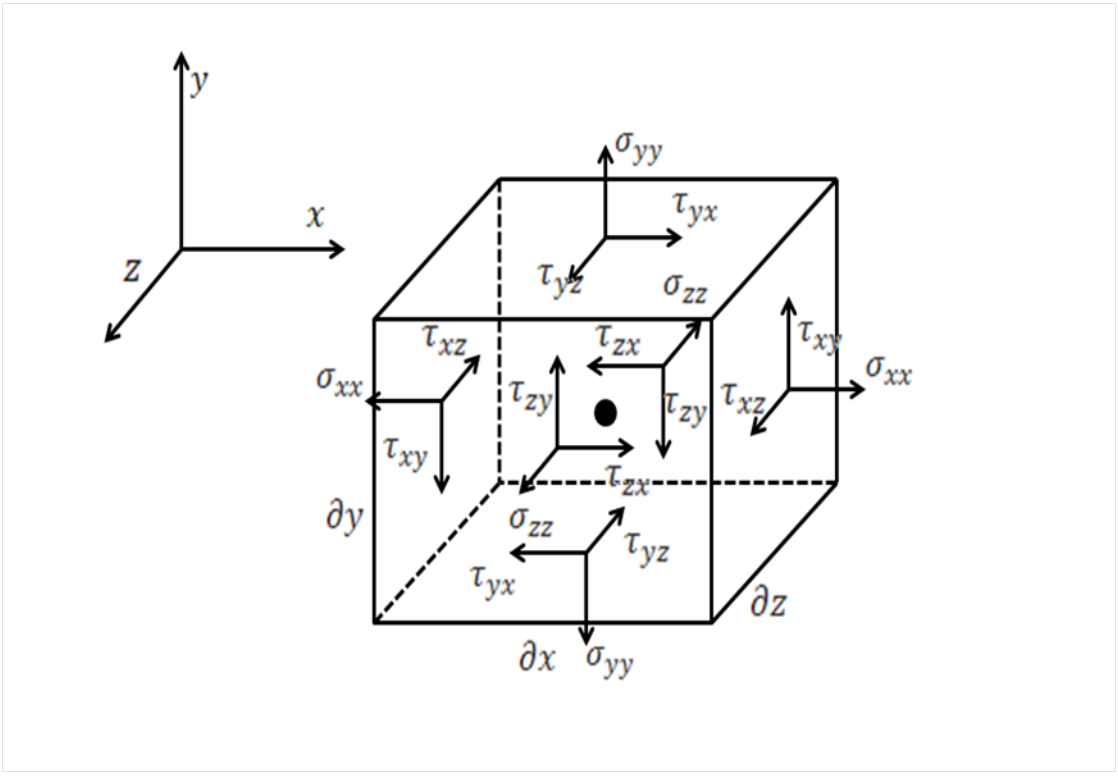

Figure 3.2: Cauchy stress tensor.

The surface forces can be obtained from the values of the stresses at the centre of the differential volume using Taylor expansion series. For instance, for the normal force in the positive x-direction is

$$\vec{F}_{xx}^{+} = \left(\sigma_{xx} + \frac{\partial \sigma_{xx}}{\partial x} \frac{\partial x}{2} \right) \partial y \partial z, \tag{3.23}$$

and in the negative direction is

$$\vec{F}_{xx}^{-} = \left(\sigma_{xx} - \frac{\partial \sigma_{xx}}{\partial x} \frac{\partial x}{2} \right) \partial y \partial z. \tag{3.24}$$

Therefore, balancing the normal surface forces in the x direction we obtain

$$\vec{F}_{xx}^{+} - \vec{F}_{xx}^{-} = \frac{\partial \sigma_{xx}}{\partial x} \partial x \partial y \partial z. \tag{3.25}$$

Analogously, for the rest of normal and tangential forces acting on the differential volume the expressions are

$$\vec{F}_{yy}^{+} - \vec{F}_{yy}^{-} = \frac{\partial \sigma_{yy}}{\partial y} \partial x \partial y \partial z, \tag{3.26}$$

$$\vec{F}_{zz}^{+} - \vec{F}_{zz}^{-} = \frac{\partial \sigma_{zz}}{\partial z} \partial x \partial y \partial z, \tag{3.27}$$

$$\vec{F}_{xy}^{+} - \vec{F}_{xy}^{-} = \frac{\partial \tau_{xy}}{\partial x} \partial x \partial y \partial z, \tag{3.28}$$

$$\vec{F}_{yx}^{+} - \vec{F}_{yx}^{-} = \frac{\partial \tau_{yx}}{\partial y} \partial x \partial y \partial z, \tag{3.29}$$

$$\vec{F}_{xz}^{+} - \vec{F}_{xz}^{-} = \frac{\partial \tau_{xy}}{\partial x} \partial x \partial y \partial z, \tag{3.30}$$

$$\vec{F}_{zx}^{+} - \vec{F}_{zx}^{-} = \frac{\partial \tau_{zx}}{\partial z} \partial x \partial y \partial z, \tag{3.31}$$

$$\vec{F}_{yz}^{+} - \vec{F}_{yz}^{-} = \frac{\partial \tau_{yz}}{\partial y} \partial x \partial y \partial z, \tag{3.32}$$

and

$$\vec{F}_{zy}^{+} - \vec{F}_{zy}^{-} = \frac{\partial \tau_{zy}}{\partial z} \partial x \partial y \partial z. \tag{3.33}$$

Taking the partial derivatives of the surface stresses, and combining with equations (3.21) and (3.22) the following expressions are obtained

$$\frac{\partial \sigma_{xx}}{\partial x} = \left(-\frac{\partial p}{\partial x} + 2\mu \frac{\partial^2 u}{\partial x^2} + 2\frac{\partial \mu}{\partial x}\frac{\partial u}{\partial x} \right), \tag{3.34}$$

$$\frac{\partial \sigma_{yy}}{\partial y} = \left(-\frac{\partial p}{\partial y} + 2\mu \frac{\partial^2 v}{\partial y^2} + 2\frac{\partial \mu}{\partial y}\frac{\partial v}{\partial y} \right), \tag{3.35}$$

$$\frac{\partial \sigma_{zz}}{\partial z} = \left(-\frac{\partial p}{\partial z} + 2\mu \frac{\partial^2 w}{\partial z^2} + 2\frac{\partial \mu}{\partial z}\frac{\partial w}{\partial z} \right), \tag{3.36}$$

$$\frac{\partial \tau_{xy}}{\partial x} = \left[\frac{\partial \mu}{\partial x}\left(\frac{\partial u}{\partial y} + \frac{\partial v}{\partial x} \right) + \mu \left(\frac{\partial^2 u}{\partial x \partial y} + \frac{\partial^2 v}{\partial x^2} \right) \right], \tag{3.37}$$

$$\frac{\partial \tau_{yx}}{\partial y} = \left[\frac{\partial \mu}{\partial y}\left(\frac{\partial u}{\partial y} + \frac{\partial v}{\partial x} \right) + \mu \left(\frac{\partial^2 v}{\partial y \partial x} + \frac{\partial^2 u}{\partial y^2} \right) \right], \tag{3.38}$$

$$\frac{\partial \tau_{xz}}{\partial x} = \left[\frac{\partial \mu}{\partial x}\left(\frac{\partial u}{\partial z} + \frac{\partial w}{\partial x} \right) + \mu \left(\frac{\partial^2 u}{\partial x \partial z} + \frac{\partial^2 w}{\partial x^2} \right) \right], \tag{3.39}$$

$$\frac{\partial \tau_{zx}}{\partial z} = \left[\frac{\partial \mu}{\partial z}\left(\frac{\partial u}{\partial z} + \frac{\partial w}{\partial x} \right) + \mu \left(\frac{\partial^2 w}{\partial z \partial x} + \frac{\partial^2 u}{\partial z^2} \right) \right], \tag{3.40}$$

$$\frac{\partial \tau_{yz}}{\partial y} = \left[\frac{\partial \mu}{\partial y}\left(\frac{\partial v}{\partial z}+\frac{\partial w}{\partial y}\right)+\mu\left(\frac{\partial^2 v}{\partial y \partial z}+\frac{\partial^2 w}{\partial y^2}\right)\right], \tag{3.41}$$

and

$$\frac{\partial \tau_{zy}}{\partial z} = \left[\frac{\partial \mu}{\partial z}\left(\frac{\partial v}{\partial z}+\frac{\partial w}{\partial y}\right)+\mu\left(\frac{\partial^2 w}{\partial z \partial y}+\frac{\partial^2 v}{\partial z^2}\right)\right]. \tag{3.42}$$

Adding all the surface forces acting on the x-axis one obtains

$$\begin{aligned}\sum \vec{F}_{surface,x} &= \left[-\frac{\partial p}{\partial x}+2\mu\frac{\partial^2 u}{\partial x^2}+2\frac{\partial \mu}{\partial x}\frac{\partial u}{\partial x}+\frac{\partial \mu}{\partial y}\left(\frac{\partial u}{\partial y}+\frac{\partial v}{\partial x}\right)\right.\\ &\left.+\mu\left(\frac{\partial^2 v}{\partial y \partial x}+\frac{\partial^2 u}{\partial y^2}\right)+\frac{\partial \mu}{\partial z}\left(\frac{\partial u}{\partial z}\frac{\partial w}{\partial x}\right)+\mu\left(\frac{\partial^2 w}{\partial z \partial x}+\frac{\partial^2 u}{\partial z^2}\right)\right]dV\\ &= \left[-\frac{\partial p}{\partial x}+\mu\left(\frac{\partial^2 u}{\partial x^2}+\frac{\partial^2 u}{\partial y^2}+\frac{\partial^2 u}{\partial z^2}\right)+\mu\frac{\partial}{\partial x}\left(\frac{\partial u}{\partial x}+\frac{\partial v}{\partial y}+\frac{\partial w}{\partial z}\right)\right.\\ &\left.+2\frac{\partial \mu}{\partial x}\frac{\partial u}{\partial x}+\frac{\partial \mu}{\partial y}\left(\frac{\partial u}{\partial y}+\frac{\partial v}{\partial x}\right)+\frac{\partial \mu}{\partial z}\left(\frac{\partial u}{\partial z}+\frac{\partial w}{\partial x}\right)\right]dV,\end{aligned} \tag{3.43}$$

analogously for the y-axis,

$$\begin{aligned}\sum \vec{F}_{surface,y} = \Bigg[&-\frac{\partial p}{\partial y}+\mu\left(\frac{\partial^2 v}{\partial x^2}+\frac{\partial^2 v}{\partial y^2}+\frac{\partial^2 v}{\partial z^2}\right)+\mu\frac{\partial}{\partial y}\left(\frac{\partial u}{\partial x}+\frac{\partial v}{\partial y}+\frac{\partial w}{\partial z}\right)\\ &+2\frac{\partial \mu}{\partial y}\frac{\partial v}{\partial y}+\frac{\partial \mu}{\partial x}\left(\frac{\partial u}{\partial y}+\frac{\partial v}{\partial x}\right)+\frac{\partial \mu}{\partial z}\left(\frac{\partial v}{\partial z}+\frac{\partial w}{\partial y}\right)\Bigg]dV,\end{aligned} \tag{3.44}$$

and for the z-axis,

$$\begin{aligned}\sum \vec{F}_{surface,z} = \Bigg[&-\frac{\partial p}{\partial z}+\mu\left(\frac{\partial^2 w}{\partial x^2}+\frac{\partial^2 w}{\partial y^2}+\frac{\partial^2 w}{\partial z^2}\right)+\mu\frac{\partial}{\partial z}\left(\frac{\partial u}{\partial x}+\frac{\partial v}{\partial y}+\frac{\partial w}{\partial z}\right)\\ &+2\frac{\partial \mu}{\partial z}\frac{\partial w}{\partial z}+\frac{\partial \mu}{\partial x}\left(\frac{\partial u}{\partial z}+\frac{\partial w}{\partial x}\right)+\frac{\partial \mu}{\partial y}\left(\frac{\partial v}{\partial z}+\frac{\partial w}{\partial y}\right)\Bigg]dV.\end{aligned} \tag{3.45}$$

On the one hand, adding all the forces acting on the differential volume and using vector notation, i.e. left-hand side of the equation (3.20), one obtains

$$\begin{aligned} &\sum \left(\vec{F}_{body} + \vec{F}_{surface} + \vec{F}_{additional}\right) \\ &= \left(-\nabla p + \mu\nabla^2\vec{v} + \mu\nabla\left(\nabla\cdot\vec{v}\right) + \vec{S}_\mu + \rho\vec{g} + \vec{S}_\sigma\right)dV. \end{aligned} \tag{3.46}$$

All the terms that include the derivatives of the viscosity have been gathered into a single momentum source term $\vec{S}_\mu$, which constitutes an additional source of linear momentum due to the variation in viscosity, and is expressed as

$$\begin{aligned} \vec{S}_\mu = &\left[2\frac{\partial\mu}{\partial x}\frac{\partial u}{\partial x} + \frac{\partial\mu}{\partial y}\left(\frac{\partial u}{\partial y} + \frac{\partial v}{\partial x}\right) + \frac{\partial\mu}{\partial z}\left(\frac{\partial u}{\partial z} + \frac{\partial w}{\partial x}\right)\right]\vec{i} \\ &+\left[2\frac{\partial\mu}{\partial y}\frac{\partial v}{\partial y} + \frac{\partial\mu}{\partial x}\left(\frac{\partial u}{\partial y} + \frac{\partial v}{\partial x}\right) + \frac{\partial\mu}{\partial z}\left(\frac{\partial v}{\partial z} + \frac{\partial w}{\partial y}\right)\right]\vec{j} \\ &+\left[2\frac{\partial\mu}{\partial z}\frac{\partial w}{\partial z} + \frac{\partial\mu}{\partial x}\left(\frac{\partial u}{\partial z} + \frac{\partial w}{\partial x}\right) + \frac{\partial\mu}{\partial y}\left(\frac{\partial v}{\partial z} + \frac{\partial w}{\partial y}\right)\right]\vec{k}. \end{aligned} \tag{3.47}$$

In addition, equation (3.46) includes the surface tension momentum source term $\vec{S}_\sigma$, which is modelled according to the Continuum Surface Force (CSF) model introduced by Brackbill et al [168]:

$$S_\sigma = \sigma\frac{\rho\kappa\nabla\alpha_i}{\frac{1}{2}\left(\rho_l + \rho_g\right)}, \tag{3.48}$$

where the density ρ is obtained as volume fraction averaged according to equation (3.3) and the curvature can be obtained as the divergence of the unitary vector perpendicular to the interface $\vec{n}$ according to

$$\kappa = \nabla\cdot\vec{n}. \tag{3.49}$$

A contact angle θ is included to describe the liquid-solid adhesion. A correction for the normal direction is incorporated as a function of the established contact angle for the computational cell next to the solid wall as

$$\vec{n} = \vec{n}_{wall} cos\theta + \vec{t}_{wall} sin\theta. \tag{3.50}$$

In the equation (3.50), $\vec{n}_{wall}$ and $\vec{t}_{wall}$ denote respectively the normal and tangent vectors to the wall.

The CSF model presents the drawback of the phenomenon called parasitic currents, which causes abnormal values of the velocity at the interface due to a wrong evaluation of the curvature. Some anomalous velocities were observed at the early stages of the present simulations. However, the effect disappeared after the pseudo-steady state was reached.

On the other hand, the material derivative of the linear momentum equation, i.e. right-hand side of equation (3.20), reads as follows:

$$\begin{aligned} \frac{D(\vec{v}dm)}{Dt} &= \left[\frac{\partial(\rho\vec{v})}{\partial t} + \vec{v}\cdot\nabla(\rho\vec{v})\right]dV \\ &= \left[\vec{v}\frac{\partial\rho}{\partial t} + \rho\frac{\partial\vec{v}}{\partial t} + u\frac{\partial(\rho\vec{v})}{\partial x} + v\frac{\partial(\rho\vec{v})}{\partial y} + w\frac{\partial(\rho\vec{v})}{\partial z}\right]dV, \end{aligned} \tag{3.51}$$

where $dm = \rho dV$.

Further developing the partial derivatives in equation (3.51) we obtain

$$\begin{aligned} \frac{D(\rho\vec{v})}{Dt} = \left[\vec{v}\frac{\partial\rho}{\partial t} + \rho\frac{\partial\vec{v}}{\partial t} + u\left(\frac{\partial\rho}{\partial x}\vec{v} + \rho\frac{\partial\vec{v}}{\partial x}\right) + v\left(\frac{\partial\rho}{\partial y}\vec{v} + \rho\frac{\partial\vec{v}}{\partial y}\right)\right. \\ \left. + w\left(\frac{\partial\rho}{\partial z}\vec{v} + \rho\frac{\partial\vec{v}}{\partial z}\right)\right], \end{aligned} \tag{3.52}$$

which can be rearranged as:

$$\begin{aligned}\frac{D(\rho\vec{v})}{Dt} = \Bigg[\vec{v}\left(\frac{\partial\rho}{\partial t}+u\frac{\partial\rho}{\partial x}+v\frac{\partial\rho}{\partial y}+w\frac{\partial\rho}{\partial z}\right)\\ +\rho\left(\frac{\partial\vec{v}}{\partial t}+u\frac{\partial\vec{v}}{\partial x}+v\frac{\partial\vec{v}}{\partial y}+w\frac{\partial\vec{v}}{\partial z}\right)\Bigg].\end{aligned} \tag{3.53}$$

Or, in vector notation and using the concept of material derivative:

$$\frac{D(\rho\vec{v})}{Dt} = \vec{v}\frac{D\rho}{Dt}+\rho\frac{D\vec{v}}{Dt}. \tag{3.54}$$

Combining the equations (3.19) and (3.54), it can be concluded that the acceleration of the differential volume is a function of the mass source term as

$$\frac{D(\rho\vec{v})}{Dt} = \vec{v}S_{mass}-\vec{v}\rho\left(\nabla\cdot\vec{v}\right)+\rho\frac{D\vec{v}}{Dt}. \tag{3.55}$$

Finally, the conservation equation governing the present model is obtained equating (3.46) to (3.55):

$$-\nabla p+\mu\nabla^2\vec{v}+\mu\nabla\left(\nabla\cdot\vec{v}\right)+\vec{S}_\mu+\rho\vec{g}+\vec{S}_\sigma = \rho\frac{\partial\vec{v}}{\partial t}+\vec{v}S_{mass}. \tag{3.56}$$

The acceleration of the differential volume, i.e. right-hand side of the equation (3.56), is the result of adding two components: one caused by the mass variation and the other by the variation in the velocity vector associated to the differential volume. The result is thus analogous to the application of Newton's second law to a variable-mass system.

3.3 Mass transfer source term

The mass transfer source term S_{mass} that appears in the equation (3.56) is obtained according to Higbie's theory. This theory is based on the concept of exposure time. According to this concept, a mass differential element is exposed to the gas phase during a limited amount of time, i.e. the exposure time, after which it returns to the liquid bulk. The mass transfer through the gas-liquid interface takes place during the exposure time. This approach describes the absorption as an unsteady process, which appears to be more suitable for the transient simulations performed in the present work. Therefore, the mass balance over a differential volume assuming unidirectional diffusion gives the following PDE for the concentration of the absorbed species c as a function of time and the distance from the interface, i.e. $x = 0$ in the interface and $x = \infty$ in the bulk of the liquid:

$$\frac{\partial c}{\partial t} = D\frac{\partial^2 c}{\partial x^2}, \tag{3.57}$$

with the following initial

$$c = 0 \quad , \quad \begin{matrix} t = 0 \\ x \geq 0, \end{matrix} \tag{3.58}$$

and boundary conditions

$$c = c_{l,int} \quad , \quad \begin{matrix} t > 0 \\ x = 0, \end{matrix} \tag{3.59}$$

and

$$c = 0 \quad , \quad \begin{matrix} t > 0 \\ x = \infty. \end{matrix} \tag{3.60}$$

The following variable change needs to be applied in order to solve equation (3.57):

$$\eta = \frac{x}{\sqrt{4Dt}}. \tag{3.61}$$

Applying the chain rule the partial derivatives in equation (3.57) can be expressed as

$$\frac{\partial c}{\partial t} = \frac{\partial c}{\partial \eta} \cdot \frac{\partial \eta}{\partial t} = \frac{\partial c}{\partial \eta} \cdot \frac{-\eta}{2t}, \tag{3.62}$$

and

$$\frac{\partial^2 c}{\partial x^2} = \frac{\partial}{\partial \eta} \cdot \frac{\partial \eta}{\partial x} \left(\frac{\partial c}{\partial \eta} \cdot \frac{\partial \eta}{\partial x} \right) = \frac{\partial^2 c}{\partial \eta^2} \cdot \left(\frac{1}{4Dt} \right). \tag{3.63}$$

Introducing the expressions (3.62) and (3.63) into Fick's second law (3.57), we obtain

$$\frac{\partial c}{\partial \eta} \cdot \left(\frac{-\eta}{2t} \right) = D \frac{\partial^2 c}{\partial \eta^2} \left(\frac{1}{4Dt} \right), \tag{3.64}$$

which can be rearranged as

$$\frac{\partial^2 c}{\partial \eta^2} + 2\eta \frac{\partial c}{\partial \eta} = 0. \tag{3.65}$$

If $P = dc/d\eta$, then equation (3.65) yields

$$\frac{dP}{d\eta} + 2\eta P = 0. \tag{3.66}$$

Separating variables and integrating one obtains

$$\int \frac{dP}{P} + \int 2\eta d\eta = 0. \tag{3.67}$$

The following solution is found

$$ln\frac{P}{c_1} = -\eta^2, \tag{3.68}$$

from which

$$\frac{dc}{d\eta} = c_1 e^{-\eta^2}. \tag{3.69}$$

Integrating equation (3.69) we obtain

$$c = c_1 erf\big(\eta\big) + c_2. \tag{3.70}$$

The integration constants c_1 and c_2 are obtained applying the boundary conditions expressed in equations (3.59) and (3.60), which results in

$$c_{l,int} = c_2 = -c_1. \tag{3.71}$$

Finally, the solution to Fick's second law is the following concentration c profile

$$c = c_{l,int} erfc\big(\eta\big). \tag{3.72}$$

On the other hand, Fick's first law calculates the mass flux J through the interface as

$$J = -D\frac{\partial c}{\partial x}\bigg|_{x=0} = -D\left(\frac{\partial c}{\partial \eta}\cdot\frac{\partial \eta}{\partial x}\right)\bigg|_{x=0}. \tag{3.73}$$

Introducing the expressions of the partial derivatives $\frac{\partial c}{\partial \eta}$ and $\frac{\partial \eta}{\partial x}$ we obtain

$$J = Dc_{l,int}\left(\frac{1}{\sqrt{4Dt}}\right) = c_{l,int}\sqrt{\frac{D}{4t}}. \tag{3.74}$$

The equation (3.74) will be used afterwards to obtain the liquid-side mass transfer

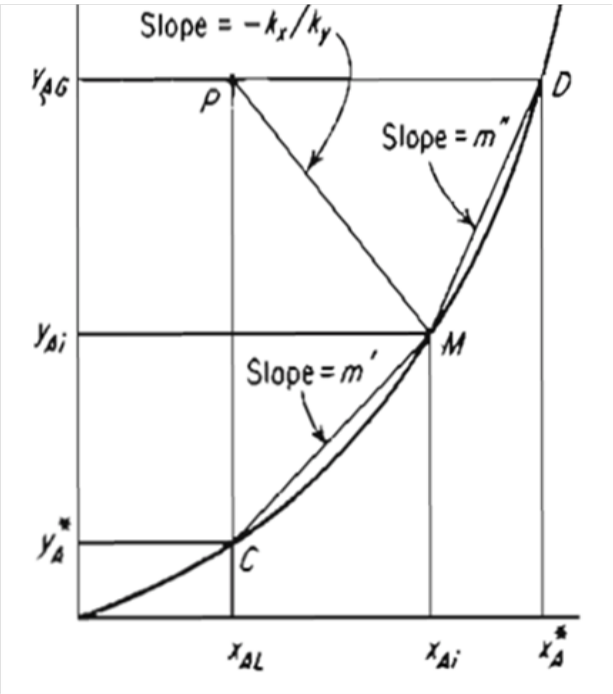

Figure 3.3: Theoretical equilibrium solubility curve. In this figure the concentrations in the bulk of the liquid and gas are denoted as x_{AL} and y_{AG}, respectively. The concentrations in the interface are y_{Ai} and x_{Ai}. The superscript * denotes values in equilibrium with those in the bulk of both phases [169].

coefficient k_l according to Higbie's theory.

The expression of the mass flux J can also be posed in terms of the overall mass transfer coefficient K_l and the difference in concentration between the concentration in the liquid phase that would be in equilibrium with the concentration in the bulk of the gas phase c_l^* and the concentration in the bulk of the liquid phase $c_{l,bulk}$ as

$$J = K_l\left(c_l^* - c_{l,bulk}\right). \tag{3.75}$$

And considering the slope of the theoretical equilibrium curve (Figure 3.3), equation (3.75) can be reformulated as

$$\frac{1}{K_l} = \frac{c_l^* - c_{l,bulk}}{J} = \frac{c_{g,bulk} - c_{g,int}}{m'' J} + \frac{c_{l,int} - c_{l,bulk}}{J} = \frac{1}{m'' k_g} + \frac{1}{k_l}. \tag{3.76}$$

Equation (3.76) can be interpreted as having two resistances to the mass flow, one corresponding to the gas side $1/m'' k_g$ and the other to the liquid side $1/k_l$.

If the value of m'' is large enough then the gas-side resistance can be neglected and the system is said to be liquid-side controlled. This assumption is valid in systems wherein the solubility of the solute in the liquid phase is small, which translates into a large slope on the equilibrium solubility curve. If pure CO_2 forms the gas phase, then the gas-side resistance can be neglected [170]. Also, $c_{l,bulk}$ can be neglected due to the fast kinetics of the CO_2-MEA reaction. Under those circumstances, the mass flux J is

$$J = k_l \left(c_{l,int} - \cancelto{0}{c_{l,bulk}} \right) . \tag{3.77}$$

The time-dependent liquid-side mass transfer coefficient is, equating (3.74) to (3.77)

$$k_l(t) = \sqrt{\frac{D}{\pi t}}. \tag{3.78}$$

And averaging equation (3.78) over the exposure time τ, one obtains

$$\bar{k}_l = \frac{1}{\tau} \int_0^\tau k_l(t) dt = 2\sqrt{\frac{D}{\pi \tau}}. \tag{3.79}$$

There are several approaches in the literature to calculate the exposure time τ. In this work the expression introduced by Haroun et al [171] is used. The authors calculated it dividing the length of the liquid film $\mathscr{L}$ by the value of the velocity at the interface v_{int} as

$$\tau = \frac{\mathscr{L}}{v_{int}}. \tag{3.80}$$

The mass flux in equation (3.77) can be converted into a mass source term multiplying by the effective area A_{eff}, which is calculated as the module of the gradient of the volume fraction in each computational cell [172] according to

$$A_{eff} = \left|\nabla\alpha\right|. \tag{3.81}$$

Thus, the mass source term S_{mass} yields

$$S_{mass} = k_l A_{eff} c_{l,int}. \tag{3.82}$$

The mass transfer rate is increased when the component being transferred reacts with the liquid phase. The enhancement factor E is defined as the ratio between the mass absorption rate with S_{reac} and without chemical reaction S_{mass}

$$E = \frac{S_{reac}}{k_l A_{eff} c_{l,int}}, \tag{3.83}$$

which renders the following expression for the mass source term:

$$S_{reac} = E k_l A_{eff} c_{l,int}. \tag{3.84}$$

The CO_2-MEA system presents a fast pseudo-first order behaviour by virtue of the high value of its associated Hatta number, i.e. between 26.13 and 65.35 [156]. Under these conditions, the expression that calculates the enhancement factor was introduced by Krevelen and Hoftijzer [174] and is given by

$$E = \frac{\sqrt{M\Big(\big(E_i - E\big)/\big(E_i - 1\big)\Big)}}{tanh\left(\sqrt{M\Big(\big(E_i - E\big)/\big(E_i - 1\big)\Big)}\right)}, \tag{3.85}$$

being M the value of the Hatta number squared and E_i the theoretical enhancement factor for an instantaneous irreversible reaction, which for the case of CO_2 being absorbed into aqueous MEA is given by

$$E_i = \sqrt{\frac{D_{CO_2}}{D_{MEA}}}\left(1+\frac{D_{MEA}c_{MEA}}{zD_{CO_2}c_{l,int}}\right). \tag{3.86}$$

The Hatta number for a general reaction between the components A and B reads [175]

$$Ha = \frac{\sqrt{\Big(2/\big(m+n\big)\Big)K_{m,n}\big[A\big]^{m-1}\big[B\big]^{n}D}}{k_l}. \tag{3.87}$$

For the CO_2-MEA system the value of the parameters m and n are equal to 1, which simplifies equation (3.87) to

$$Ha \simeq \frac{\sqrt{K_f\big[MEA\big]D_{CO_2}}}{k_l}. \tag{3.88}$$

Now, the enhancement factor can be approximated to the value of the Hatta number when the reaction presents the pseudo-first order behaviour as

$$E \simeq Ha. \tag{3.89}$$

Introducing the equations (3.88) and (3.79) into the expression of the mass source term (3.84), and considering that the concentration of solute in the bulk of the liquid phase should be zero by virtue of the high Hatta number, one obtains the final form of the mass source term introduced in the momentum conservation equation as:

$$S_{mass}\big|_{reac} = \left(\frac{\sqrt{K_f\big[MEA\big]D_{CO_2}}}{k_l}\right)\left(2\sqrt{\frac{D_{CO_2}}{\pi\tau}}\right)A_{eff}c_{l,int}. \tag{3.90}$$

An additional mass source term is introduced in the conservation equation to account

for the consumption of reactants and the creation of products of the chemical reaction. Since the carbamate formation is a second order irreversible reaction, the reaction rate r can be calculated as

$$r = K_f \left[MEA\right] \left[CO_2\right]. \tag{3.91}$$

The reaction rate r should be multiplied by the molecular weight of each of the species involved in the reaction (2.5) to obtain their respective mass source terms

$$S_{MEA} = -P_{m,MEA} r, \tag{3.92}$$

$$S_{CO_2} = -P_{m,CO_2} r, \tag{3.93}$$

$$S_{H_2O} = -P_{m,H_2O} r, \tag{3.94}$$

$$S_{MEACOO^+} = P_{m,MEACOO^+} r, \tag{3.95}$$

and

$$S_{H_3O^+} = P_{m,H_3O^+} r. \tag{3.96}$$

3.4 Solubility and diffusivity

The solubility of CO_2 in the aqueous MEA solution is calculated by means of Henry's law:

$$p_{CO_2} = He_{CO_2,M} c_{int,CO_2}. \tag{3.97}$$

The equation (3.97) means that the partial pressure of CO_2 in the gas phase p_{CO_2} is proportional to the solubility of CO_2 into the aqueous amine solution c_{int,CO_2}. The proportionality constant is called Henry's law constant and is denoted as $He_{CO_2,M}$. In this work the method presented by Penttilä et al [138] is used to calculate the Henry's law constant. Their method is based on the N_2O analogy [176]. The Henry's law constant for CO_2 in the aqueous amine solution, i.e. denoted by the subscript M, is calculated as

$$He_{CO_2,M} = He_{N_2O,M}\left(\frac{He_{CO_2,W}}{He_{N_2O,W}}\right), \tag{3.98}$$

being the Henry's constant for both gases, i.e. CO_2 and N_2O, in pure water approximated by the correlation

$$He_W = e^{\left(a+\frac{b}{T}+clnT+dT\right)}. \tag{3.99}$$

Finally, the solubility of N_2O in the aqueous amine solution can be obtained from the following expression valid for binary solvents as

$$He_{N_2O,M} = \sum_{i=1}^{2} He_{N_2O,i} x_i + A_{12}\left[x_1 x_2\right]^2 \left[1 - \frac{T}{B_{12}}\right] e^{(-C_{12}x_2)}, \tag{3.100}$$

where the component 1 is water and 2 is the amine. The Henry's law constant for N_2O in the pure amine is corrected by a series of terms that take into account the mole fraction of both components present in the binary mixture, i.e. x_i. The value for the pure amine is given by

$$He_{N_2O,MEA} = a + bT. \tag{3.101}$$

The value of the constants can be seen in the Table 3.1:

Table 3.1: Parameters for the calculation of the Henry's law constant of CO_2 and N_2O in water and pure MEA

Henry's law constant	a	b	c	d
$He_{N_2O,W}$	158.245	-9048.596	-20.86	-0.00252
$He_{CO_2,W}$	145.369	-8172.355	-19.303	
$He_{N_2O,MEA}$	-9172.5	39.598		

The constants in Table 3.2 are also needed for binary mixtures such as the one considered in the present work, i.e. aqueous MEA:

Table 3.2: Parameters for the calculation of the Henry's law constant in the H_2O-MEA binary mixture

A_{12}	B_{12}	C_{12}
3524641.533	324.718	13.219

The Wilke-Chang equation is used to calculate the value of the CO_2 diffusivity D within the liquid phase. This model presents the diffusivity as a function of both the temperature T and the viscosity μ of the liquid through which it diffuses. In this way, the effect of the variation in the concentration of MEA, which affects the liquid viscosity, on the hydrodynamics and the mass transfer performance can be assessed. The Wilke-Chang equation reads [177]:

$$D = \frac{7.4 \times 10^{-8} \left(\Theta P_m\right)^{1/2} T}{\mu V_m^{0.6}}. \tag{3.102}$$

In equation (3.102), the symbol Θ denotes the association parameter of water whose value is 2.6. The parameter V_m is the molar volume of solute.

3.5 Pressure drop in structured packing columns

Pressure drop constitutes an important energy penalty in the operation of a post-combustion CCS facility. Pressure drop calculations are divided into wet pressure drop and dry pressure drop, depending on whether or not the presence of the liquid is considered. The theory associated to the pressure drop within a structured packing column is presented in this section.

Pressure drop is a measure of the energy loss in the fluid during its transportation through a duct. This energy loss represents the main economic penalty in a CCS post-combustion facility along with the cost of the amine regeneration [102]. The pressure loss in the column is described with an expression analogous to the Darcy-Weisbach equation. Therefore, it is calculated as the product between the kinetic energy of the fluid and a friction factor ζ_{total} which is characteristic of the particular geometry of the duct. Its expression is

$$\Delta p = \zeta_{total} \frac{\rho_g v_{g,eff}^2}{2}. \tag{3.103}$$

The effective gas velocity $v_{g,eff}$ in equation (3.103) is related to the gas superficial velocity and corrected by the void fraction and the geometry of the packing. For wet conditions, i.e. liquid phase involved, the effective velocity can be thus obtained as

$$v_{g,eff} = \frac{v_g}{\varepsilon\left(1-h_l\right) sin\varphi}, \tag{3.104}$$

where φ represents the inclination angle of the solid surface with respect to the vertical direction. The term $\varepsilon\left(1-h_l\right)$ is the porosity of the packing corrected by the presence of the liquid, this is to say, the variation on the space available for the gas to flow. The parameter h_l is the liquid hold-up, which is defined as the volume of liquid per unit volume

of packing. Therefore, an increase in the liquid hold-up causes a diminution in this term, resulting in a higher $v_{g,eff}$ and pressure drop. The most frequently used model to calculate the liquid hold-up inside the packing assumes that the liquid forms a perfectly developed liquid film that fully covers the packing wall. Under these conditions, the liquid hold-up can be calculated as the product of the specific area of the packing A_{spf} and the liquid film thickness δ_l as

$$h_l = A_{spf}\delta_l, \tag{3.105}$$

where the liquid film thickness is obtained according to Nusselt theory [178] as

$$\delta_l = \left(\frac{3\mu_l}{\rho g cos\varphi}\right)^{1/2}. \tag{3.106}$$

The total friction factor in equation (3.103) can be decomposed into a turbulent friction term and the drag term, according to Olujić et al [179]

$$\zeta_{total} = \zeta_{turb} + \zeta_{drag}. \tag{3.107}$$

The turbulent friction factor ζ_{turb} accounts for as much as 70% of the total loss and it can be modelled with CFD meso-scale simulations. The turbulent friction component is caused by the turbulence of the gas whereas the drag component represents the loss of energy due to direction changes caused by sharp bends when the gas flow interacts with the solid walls.

The equation proposed by Said et al [93] for the turbulent friction term is

$$\zeta_{turb} = \left(\frac{C_1}{Re_g^{n_1}} + \frac{C_2}{Re_g^{n_2}}\right)^{n_3}. \tag{3.108}$$

The Reynolds number Re_g is calculated as a function of the channel height h_c and the

gas effective velocity $v_{g,eff}$ according to

$$Re_g = \frac{\rho_g v_{g,eff} h_c}{\mu_g}. \tag{3.109}$$

The exponents n_1, n_2, and n_3 in the equation (3.108) are constants for any geometry of the packing but the coefficients C_1 and C_2 depend on the channel dimensions h_c and b_c according to

$$C_1 = \theta_1 h_c^{\theta_2} b_c^{\theta_3}, \tag{3.110}$$

and

$$C_2 = \omega_1 h_c^{\omega_2} b_c^{\omega_3} + \omega_4 h_c^{\omega_5} b_c^{\omega_6}. \tag{3.111}$$

The parameters used in equations (3.108), (3.110), and (3.111) can be found in Table 3.3:

Table 3.3: Constant parameters. Calculation of the friction factor for air as the gas phase.

Parameter	Value
n_1	0.0166
n_2	0.29688
n_3	4.3645
θ_1	0.883
θ_2	-0.1281
θ_3	0.1723
ω_1	0.209
ω_2	-0.3778
ω_3	0.03738
ω_4	0.684
ω_5	0.976
ω_6	-0.9991

Separately, the drag coefficient ζ_{drag} was correlated with the following equation (3.112),

specific for the commercial packing MonztPak B1-250M, which is the type of packing used in this work. The correlation considers the presence of the liquid phase, but they can also be used for dry conditions when v_l, h_l, and δ_l are equal to zero:

$$\zeta_{drag} = 1.76\left(cos\varphi\right)^{1.63} + \psi\frac{4092v_l^{0.31} + 4715\left(cos\varphi\right)^{0.445}}{Re_g} + \psi 34.19v_l^{0.44}\left(cos\varphi\right)^{0.779}, \tag{3.112}$$

where ψ is the fraction of channels ending at the column wall. This parameter is obtained from the geometry of the packing as

$$\psi = \frac{2h_c}{\pi d_c^2 tan\varphi}\left(d_c^2 - \frac{h_c^2}{\left(tan\varphi\right)^2}\right) + \frac{2}{\pi}arcsin\left(\frac{h_c}{d_c tan\varphi}\right). \tag{3.113}$$

The Reynolds number in equation (3.112) is calculated according to

$$Re_g = \frac{v_g}{sin\varphi\left(\varepsilon - h_l\right)}\frac{\rho_g d_c}{\mu_g}, \tag{3.114}$$

where the hydraulic diameter of the channel is

$$d_c = \frac{\frac{\left(b_c h_c - 2\delta_l s_c\right)^2}{b_c h_c}}{\left(\left(\frac{b_c h_c - 2\delta_l s_c}{2h_c}\right)^2 + \left(\frac{b_c h_c - 2\delta_l s_c}{b_c}\right)^2\right)^{0.5} + \frac{b_c h_c - 2\delta_l s_c}{2h_c}}, \tag{3.115}$$

being s_c, the channel side dimension.

The pressure drop correlation described above is used to compare the results from the meso-scale simulations presented in Chapter 7, prior to the analysis of the liquid hold-up and the interfacial area.

Chapter 4

Verification and Validation

A distinction between verification and validation of a CFD code needs to be established. Verification deals with how well the equations have been solved, that is to say, it has to do with numerical uncertainty and is a purely mathematical issue. Validation establishes how well the physics of a particular problem have been represented in the model. According to Blottner [180]:

- *"Verification is solving the equations right"* and,
- *"Validation is solving the right equations"*.

The remarkable growth in computational capacity seen in the last decades has given way to a parallel increase in the pretensions of CFD modelers, who aim at including more and more complicated physics to their calculations at the expense of numerical accuracy. Quoting Roache [181]: *"CFD practitioners have often focused on qualitative simulation of the next more difficult problem class, rather than on achieving quantitative accuracy on the previous problem class".* The author points out that the result from this tendency is a decrease in the quality of the CFD work published and, as a matter of fact, it has become difficult to find systematic assessment of verification and validation in CFD publications.

This work is aimed at exploring new capabilities of CFD techniques by implementing reactive mass transfer into VOF multiphase simulations. However, a verification and validation assessment are also included in order to quantify how a CFD model is capable of representing the physics of this problem.

4.1 Verification

There is a lack of knowledge on the application of systematic grid convergence analysis to multiphase flow CFD simulations. Könözsy et al [209] present a grid convergence study for CFD simulations of microsegregation processes. The importance of the application of such studies in this field lies in the fact that multiphase simulations are computationally expensive hence the search for the optimum grid should be a priority. Grid convergence studies aim at quantifying numerical uncertainty for code verification. The theory used to carry out the present grid convergence study can be found in Roache [182], who proposed the use of a grid convergence index (GCI) based on the Richardson extrapolation [183].

According to the Richardson extrapolation, the numerical solution of a certain variable f can be obtained with the following series that correct the exact value of the variable:

$$f = f_{exact} + g_1 h + g_2 h^2 + g_3 h^3 + h.o.t., \tag{4.1}$$

where g_1, g_2, and g_3 are continuous functions which do not depend on the grid spacing h. The value of g_1 is zero for second order methods.

If one combines two different solutions f_1 and f_2 obtained in two grids h_1 (fine grid) and h_2 (coarse grid), respectively, the following expression is obtained

$$f_{exact} = \frac{f_1 h_2^2 - f_2 h_1^2}{h_2^2 - h_1^2} + h.o.t., \tag{4.2}$$

which can be reduced to the following after dropping the high order terms and introducing the grid refinement ratio $r = h_2/h_1$

$$f_{exact} \cong f_1 + \frac{f_1 - f_2}{r^2 - 1}. \tag{4.3}$$

The expression (4.3) can be generalised for $p-th$ order methods as

$$f_{exact} \cong f_1 + \frac{f_1 - f_2}{r^p - 1}. \tag{4.4}$$

The expression (4.4) says that the exact solution is obtained as the fine grid solution f_1 plus a correction term that depends on the grid refinement ratio r and the difference between the fine and the coarse solutions $f_1 - f_2$.

The equation (4.4) can be then rewritten as

$$f_{exact} \cong f_1\big(1 - E_1\big), \tag{4.5}$$

where the coefficient E_1 is called the Richardson error estimator and is calculated as

$$E_1 = \frac{\varepsilon}{r^p - 1}, \tag{4.6}$$

with ε being

$$\varepsilon = \frac{f_2 - f_1}{f_1}. \tag{4.7}$$

Finally, the grid convergence index (GCI) results from applying a safety factor F_s to the Richardson error estimator E_1. The recommended values of F_s are $F_s = 1.25$ for grid convergence studies with at least three grids and $F_s = 3$ when two grids are considered. The GCI can be applied either to grid values or to solution functionals such as the effective

area considered in this section. Its expression is

$$GCI = F_s \frac{|\varepsilon|}{r^p - 1}. \tag{4.8}$$

Figure 4.1 shows a schematic of the computational domain. The pressure outlet and velocity inlet boundary conditions are used where shown. Non-slip wall conditions with contact angles are set in the rest of the boundaries. The liquid inlet consists of a 0.4 mm thick slot next to the wall. Two different cases are run in this grid convergence study. One case with 45° inclination over the horizontal and 0.38 m/s liquid inlet velocity (case 1), and a second case with 60° and 0.25 m/s (case 2). In both cases the contact angle is set to 70°.

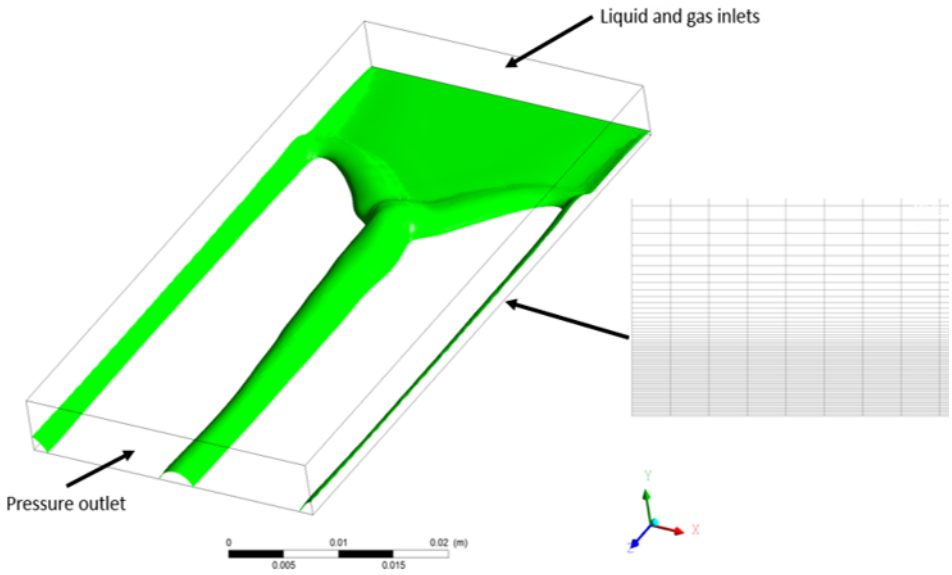

Figure 4.1: Details of the computational domain and the refinement of the mesh next to the wall. The boundary conditions used are shown. The domain consists of a 0.03 m x 0.005 m x 0.06 m inclined metallic plate. The origin of coordinates is placed at the top left corner. The result shown in this figure has been obtained with the mesh *D*, at 0.24 s flow time. Case 2.

Five meshes are used in the present grid convergence study. Table 4.1 shows the

Table 4.1: Number of nodes in each direction and total number of nodes in the five grids tested, i.e. see figure 4.1 to check the directions. The figures in brackets indicate the number of nodes within the 0.4 mm next to the wall.

Grid	Nodes x-dir	Nodes y-dir	Nodes z-dir	Total Nodes
A	35	67(25)	147	344715
B	42	78(30)	177	579852
C	50	93(36)	212	985800
D	60	112(44)	254	1691640
E	72	135(53)	305	2942640

Table 4.2: Spatial discretisation.

Variable	Solution method
Gradient	Least Squares Based
Pressure	PRESTO!
Momentum	Second Order Upwind
Volume fraction	Geo-Reconstruct

Table 4.3: Grid convergence study time resources. The time is expressed in hours of wall time per seconds of flow time.

Grid	Case 1 (h/s).	Case 2 (h/s)
A	14.8	23.3
B	39.5	37.6
C	67.9	64.3
D	124.7	108.2
E	171.7	222.3

Table 4.4: Dimensionless velocity and pressure results for the case 1. The coordinates of the grid point considered are (0.015, 0.0004, 0.03) m.

Grid	Spacing(μm)	Velocity(-)	Pressure (Pa)
A	16.7	1.4578437	18.2929096
B	13.8	1.4505008	18.2207470
C	11.4	1.4445035	18.1901169
D	9.3	1.4383131	18.6943321
E	7.5	1.4372545	18.3000000

Table 4.5: Dimensionless velocity and pressure results for the case 2. The coordinates of the grid point considered are (0.015, 0.0004, 0.01) m.

Grid	Spacing(μm)	Velocity(-)	Pressure (Pa)
A	16.7	1.5971792	23.9937592
B	13.8	1.5856453	25.1172543
C	11.4	1.5799024	24.1832314
D	9.3	1.5814781	24.6741753
E	7.5	1.5807000	25.2052422

details of the structured meshes tested. The same refinement factor $r = 1.2$ is applied to all dimensions in each refining step to get progressively coarser grids.

Table 4.2 shows the solution methods used for spatial discretisation. A first order implicit method is used for time discretisation and the SIMPLE scheme is applied for pressure-velocity coupling. The under-relaxation factors are left at default values. The convergence criterion is set at a value of 0.001 for all the residuals.

Table 4.3 summarises the wall time needed to obtain the solutions for the interfacial area for both cases. All the simulations were run in the Astral HPC facilities at Cranfield University using 3 computing nodes (48 CPUs).

The first variables tested in this grid convergence study are the velocity and the pressure at a particular grid point situated in the area where a fully developed liquid film is observed, i.e. tables 4.4 and 4.5. The values of the velocity and the distance from the wall are non-dimensionalised dividing by the value of the inlet velocity and the dimension of the domain in the y-direction, i.e. 5mm, respectively.

Figure 4.2 shows the velocity profiles at the specified position for case 1 at pseudo-steady state whereas tables 4.4 and 4.5 present the value of the velocity and the pressure at the considered grid point for both cases and all the meshes tested. It can be seen in Figure 4.2 that the five series match for values of the dimensionless distance below 0.1. This happens because the mesh is locally refined in this area as shown in Figure 4.1. This

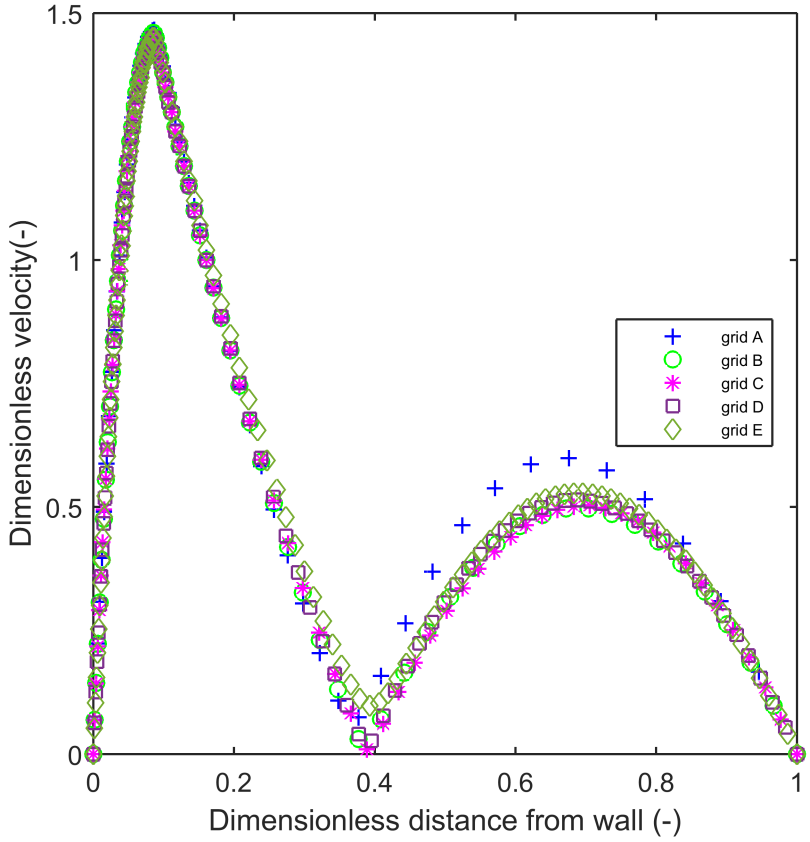

Figure 4.2: Dimensionless velocity profiles in a line placed at x =0.015 m and z =0.03 m. Case 1.

zone corresponds to the liquid phase. However, the difference becomes evident as the distance increases, i.e. distance ranging from 0.4 to 0.8. This area is occupied by the gas phase and it is not as refined as the vicinity of the plate. Figure 4.3 shows how the value of the velocity approximates the exact value as the grid spacing is reduced. Upon these conditions, it is possible to predict the value at zero grid spacing using the Richardson extrapolation, i.e. equation (4.4). However, pressure presents an oscillatory behaviour, i.e. see figure 4.4. The oscillatory behaviour is also observed for the velocity at the grid point considered in case 2.

Table 4.6 shows the values obtained for the results of the grid convergence study using

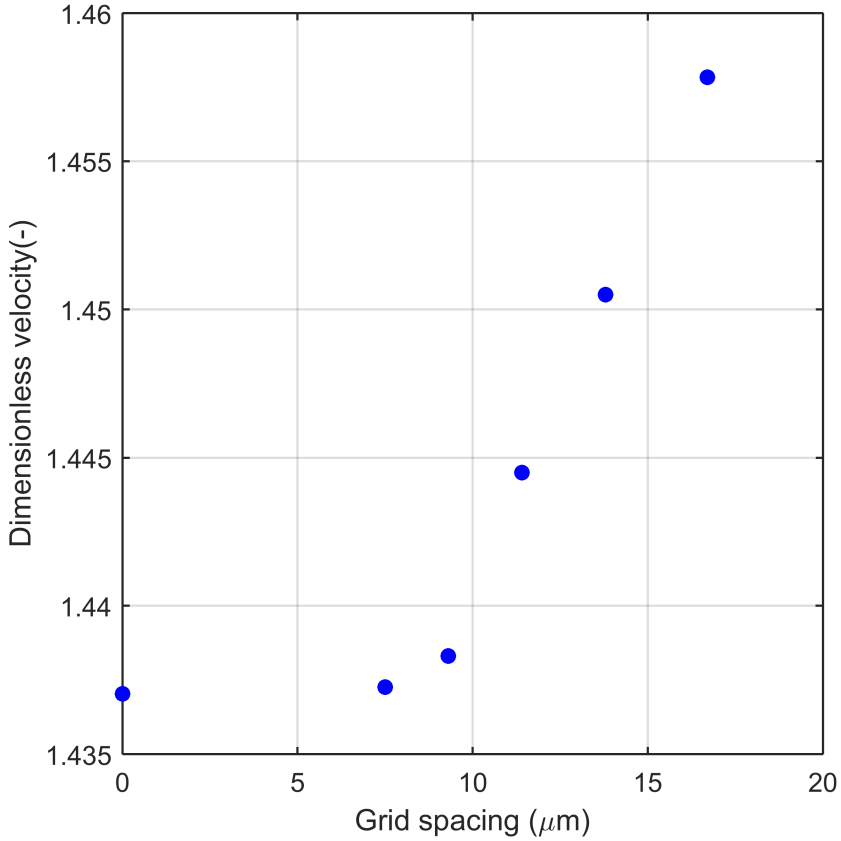

Figure 4.3: Dimensionless velocity vs. grid spacing. The coordinates of the grid point considered are (0.015 m, 0.0004 m, 0.03 m). Case 1.

Table 4.6: Grid convergence test results for the dimensionless velocity. Case 1. Grid point coordinates (0.015 m, 0.0004 m, 0.03 m).

Parameter	Value
Order of conv. p	9.7
Dimensionless. vel at $h = 0$	1.4370361
$GCI_{12}(\%)$	0.018992
$GCI_{23}(\%)$	0.110979
$\frac{GCI_{23}}{r^p GCI_{12}}$	0.999264

the meshes C, D, and E for the velocity of case 1. It can be observed that the results present a high order of convergence and low values of the GCI, which means that the numerical uncertainty is reasonably low. Moreover the quotient $\frac{GCI_{23}}{r^p GCI_{12}}$ presents a value close to

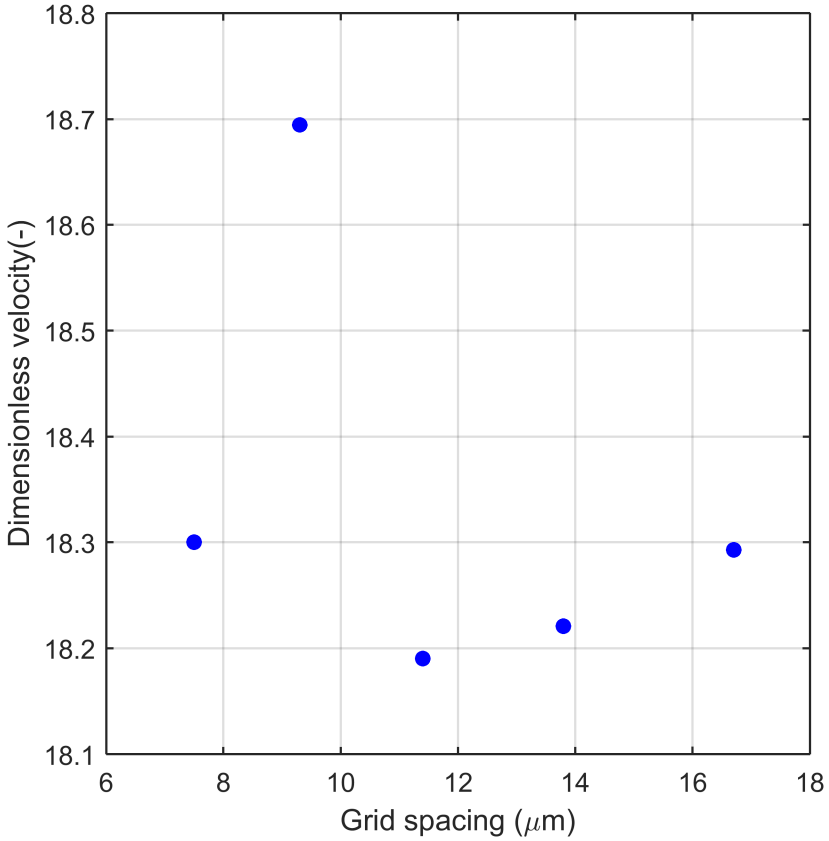

Figure 4.4: Pressure vs. grid spacing. The coordinates of the grid point considered are (0.015 m, 0.0004 m, 0.03 m). Case 1.

Table 4.7: Liquid film thickness calculated for the different meshes tested.

Grid	Case 1 (mm)	Case 2 (mm)
A	0.421000004	0.334663433
B	0.421000004	0.318418752
C	0.421000004	0.320812484
D	0.421000004	0.334883720
E	0.421000004	0.330769224

unity, which indicates that the calculations are well within the asymptotic range.

As was pointed out previously, not only variables at a particular grid point can be subject to the grid convergence study but also solution functionals such as liquid film

thickness or interfacial area. The table 4.7 shows the value of the liquid film thickness at the same position (x =1.5 cm and z =3 cm for case 1 and x =1.5 cm and z =1 cm for case 2) for the five meshes tested. The liquid film thickness is taken as the maximum y-coordinate at which the value of the volume fraction is equal to 1.

As can be observed in table 4.7, the liquid film thickness presents the same values for all the meshes tested.

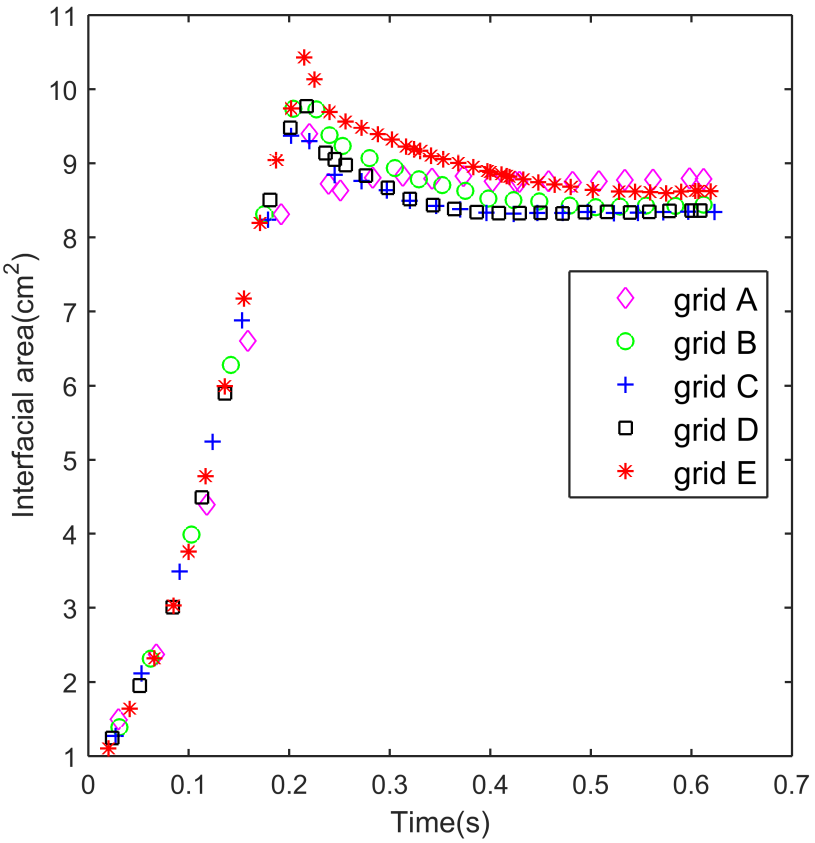

Figure 4.5: Transient evolution of the interfacial area for the five grids tested. Case 2.

The interfacial area is the next parameter studied. The interface is obtained as the isosurface with a value of the volume fraction equal to 0.5. Figure 4.6 shows the liquid flow pattern for the five grids. The difference between the results is not noticeable but

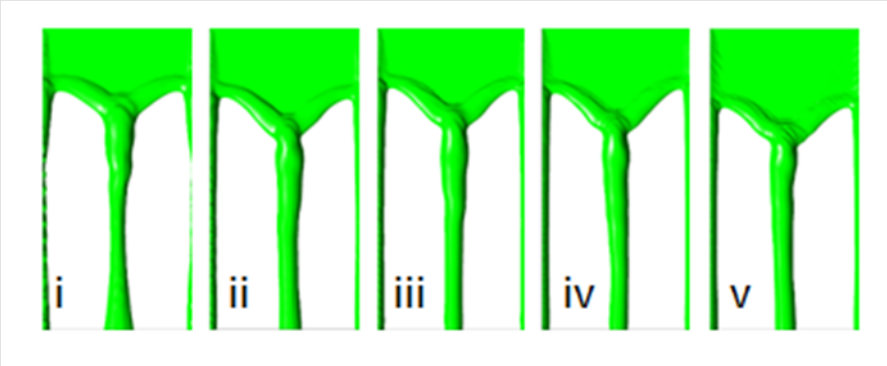

Figure 4.6: Snapshots of the flow patterns for the different grids tested. Case 2. From left to right: i) grid A, ii) grid B, iii) grid C, iv) grid D, and v) grid E. Flow time 0.24 s.

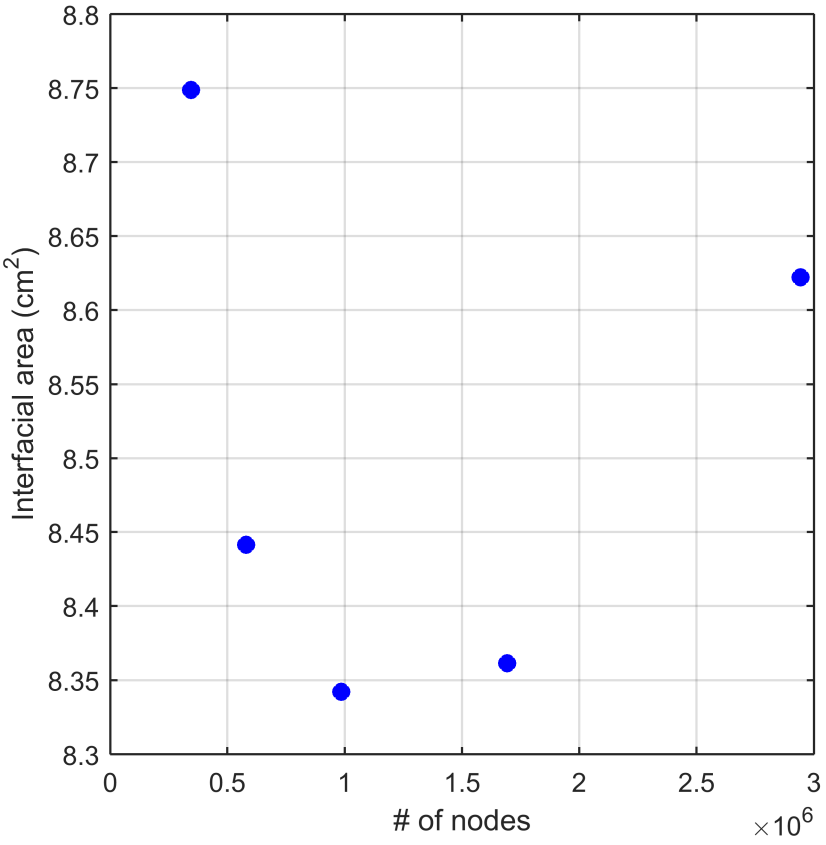

Figure 4.7: Interfacial area vs # of nodes. Case 2.

it becomes evident looking at the transient behaviour observed in figure 4.5. Table 4.8 shows the values of the interfacial area obtained for the different grids tested whereas the oscillatory behaviour presented by this variable can be observed in figure 4.7.

Table 4.8: Value of the interfacial area obtained for the different meshes considered.

Grid	Case 1 (cm^2)	Case 2 (cm^2)
A	17.9308	8.7488
B	16.4050	8.4413
C	16.1420	8.3422
D	17.1771	8.3615
E	17.7906	8.6221

Table 4.9: Specifications of the 2D grids used to check the convergence of the dissolved species mass fraction.

Grid	Nodes x-dir	Nodes y-dir	Total Nodes
1 (Fine)	99	800	79200
2 (Medium)	83	667	55361
3 (Coarse)	69	556	38364

Finally, the mass transfer is also assessed. The UDF describing the mass transfer process is implemented in the simulations. Three 2D grids are used with the specifications shown in the table 4.9. The inlet velocity is set at 0.27 m/s.

Pure CO_2 is considered as the gas phase whereas the liquid phase is a 30% wt. aqueous MEA solution. An unphysically high value of the mass source term, i.e. 92 $kg/m^3/s$ is implemented to check whether the mass source terms cause any numerical instability. Table 4.10 shows the values obtained for the three different meshes whereas Figure 4.8 shows the values of the mass fraction obtained as a function of the grid spacing. The mass fraction of the dissolved species also presents an oscillatory behaviour.

Although Richardson extrapolation is not applicable when an oscillatory behaviour appears, it is still possible to calculate the uncertainty of those variables. Ali et al [184] define the convergence ratio as presented in the following expression (4.9):

Table 4.10: Mass fraction as a function of the grid spacing. The grid point considered is placed at 5 cm from the liquid inlet and 0.34 mm from the surface of the plate.

Grid spacing (μm)	Mass fraction (-)
10.3	0.002497
8.5	0.002484
7.1	0.002571

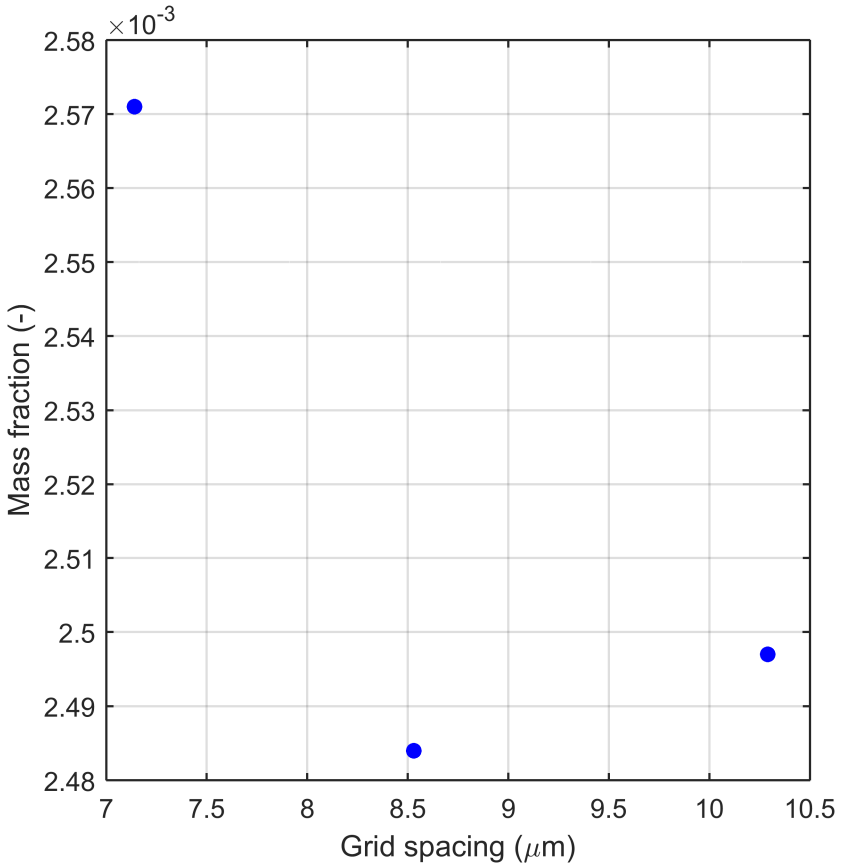

Figure 4.8: Mass fraction vs. grid spacing.

$$R = \frac{\varepsilon_{21}}{\varepsilon_{32}}, \tag{4.9}$$

where $\varepsilon_{21} = f_2 - f_1$ and $\varepsilon_{32} = f_3 - f_2$, being f_1 the value of the function of the fine mesh, f_2 that of the medium mesh, and f_3 the value associated to the coarse mesh.

Three different possible outcomes can be obtained from the application of equation (4.9):

- Monotonic convergence, if $0 < R < 1$,
- Oscillatory convergence, if $R < 0$
- Divergence, if $R > 1$

The application of the equation (4.9) to the variables included in this study gives the results shown in table 4.11.

Table 4.11: Values of the convergence ratio R for the different variables included in this study, considering the meshes C, D, and E. Case 1. The value corresponding to the liquid film thickness is not included since the application of the equation (4.9) results in a division by zero.

Variable	Convergence ratio R
Velocity	0.17
Pressure	-0.78
Interfacial area	0.59
Mass fraction	-6.69

For those variables that present oscillatory convergence, it is still possible to assess the numerical uncertainty, according to the expression

$$U = \frac{1}{2}\left(f_{upper} - f_{lower}\right). \tag{4.10}$$

Table 4.12: Values of the numerical uncertainty for the pressure and the mass fraction of the dissolved species.

Variable	Uncertainty Case 1	Uncertainty Case 2
Pressure (Pa)	0.2521000	0.6057415
Interfacial area (cm^2)	0.8944000	0.2033000

The equation (4.10) says that the numerical uncertainty of the variable f corresponds to half the amplitude of the oscillation observed. Applying the equation (4.10) results in the following values of the numerical uncertainty for the pressure and the interfacial area (table 4.12). The uncertainty for the mass fraction tested is 0.0000435.

As a conclusion, the results presented in this section present the oscillatory convergence behaviour pointed out by Ali et al [184]. To be more specific, there is a convergence for the first three refinement steps in most of the cases, which suggests that the optimum grid is accomplished [209]. The values begin to oscillate when further refinement is applied. The uncertainty has been calculated and presents a low value. The meshes used to obtain the results in this thesis are always in the range considered in this grid convergence study.

4.2 Validation

The term validation involves the definition of the error tolerance depending on the application of the model [185]. Generally, a high level of accuracy is required for a purely scientific work whereas in industry it should be simply enough for the purpose at hand. Therefore, CFD simulations might be used at different levels of increasing accuracy, according to Benek et al [186]:

- *Provide diagnostic information*

  The basic physics should be reasonably represented in this level. However, the accuracy is only qualitative.

- *Supply incremental data*

  At this level, quantative accuracy is required but only for increments.

- *Generate baseline data for the performance model data base*

  This level requires quantitative accuracy in absolute terms.

Sindir et al [187] point out four different phases for the validation of a code. The authors point out that a decreasing availability and accuracy of experimental data is found as the simulations and experiments increase in complexity.

- Phase 1: *Unit problems*

  This phase features validation of single flow features

- Phase 2: *Benchmark cases*

  This phase is characterised by validation of simple to moderate flow physics. More than one flow features are included at this level.

- Phase 3: *Simplified/partial flow path*

  Validation of multiple relevant flow features and moderate to complex flow physics.

- Phase 4 *Actual hardware*

  This phase presents validation of the complete flow physics.

Data availability and accuracy decreases as ones progresses from Phase 1 to Phase 4. As a matter of fact, a very limited amount of data is available in the literature to carry out the validation of the present model. The interfacial area of the gravity-driven liquid film is compared against some reported experiments. Also, some data on the mass transfer are used to compare the results. Therefore, the validation assessment presented in this section lies within Phase 2.

The methodology presented by Coleman and Stern [188] is used herein to assess the validation of the present model. The authors define the comparison error C as the difference between the experimental and the simulation data. It can be written as

$$C = D - S. \tag{4.11}$$

The comparison error C is usually used in the literature to establish whether or not a model is validated. If $\left|C\right|$ is small enough for a particular application then it is said that the model is validated.

If the assumption of independence of error sources is taken then it can be said that the true value lies in the interval $D \pm U$ 95%. The uncertainties of the comparison error U_E, the experimental U_D and the simulation values U_S is related by

$$U_E^2 = U_D^2 + U_S^2. \tag{4.12}$$

At the same time, the simulation uncertainty U_S^2 can be decomposed as the sum of three contributions [188]: the simulation numerical solution uncertainty U_{SN}, the simulation modelling uncertainty from using previous experimental data U_{SPD}, and the simulation uncertainty from modelling assumptions U_{SMA}

$$U_S^2 = U_{SN}^2 + U_{SPD}^2 + U_{SMA}^2. \tag{4.13}$$

The uncertainty due to the use of previous experimental data U_{SPD} can be considered negligible whereas the uncertainty due to modelling assumptions U_{SMA} cannot be easily estimated. The validation uncertainty U_V is defined as the combination of the experimental error U_D and the numerical solution uncertainty U_{SN}

$$U_V^2 = U_D^2 + U_{SN}^2. \tag{4.14}$$

Finally, if the comparison error C is less or equal to the validation uncertainty U_V then it can be concluded that the validation has been achieved at the U_V level. The value of the

validation uncertainty is corrected by a tolerance TOL_V as defined in the expression

$$\left|C\right| \leq U_V + TOL_V. \tag{4.15}$$

The first variable to be validated is the interfacial area. The experimental data from Hoffmann et al are used [189, 190] and the CFD results from Iso et al [191]. Figure 4.9 shows the comparison between the benchmark data and the present simulations. The interfacial area is presented as the percentage of the plate surface covered by the liquid.

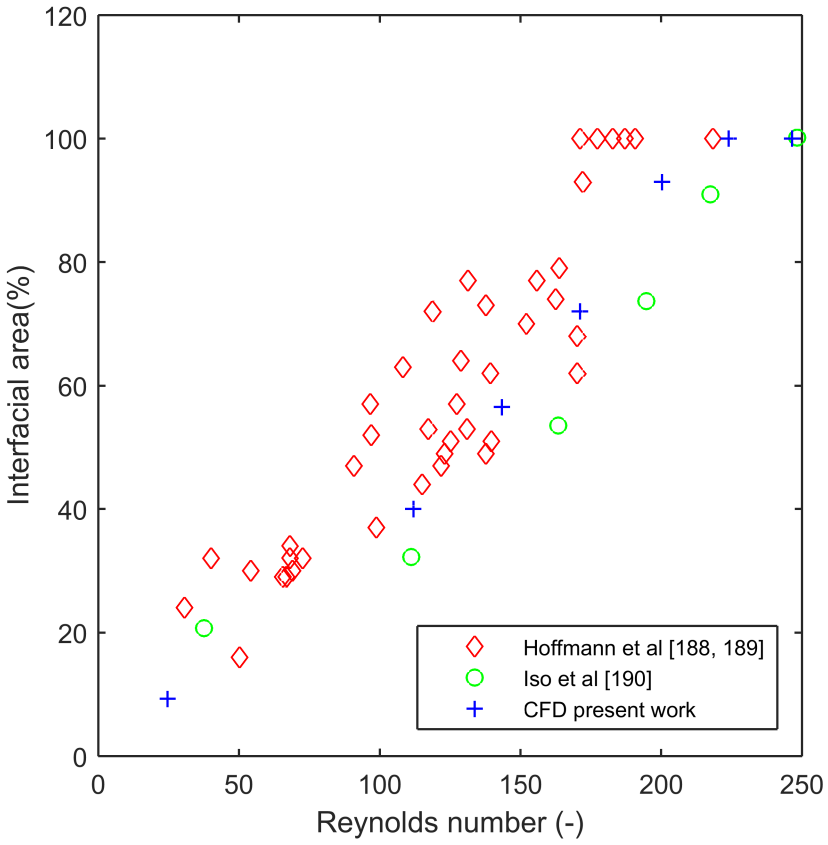

Figure 4.9: Interfacial area vs. Reynolds No. The gas phase in these simulations is air whereas the liquid phase is pure water. The Reynolds number is calculated as $Re = \frac{\rho_l v \delta_l}{\mu_l}$, being v the velocity at the liquid inlet and δ_l the liquid film thickness calculated according to Nusselt theory [178].

Table 4.13: Calculation of the comparison error for the interfacial area (%) between the CFD simulations in this work and the benchmark data from Hoffmann et al [189, 190].

Reynolds No.	Experimental	Simulation	Comparison error C
112.04	53.50 ± 19.0	44.0	9.5
137.72	58.75 ± 19.2	57.0	1.75
170.24	80.75 ± 32.2	68.0	12.75

Table 4.14: Calculation of the uncertainties and evaluation of condition (4.14)

Reynolds No.	U_D^2	U_V	C	Meets cond 4.14?
112.04	361.00	19.0	9.5	Yes
137.72	368.64	19.2	1.75	Yes
170.24	1036.84	32.2	12.75	Yes

As can be seen in the figure, the authors do not provide any information about the variability in their results. However, it is possible to obtain an average value and the standard deviation 2σ using the data in figure 4.9 for the three values of the Reynolds number shown. The results are included in table 4.13, which also calculates the comparison error by means of equation (4.11). Finally, the result of applying the validation condition, i.e. equation (4.15), is assessed in table 4.14. The numerical uncertainty U_{SN}^2 is taken as the value shown in table 4.12 for case 1, i.e. 0.8944 cm^2. As a result, the condition (4.15) is met for the three cases considered, which was foreseeable since the values obtained with the present CFD simulations lie within the experimental work from Hoffmann et al, i.e. figure 4.9.

Data available in the literature on mass transfer are scarce. Some experimental results were presented by Xu et al [172], who performed mass transfer experiments for the propane-toluene system in an inclined plate. The results of the present simulations are compared with their experiments and simulations in figure 4.10. The benchmark does not include any data on variability. However, the present model clearly underestimates the values obtained by Xu et al [172]. A similar underestimative behaviour is also presented

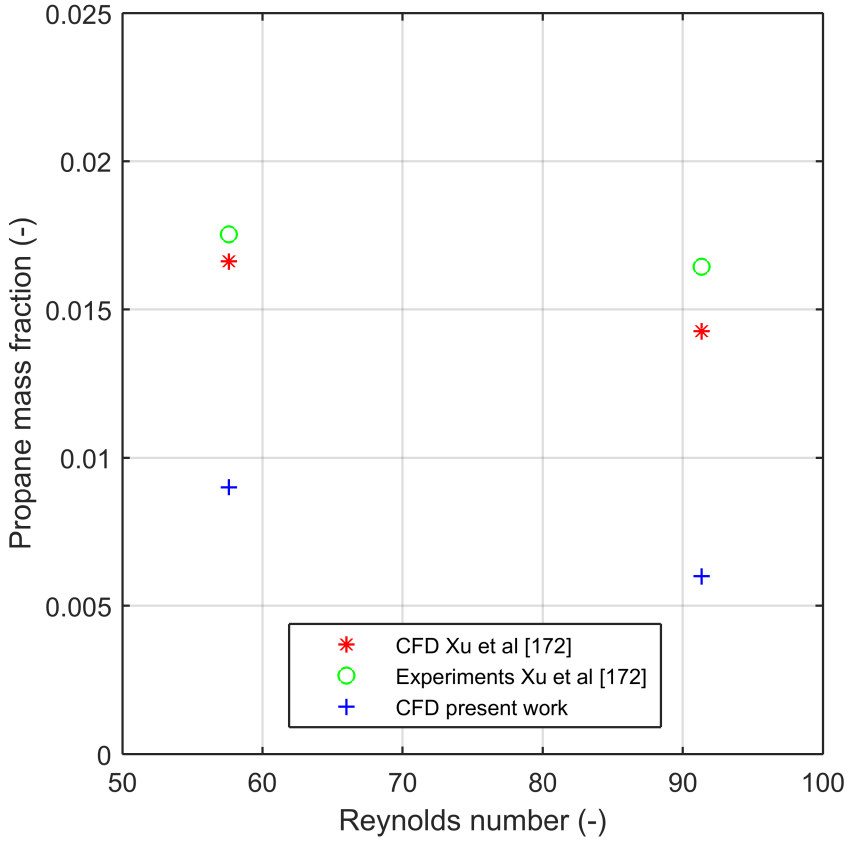

Figure 4.10: Comparison between the results obtained with the present model and the benchmark data from Xu et al [172] for the propane concentration at outlet conditions.

by Yu et al [173]. It can also be observed that the tendency is well represented and the propane mass fraction decreases with the Reynolds number by virtue of the decrease in contact time between both phases. Figure 4.11 shows the comparison between the Sherwood number obtained with the present model and experimental correlations found in the literature [90, 192, 193]. It is shown in the figure that the results from the present simulations follow the same tendency and the same order of magnitude than the cited correlations.

As a conclusion, the effective area as a function of the Reynolds number at the liquid inlet is validated and can be used to *"generate baseline data for the performance model*

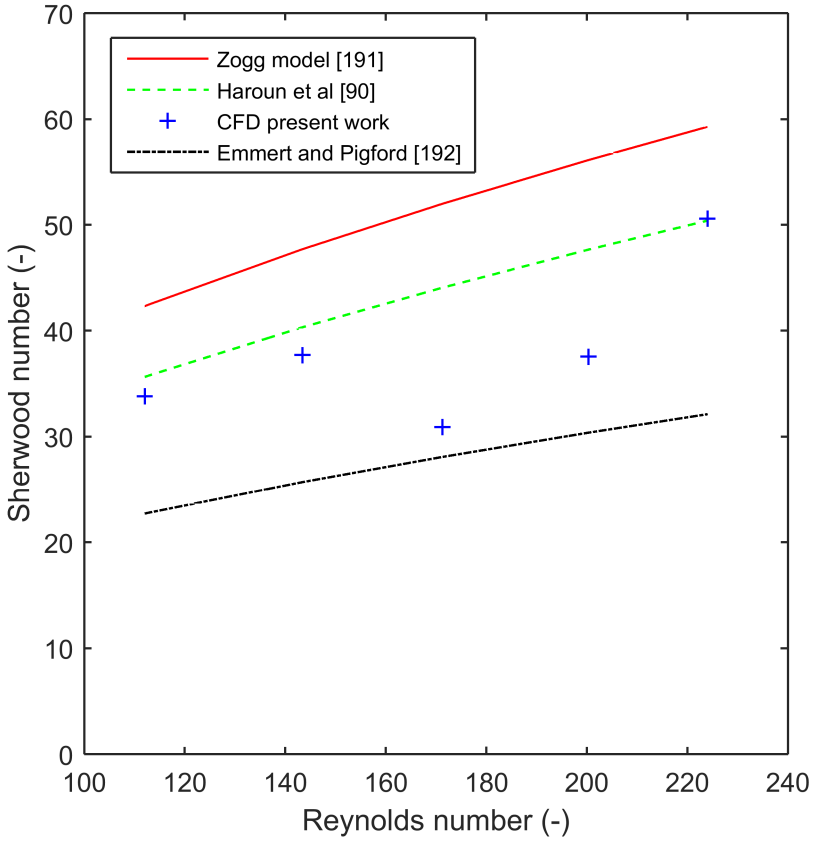

Figure 4.11: Comparison between the results obtained with the present model and experimental correlations found in the literature for the oxygen/water system.

data base" according to Benek et al [186]. Regarding mass transfer, complete validation of the model has not been accomplished. However, the tendencies of the variation on the mass transfer rate against the Reynolds number has been compared to CFD and experimental results. Furthermore, the values of the Sherwood number against the Reynolds number obtained with these simulations lie well within the values provided by experimental correlations found in the literature [90, 192, 193]. The model can thus be further used to *"provide diagnostic information"*.

Chapter 5

Hydrodynamics and mass transfer: Small-scale

This chapter presents the first step in the development of the model at small-scale. The first aspect to be analysed is the hydrodynamics of the liquid film over the structured packing. The simulations are run in 3D computational domains instead of 2D. This constitutes one of the novelties of the present work and helps visualising the formation of droplets and rivulets in the packing walls, i.e. contrarily to the often assumed perfectly developed liquid film.

The study of the hydrodynamics has been started in section 4.2, where the relationship between the liquid load and the interfacial area has been compared to experimental data available in the literature. The relationship between the liquid load and the effective area results in three different flow regimes, i.e. trickling, rivulet and full film flow. After the analysis of the hydrodynamics for the case of a smooth metallic plate, the influence of a certain surface texture, i.e. a triangular geometric pattern, is considered. The objective of this test is to check whether or not a particular geometrical pattern on the packing surface is able to modify the wetting process, hence the mass transfer performance of the packing.

The study also includes the influence of the liquid viscosity on the wetted area, showing the beneficial impact of increasing the MEA percentage for the range of liquid loads considered.

Finally, the chapter ends with the implementation of the mass transfer theory – without chemical reaction – on a UDF. The mass transfer is analysed for the case of oxygen absorption into pure water. Once the absorption theory is implemented in the UDF, the influence of the liquid load on the mass absorption rate is tested, showing the existence of an optimum point that depends on the amount of wetted area.

5.1 Effect of the liquid load on the wetted area

The analysis of the variation of the wetted area with the liquid load gives rise to three different flow regimes, i.e. trickling, rivulet and full film flow, which have been reported in the literature and are reproduced in figure 5.1. The image on the left-hand side represents the trickling flow and is characterised by the formation of two stable rivulets on both sides of the domain and a central part that remains unstable, with droplets being detached as the liquid accumulates and gravity overcomes the cohesion of the liquid. In this regime, surface tension prevails over gravity. The central image represents the rivulet flow, which is found as the liquid load increases. The rivulet flow is characterised by the two rivulets formed in the previous regime plus the formation of a third one at the centre of the domain. The rivulets are joined by a front wave that delimits an area where a perfectly developed liquid film is observed. In this case, cohesion due to surface tension still dominates, hence the appearance of the central rivulet. The extension of the area where the liquid film is formed increases with the liquid load, augmenting to the extent that the full film flow appears when a particular value of the liquid load is reached, i.e. the full film flow in the image at the right-hand side of the figure. The full film flow regime is identified by the

formation of a liquid film that covers the entire plate. It is important to remark that the full film flow is an ideal case and it is never encountered in a structured packing. On the other hand, a combination of trickling and rivulet regimes appears as is analysed in Chapter 8.

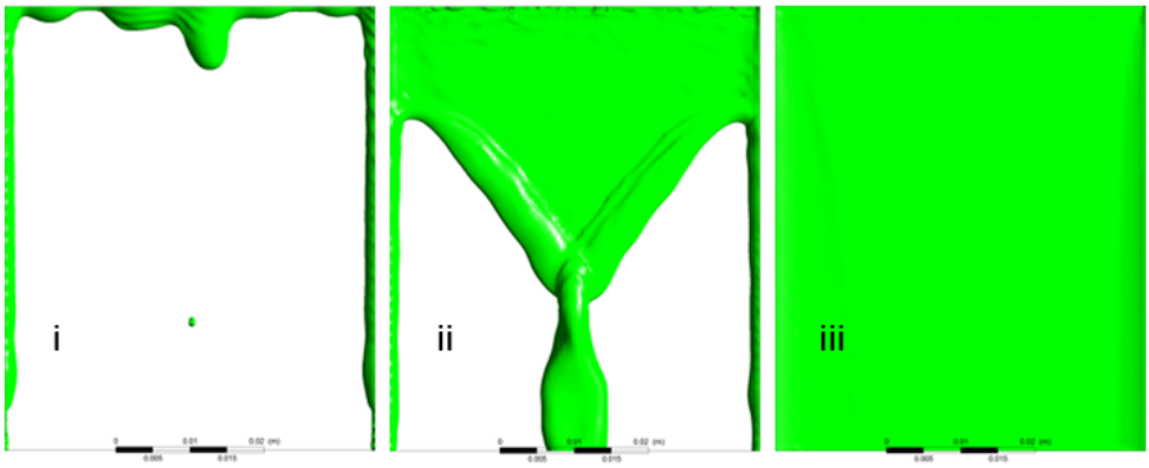

Figure 5.1: Liquid film patterns at different liquid loads at pseudo-steady state. Pure water and air. The computational domain is a 0.05 m x 0.007 m x 0.06 m smooth plate inclined 60° over the horizontal: i) Trickling flow, We=0.016, 5.5 cm/s; ii) Rivulet flow, We=0.561, 32 cm/s; and iii) Full film flow, We=1.369, 50 cm/s.

The formation of the three different flow regimes respond to the balance between the cohesion of the liquid, represented by the surface tension; and the forces that tend to spread the liquid (gravity). The balance between both types of forces is represented by the Weber number, which is calculated as

$$We = \frac{\rho_l v_l^2 \delta_l}{\sigma}. \tag{5.1}$$

The Weber number constitutes an alternative manner to represent the liquid load since the rest of the parameters have not been modified. Higher values of the Weber number imply that gravity prevails over surface tension whereas the opposite happens when its value decreases. The trickling flow has been observed for values of the Weber number

of up to 0.4, at which the instability in the central part gives way to the formation of the central rivulet, hence entering the range of values of the rivulet regime. The rivulet flow lasts for values up to 1.2. In the latter, the surface tension still prevails over gravity, leading to the formation of round structures. Beyond this point, gravity becomes dominant and the full film flow develops.

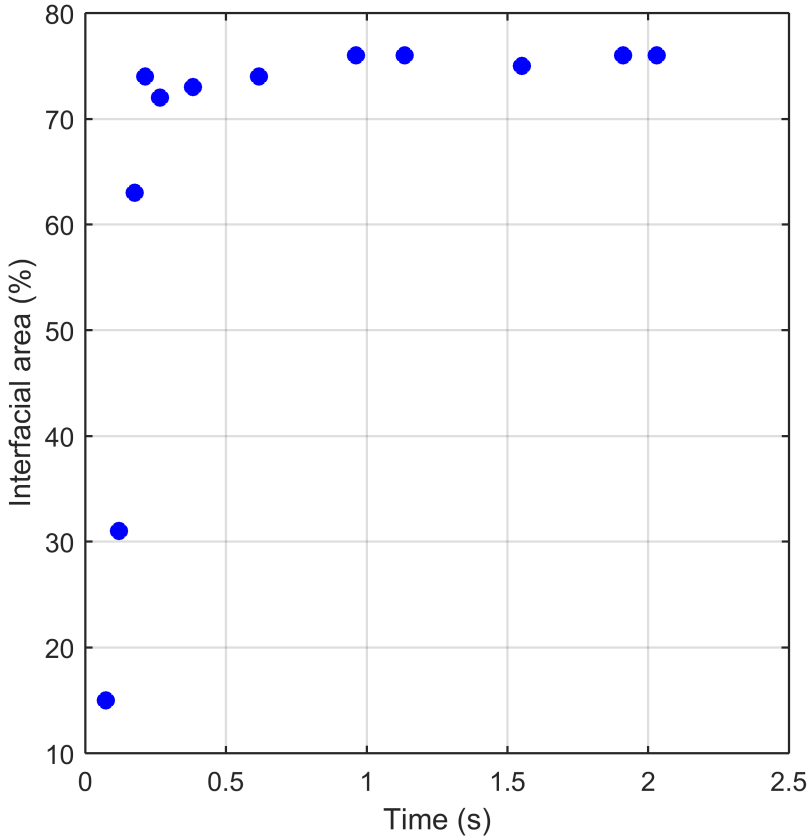

Figure 5.2: Transient evolution of the wetted area in the smooth plate. Pure water and air. The liquid inlet velocity is 38 cm/s. 60° inclination over the horizontal.

As a conclusion, the interface tracking at small-scale is able to reproduce the effect of the balance between the gravity and the cohesion of the liquid, reproducing the flow regimes observed in the experiments found in the literature. The relationship between the wetted area and the liquid injection velocity is therefore well represented.

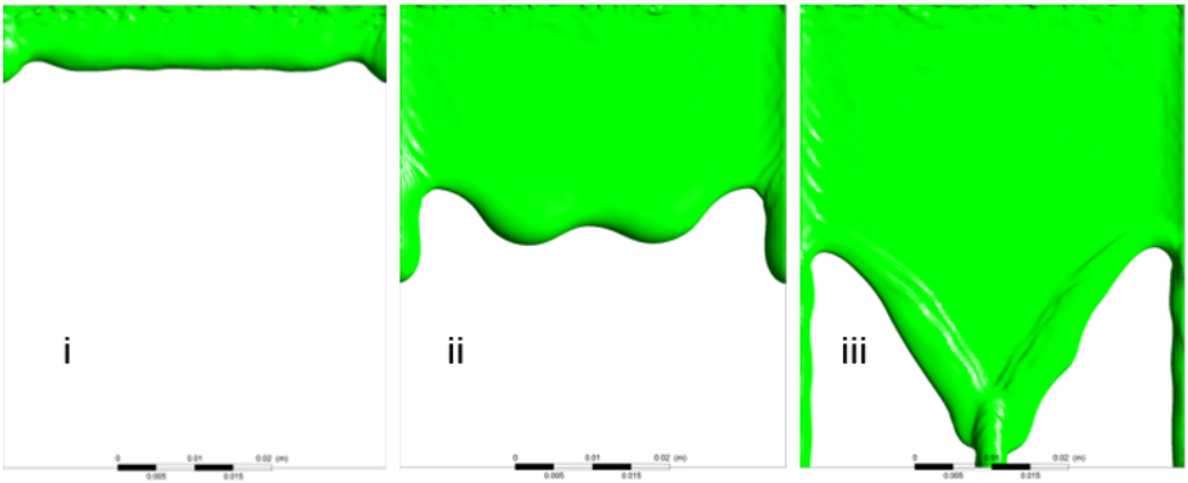

Figure 5.3: Liquid film patterns at different flow times. Pure water and air. The liquid inlet velocity is 38 cm/s. The computational domain is a 0.05 m x 0.007 m x 0.06 m smooth plate inclined 60° over the horizontal direction. The contact angle is 70°. Flow times: i) 0.058 s, ii) 0.133 s, and iii) 0.261 s.

The transient evolution of the wetted area is presented in figure 5.2. The fluids used are water and air. The liquid injection velocity, i.e. or liquid load, is 38 cm/s (Re $\simeq$ 170, We $= 0.8$). Pseudo-steady state is reached after an approximate flow time of 0.5 s. The pseudo-steady state is recognised by the appearance of small variations in the value of the interfacial area. The variation shows a direct relationship during the first time steps followed by a peak value when the front wave reaches its final extension. After that, the wetted area presents a small drop and gets stabilized at a constant value. Figure 5.3 shows the flow patterns at different flow times for the same case as in figure 5.2, which corresponds to a rivulet flow regime. The formation of the lateral rivulets due to the capillary effects at the corners of the plate begins at an early stage of the development. The area with the perfectly formed liquid film can also be observed.

The following step is to investigate how to increase the amount of wetted area. Two of the parameters that influence the spreading of the liquid are the liquid viscosity and the

use of a particular geometrical pattern on the surface texture.

5.2 Effect of wall surface texture on the wetted area

The objective of this section is to discuss whether or not the fact of using a particular texture in the surface of the plate can increase the amount of wetted area.

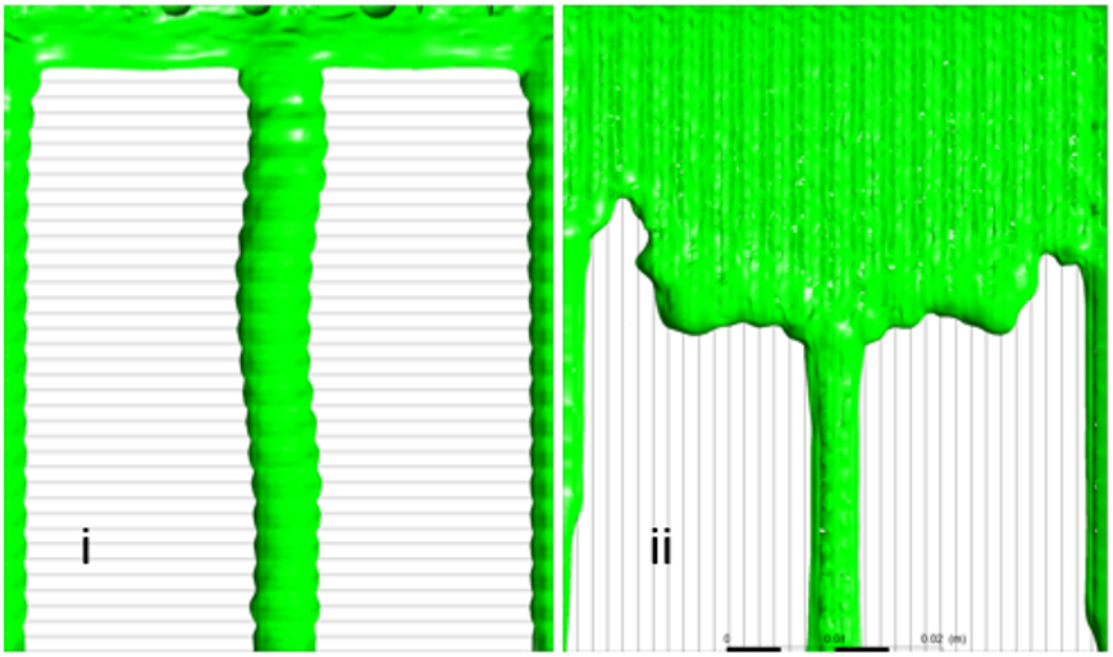

Figure 5.4: Prediction of the flow regime for the two surface textures tested. Pure water and air. The liquid inlet velocity is 22 cm/s. 0.05 m x 0.007 m x 0.06 m smooth plate inclined 60° over the horizontal direction. The contact angle is 70°. The flow time is 0.350 s: i) Ridges placed perpendicularly to the direction of the flow, and ii) Ridges placed according to the direction of the flow, i.e. stream-wise.

A simple texture pattern, which can be easily implemented in CFD, is the inclusion of ridges with a simple shape. In this case, a triangular shape is tested, the base and height of the triangle being respectively 2.8 mm and 0.6 mm. The ridges are placed with two different orientations: stream-wise and perpendicular to the main direction of the flow.

The stream-wise pattern is expected to increase the wetted area, since it splits the central rivulet, directing the flow along the ridges.

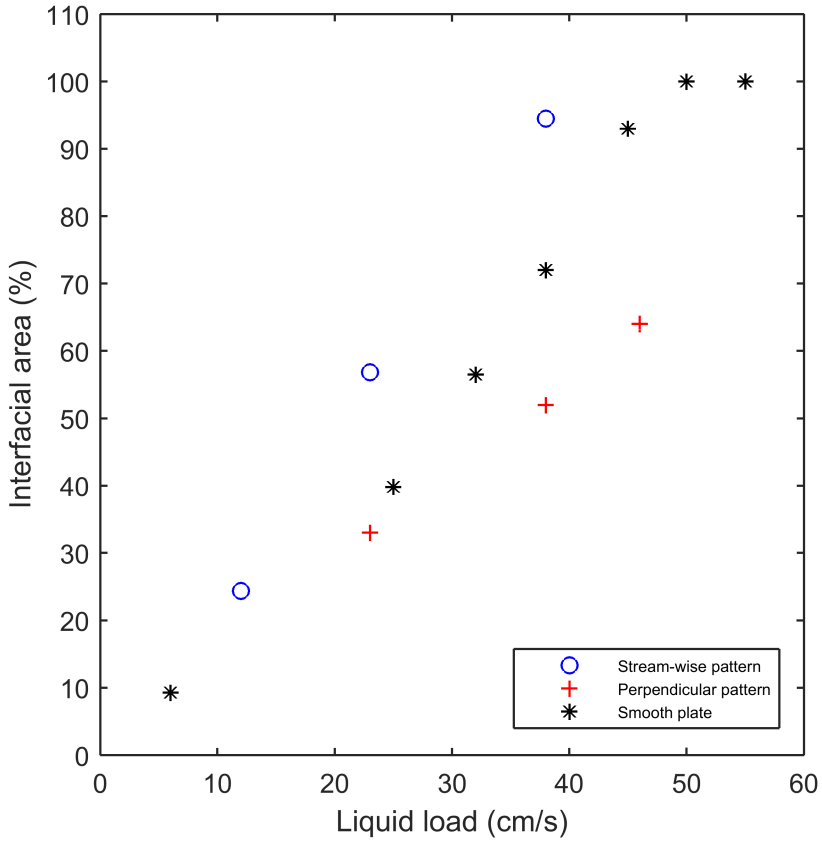

Figure 5.5: Effect of the surface pattern on the wetted area (% of interfacial area) at different liquid loads and pseudo-steady state. 0.05 m x 0.007 m x 0.06 m plate inclined 60° over the horizontal direction. The contact angle is 70°.

Figure 5.4 shows a view of the liquid flow pattern for the same liquid injection velocity and the two surface textures considered. The snapshots have been taken at 0.35 s flow time. As can be observed, the expected behaviour is confirmed and the ridges direct the liquid flow when placed in the stream-wise direction. Contrarily, the ridges act as a barrier when placed in the perpendicular direction, enhancing the effect of the surface tension and showing a smaller value of the wetted area. The general conclusion then is that adding a

texture pattern to the packing surface clearly affects the amount of wetted area available for mass transfer.

Figure 5.5 quantifies the effect of the liquid load in the wetted area for the two texture arrangements and the case of the smooth plate. One can see that the results for the smooth plate are situated between the two texture pattern data series. One can also observe that the difference between them is greater as the value of the liquid load increases.

The analysis of the data above highlights the importance of selecting a particular geometrical texture pattern and its disposition with respect to the general direction of the flow. The results show that the shape of the ridges should direct the liquid flow in order to enhance the amount of interfacial area available for mass transfer. Further work should be done in this direction to check whether the size of the triangular shape can also influence the amount of wetted area.

5.3 Effect of the liquid viscosity on the wetted area

The large difference in viscosity between water, i.e. 1 mPa · s, and MEA, i.e. 24 mPa · s, is expected to give rise to significant changes on the wetted area when comparing pure water and different concentration solutions of aqueous MEA at the same liquid load. Figure 5.6 shows the relationship between the wetted area and the liquid load for three different values of the liquid viscosity, corresponding to the case of pure water and two aqueous solutions used in industry, e.g. 30% wt. MEA and 40% wt. MEA. In this case, a higher viscosity results in a better spreading of the liquid with a substantial difference at low liquid loads. For a liquid load of 22 cm/s, the full liquid film is reached when the 40% wt. solution is used and almost achieved by the 30% wt. solution whereas the area covered by pure water covers 60% of the plate surface.

At 12 cm/s, the difference between the three points is considerable, clearly showing

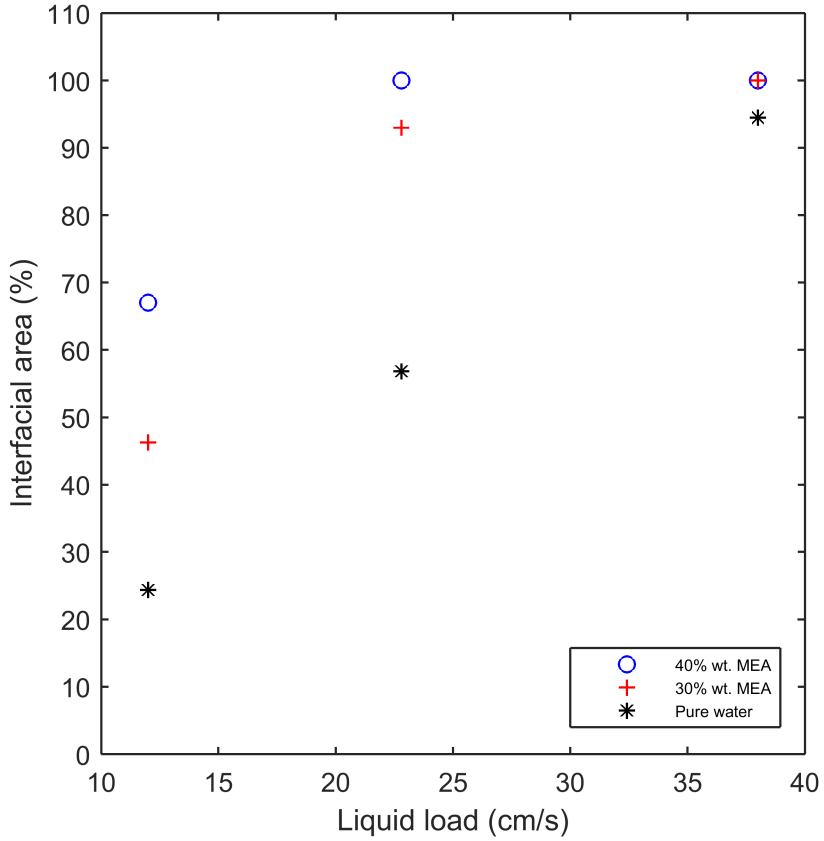

Figure 5.6: Effect of viscosity on the wetted area (% of interfacial area) at different liquid loads and pseudo-steady state. Comparison between pure water and two MEA aqueous solutions, i.e. 30% wt and 40% wt. 0.05 m x 0.007 m x 0.06 m plate inclined 60° over the horizontal direction. Triangular ridges placed in the stream-wise direction, i.e. the height of the triangle is 2.8 mm and the base is 0.6 mm. The contact angle is 70°.

that the increment in the viscosity causes a better liquid spreading. At high liquid loads, pure water approaches the full film flow while the other liquids have already achieved it. The transient development of the three cases at 38 cm/s is analysed later in Chapter 7 where it is observed that higher wetted area values are achieved as the viscosity increases despite the fact that the development of the liquid film is slower.

The results found in the literature, regarding the effect of the viscosity on the wetted area, are often contradictory [194]. Therefore, some inconsistency exists in the literature

on whether an increase in the liquid viscosity results in a better spreading or vice versa. The results obtained in this section are consistent with the work presented by Shi and Mersman [195]. However, it is important to recall that the present results refer to the case of an inclined plate. As it will be explained in Chapter 8, the results show the opposite tendency at meso-scale, although with a negligible difference between the cases.

5.4 Transient behaviour of the mass transfer

After the analysis of the parameters that affect the interfacial area, the mass transfer theory shown in Chapter 3 was introduced in the model by means of a UDF. The figure 5.7 shows the transient evolution of the averaged oxygen mass fraction in the gas-liquid interface for four values of the liquid load. The figure shows three stages for each case. In the first stage, the oxygen mass fraction in the liquid film is practically identical regardless of the value of the liquid load. This behaviour responds to the fact that at the early stage of the formation of the film, an accumulation of liquid is generated at the inlet region due to the effect of surface tension. As a consequence, the exposure time is the same for all the cases, leading to similar values of the mass fraction of oxygen absorbed in the liquid. This stage lasts until approximately 0.05 s flow time.

The second stage lasts until approximately 0.25 s flow time and is characterised by a lower absorption rate, i.e. represented by the slope of the graph. The transition between the first and the second stages is clearly delimited by a slope change. In the second stage, the values of the oxygen absortion rate at the different liquid loads are similar until approximately 0.1 s flow time. The beginning of the second stage has been considered to happen when the absorption rate presents a clear diminution with respect to that of the first stage. This decay of the absorption rate is due to the fact that, as the absorption progresses, the difference in the solute concentration between the interface and the bulk

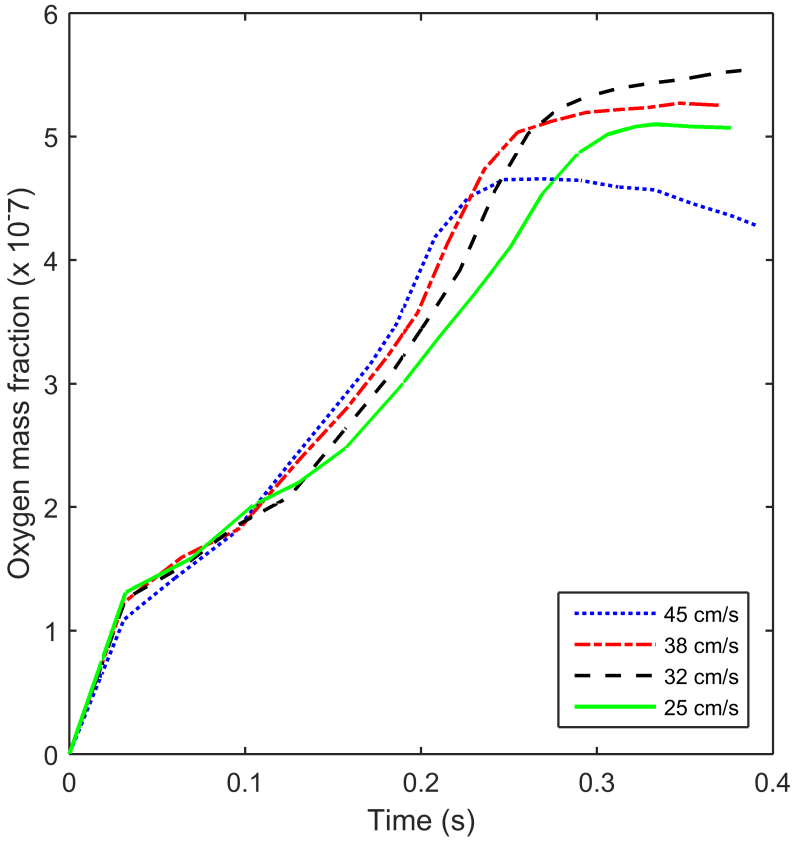

Figure 5.7: Transient evolution of the oxygen mass fraction in the liquid film for four different values of the liquid load. 5 cm x 7 mm x 6 cm smooth plate inclined 60° over the horizontal direction. The contact angle is 70°. The value of the solubility for the oxygen into pure water is 8 mg/l at 20°C.

of the phase becomes smaller, leading to a decrease in the mass transfer rate.

Also, the concentration values observed in the graph begin to present different values in this stage since the transient behaviour of the wetted area also begins to differ, which consequently affect the exposure time.

Finally, the stabilisation of the oxygen mass fraction occurs when the system reaches the hydrodynamical pseudo-steady state, i.e. when the wetted area reaches a constant value. As a final remark, one can also observe that the greater the liquid flow rate, the later the stabilisation is achieved. This behaviour was expected since a smaller liquid

injection rate necessarily leads to a slower development of the liquid film.

5.5 Effect of the liquid load on the absorption rate

The effect of the liquid load on the oxygen absorption rate is depicted in figure 5.8. The absolute rate of oxygen absorbed in pure water in the inclined plate is calculated as the product between the average mass fraction of oxygen in the liquid phase in the liquid outlet times the mass flow rate of liquid injected into the domain.

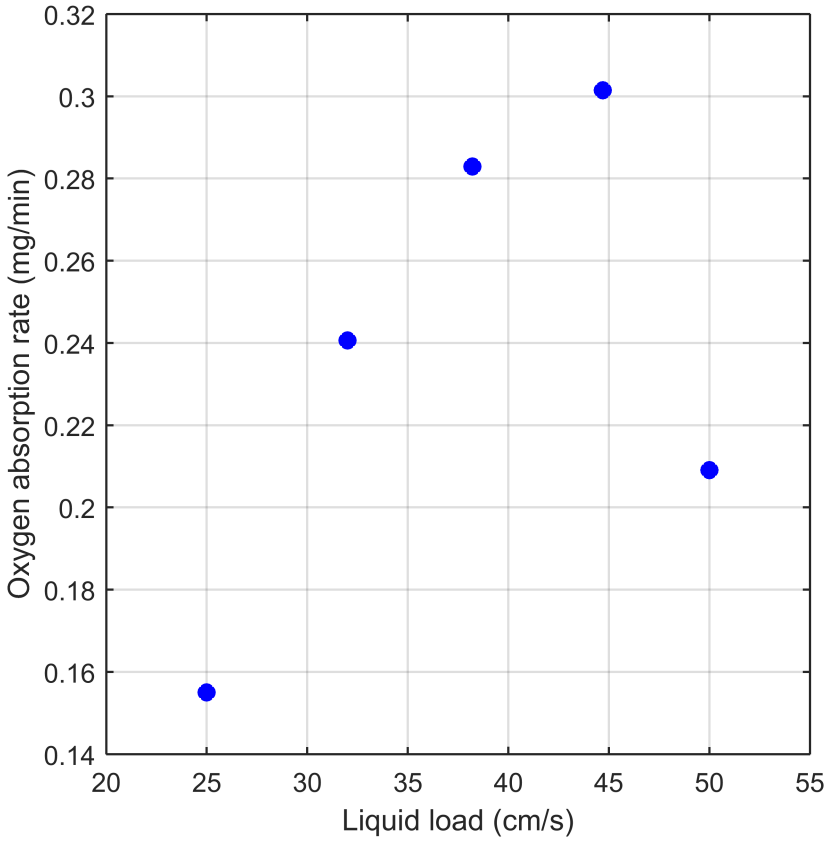

Figure 5.8: Oxygen absorption rate vs liquid load at pseudo-steady state. 5 cm x 7 mm x 6 cm plate inclined 60° over the horizontal direction. The contact angle is 70°.

The graph shows a direct relationship between the two variables until a maximum

point is reached beyond which the absorption rate decreases. According to Higbie's penetration theory, higher liquid loads imply less exposure time between the phases hence a decreasing tendency could be expected. However, before the turning point observed in the graph the tendency is exactly the opposite due to the existence of a greater amount of interfacial area available for mass transfer, which enhances the oxygen absorption rate. Once the turning point is surpassed, the trend follows the theoretical reasoning from Higbie's theory. The turning point appears at a value of the liquid load of approximately 45 cm/s, which coincides with the value of the liquid load in which the full film flow is reached. Therefore, beyond the turning point the interfacial area does not augment whereas less contact time between the phases occurs, which results in a decay of the absorption rate.

5.6 Conclusions

The present chapter presents the analysis of the hydrodynamics of the gravity-driven liquid film flow over an inclined metallic plate and the mass transfer between the gas and the liquid phases without chemical reaction. Regarding the hydrodynamics, special focus is put on the variations of the wetted area as a function of parameters such as the liquid load, liquid viscosity and the surface texture pattern. Later, the mass transfer performance for the water/oxygen system is included.

The main conclusion taken from the analysis of the hydrodynamics is that the amount of wetted area depends on the liquid injection velocity. An analysis of this relationship was done in terms of the balance between the gravity and the surface tension, i.e. the Weber number. Three different flow regimes can be identified in the analysis: tricking, rivulet and full film flow. The full film flow, i.e. the flow regime in which the whole surface of the plate is covered by the liquid phase, is reached only for values of the liquid load over a particular threshold. Before this value is reached, the flow shows the forma-

tion of irregular structures such as droplets and rivulets. This phenomenon is known as liquid maldistribution and its existence has been experimentally investigated in the literature. The importance of a good representation of this phenomenon lies in the effect that the amount of interfacial area available for mass transfer has on the overall performance of the reactor. As a consequence, a greater amount of interfacial area implies a better absorption performance. After the study about how the liquid load affects the wetted area, the influence of the texture pattern was also assessed. A triangular pattern forming ridges on the surface of the inclined plate is tested. The results show that the amount of wetted area is enhanced when the ridges are placed in the same direction as the liquid flow whereas the same ridges act as a barrier when placed perpendicularly.

Additionally, the viscosity of the liquid phase is assessed. The simulations included three different fluids: pure water and two aqueous MEA mixtures used in industry. The results show that increasing the viscosity of the fluid results in a better liquid spreading. However, it is worth to say that contradictory results have been found in the literature and that the effect of the viscosity on the wetted area is not well established.

After the study of the influence of the geometrical pattern, the mass transfer between oxygen and water is implemented on the model. The analysis of the transient behaviour of the system follows. Three different stages are found in the graph for the averaged oxygen mass fraction. The first stage is characterised by the coincidence between the different series of data. As the liquid film develops, a decrease in the absorption rate occurs until total stabilisation at pseudo-steady state conditions is reached.

Finally, the same model is applied to assess the relationship between the absorption rate and the liquid load. Since an increase in the wetted area is found for higher liquid loads, a direct relationship between the absorption rate and the liquid injection velocity is expected. The results show this tendency for the entire range of values of the trickling and the rivulet flow. However, once a completely developed liquid film is formed the tendency

reverses and a decreasing relationship is found between the two variables. This behaviour is caused by a smaller exposure time. Also, the existence of this turning point could be analysed for the case of the operation of a real absorption column.

Chapter 6

Effect of operating parameters on mass transfer

After the development of the mass transfer model without chemical reaction, this chapter analyses the influence of several operating parameters on the mass absorption rate. The following parameters are included in the study:

- The viscosity of the fluid. This parameter can be varied changing the concentration of the amine in the liquid solution. The viscosity hinders the diffusion process according to the Wilke-Chang equation hence a reduction in the absorption rate is expected for higher amine concentrations.
- The effect of the gas pressure: Higher values of the gas pressure imply a higher solubility of the species being transferred from the gas phase. The mass transfer rate is assessed for three different values of the gas pressure.
- Gas velocity: This parameter can also affect the mass transfer performance through the variations on the contact time between phases and its influence on the interfacial area.

- Flow configurations: The performance of the mass transfer process is analysed for both co- and counter-current flow. Normally, absorption columns operate at counter-current conditions since it is established that this configuration maximises the mass transfer performance. In this chapter both flow configurations are compared for the case of a small inclined plate.

- Liquid-solid contact angle: This parameter depends on the cohesion of the liquid molecules and the adhesion of the liquid to the solid surface. Better adhesion conditions imply a better spreading of the liquid over the plate, which results in more area available for mass transfer.

6.1 Effect of the viscosity on the mass transfer rate

The immediate effect of varying the amine concentration is a change in the overall viscosity of the solution due to the difference in the values associated to both water and MEA. Water has a value of the dynamic viscosity of 1 mPa·s whereas the value for pure MEA at the temperature considered, i.e. 295K, is 24 mPa·s. The assumption of a mass weighted mixing law has been taken to calculate the viscosity of the mixture. The viscosity of the solution can also vary with the amount of absorbate in the liquid phase. However, it is assumed that the properties of the liquid phase remain constant regardless of the solute concentration.

The viscosity can affect the mass transfer source term through both the solubility and the diffusivity of the solute. The influence on the solubility has been reported in the literature to be negligible [126], whereas the diffusivity can be calculated by means of the Wilke-Chang equation, i.e. equation (3.102). Figure 6.1 shows the effect of the amine concentration on the oxygen absorption rate at pseudo-steady state conditions. Two liquid

loads and two aqueous MEA solutions commonly found in industry, i.e. 30% and 40% wt. MEA, are used to carry out the simulations. The liquid injection velocities considered are 38 cm/s and 45 cm/s. Both values of the injection velocity correspond to the rivulet flow regime presented in Chapter 5. The velocities selected to carry out the analysis belong to this flow regime since it is the actual regime found in industrial operation. As a general trend, it is observed that the absorption rate decreases when the liquid viscosity increases. This was an expected result in the light of the Wilke-Chang equation since the value of the diffusivity has an inverse relationship with the viscosity of the liquid.

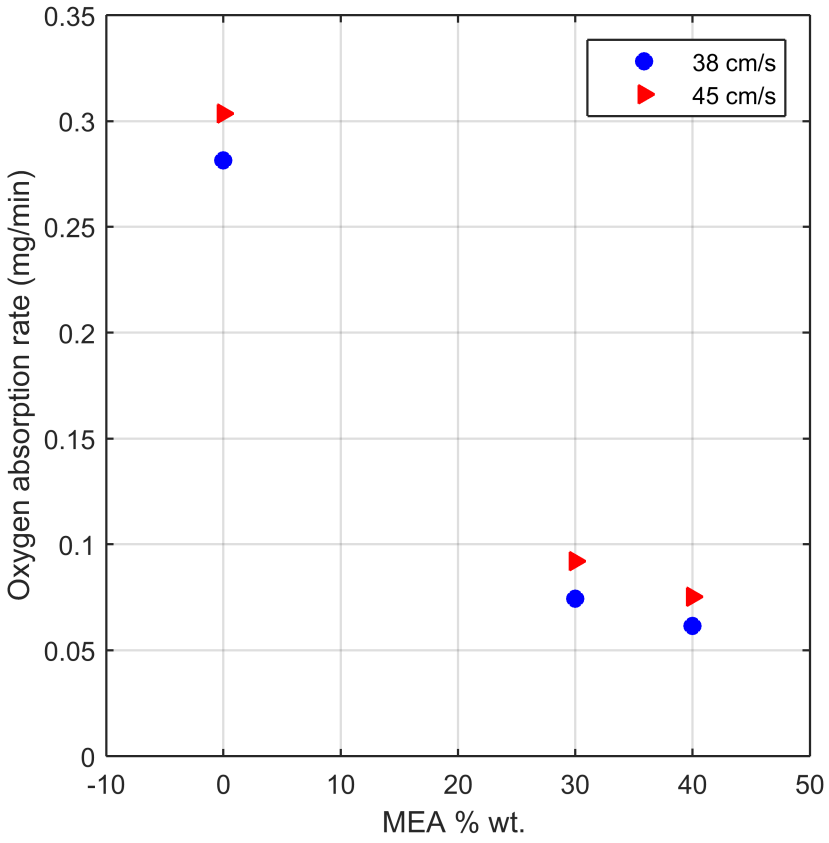

Figure 6.1: Oxygen absorption rate vs MEA wt. % for two different liquid injection velocities. 5 cm x 7 mm x 6 cm plate inclined 60° over the horizontal direction. The contact angle is 70°. Pure oxygen as stagnant gas phase.

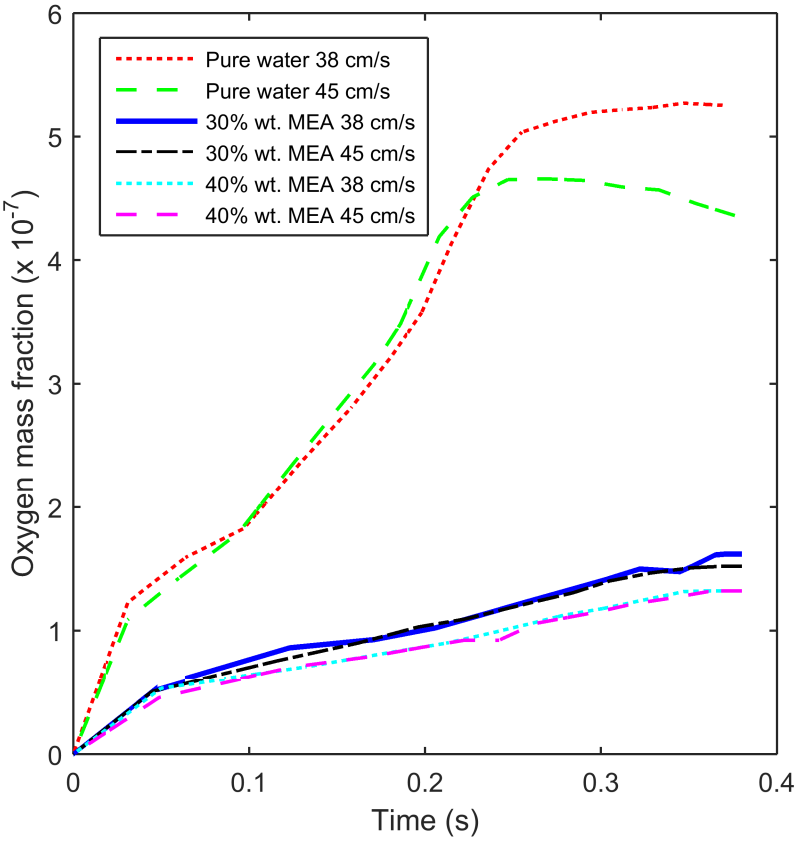

Figure 6.2: Oxygen mass fraction vs time. 5 cm x 7 mm x 6 cm plate inclined 60° over the horizontal direction. The contact angle is 70°. Pure oxygen as stagnant gas phase.

The effect of the liquid load can also be observed in figure 6.1. In general, the greater the velocity the greater the mass absorption rate since both values of the liquid load tested lie in the range of the rivulet flow. This is caused by the fact that the interfacial area, hence the mass transfer rate, increases with the liquid load for range of liquid loads in the rivulet flow as discussed in chapter 5.

Figure 6.2 shows the effect of the amine concentration on the transient behaviour of the absorption process for two different liquid injection velocities. The results show that the higher the amine concentration the smaller oxygen absorption in the liquid film.

The three stages discussed in Chapter 5 for the transient development can also be

observed in figure 6.2. As a general conclusion, it must be said that the viscosity of the liquid hinders the absorption process without chemical reaction.

6.2 Effect of the gas pressure

Figure 6.3 shows the transient evolution of the absorbed oxygen for the three values of the absolute gas pressure tested in this study. The three values tested are atmospheric pressure, 0.5 bar and 1 bar gauge pressure. The corresponding solubility values are summarised in table 6.1.

Table 6.1: Values of the solubility of pure oxygen in water as a function of the gas pressure

Gauge pressure (bar/Pa)	Solubility (x 10^{-6} $kg_{O_2}/kg_{solution}$)
0.0/101,325	8.5
0.5/151,987	13.5
1.0/202,650	17.0

The results show that a greater value of the gas pressure gives rise to a better absorption rate. An increment in 0.5 bar gauge pressure implies an improvement of up to 60%, taking the immediate inferior pressure value as the base case. The simulations are carried out with the same water injection velocity for the three cases, i.e. 38 cm/s, and pure oxygen as the stagnant gas phase.

Increasing the pressure of the gas phase implies a higher solubility of the gas species being transferred as described by Henry's law. With a greater value of the concentration at the gas-liquid interface, the concentration gradient is higher, which translates into a greater amount of gas being absorbed through the interface.

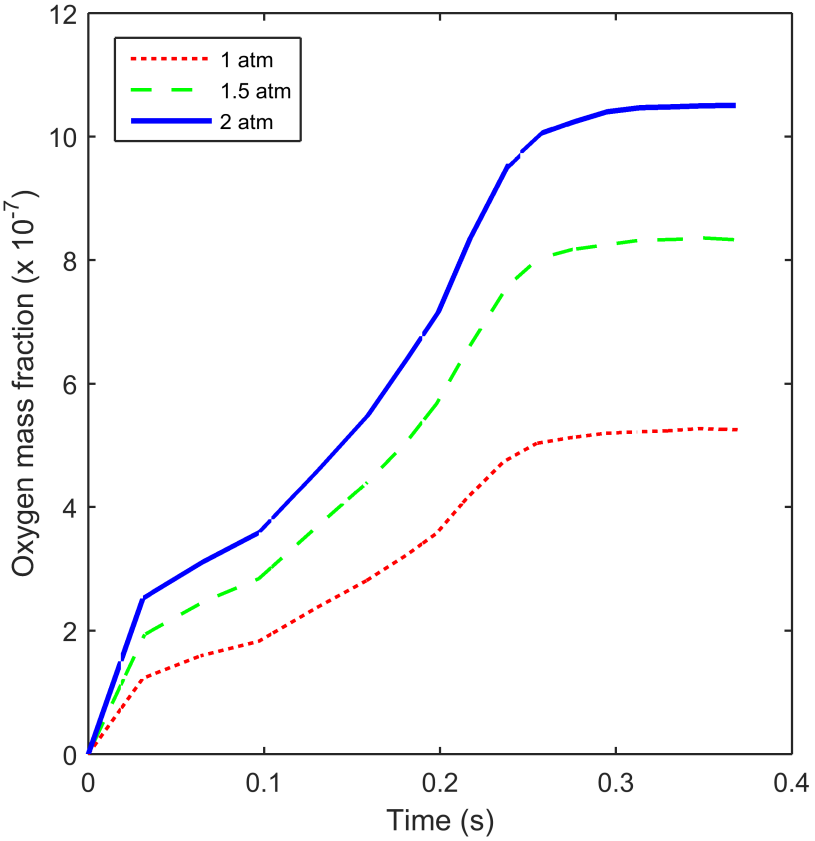

Figure 6.3: Oxygen mass fraction vs time. Comparison between the three absolute gas pressure values tested. 5 cm x 7 mm x 6 cm plate inclined 60° over the horizontal. The contact angle is 70°. Pure oxygen as stagnant gas phase. Pure water as the liquid phase with a liquid load of 38 cm/s.

6.3 Effect of flow configurations and gas velocity

Post-combustion CCS absorbers work usually in counter-current disposition. In this section the effect of using either co- or counter-current flow disposition is investigated for the simplified case of an inclined plate.

The effect of the gas velocity is also assessed. The gas velocity is represented by the F-factor:

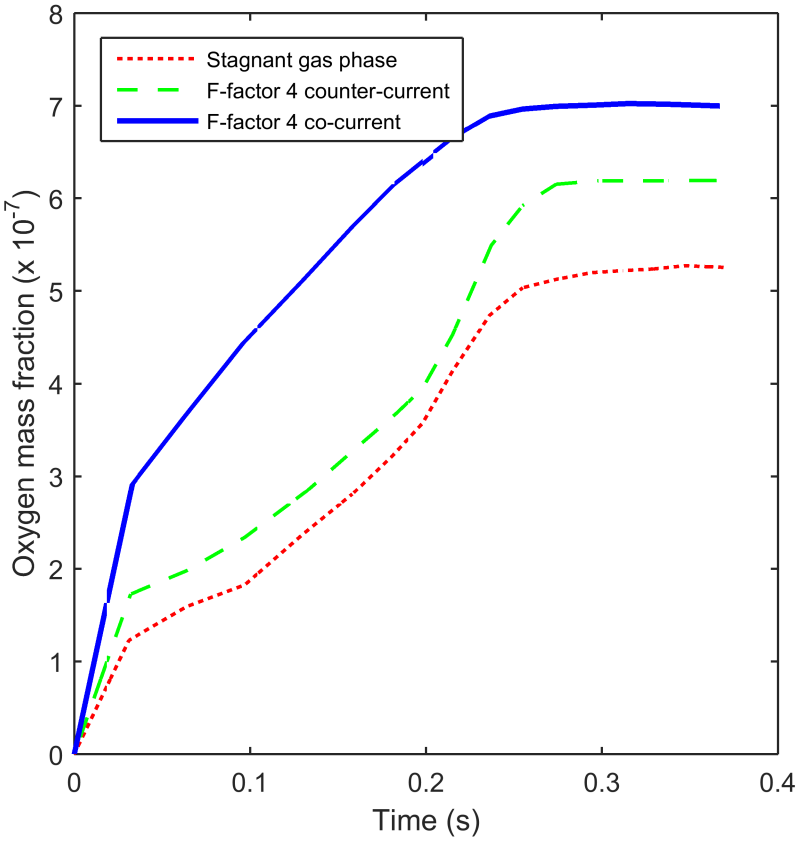

Figure 6.4: Oxygen mass fraction vs time. Comparison between both co- and counter-current flow configurations and the stagnant gas phase case. 5 cm x 7 mm x 6 cm plate inclined 60° over the horizontal. The contact angle is 70°. Pure oxygen as the gas phase. Pure water as the liquid phase with a liquid load of 38 cm/s. 1 atm absolute gas phase pressure.

$$F - factor = v_g \sqrt{\rho_g} \tag{6.1}$$

The F-factor is a measure of the kinetic energy of the gas phase since it takes into account both the gas velocity and its density.

Velocity profiles are specified at the gas inlet by means of UDFs in order to avoid a sharp transition in the velocity values associated to both liquid and gas inlets. The same

velocity profiles with negative values are used for the counter-current calculations.

The transient development of the oxygen mass fraction within the liquid film is represented in figure 6.4, which also displays the three different stages previously identified in section 5.4. The liquid injection velocity is kept constant, i.e. 38 cm/s. The results show that, in general, the mass transfer is enhanced when momentum is applied to the gas phase, being the enhancement more pronounced with the co-current flow configuration. This behaviour is explained by the drag between the gas and the liquid, which affects the hydrodynamics. In fact, drag causes the spreading of the liquid film, resulting in a greater interfacial area and enhanced oxygen absorption rate for the co-current configuration as well as a smoother transition between the three stages of the transient development. Therefore, drag helps the liquid spreading. The opposite happens for the counter-current configuration, in which the liquid is hold within the domain by the gas phase, hindering the development of the liquid film.

Figure 6.5 shows the values of the oxygen absorption rate against the absolute gas pressure including also the effect of the gas velocity and the flow configuration. The graph confirms the tendency observed in figure 6.4, by which the oxygen mass transfer rate is enhanced when a certain amount of momentum is applied to the gas, being the effect more advantageous for the case of co-current flow than counter-current.

As a conclusion, the importance of the gas velocity and the flow configuration has been highlighted. Co-current flow has been proved to be more convenient than counter-current in the case of an inclined plate due to a better liquid spreading caused by the gas drag. However, counter-current configuration is widely used in industry. In the case of an ideal geometry such as the inclined plate considered here, the drag caused by the gas phase flattens the liquid film whereas in an intricate geometry such as a structured packing the counter-current disposition is more favourable, due to the fact the liquid phase undergoes break-up that gives rise to the formation of droplets and rivulets. The appearance of the

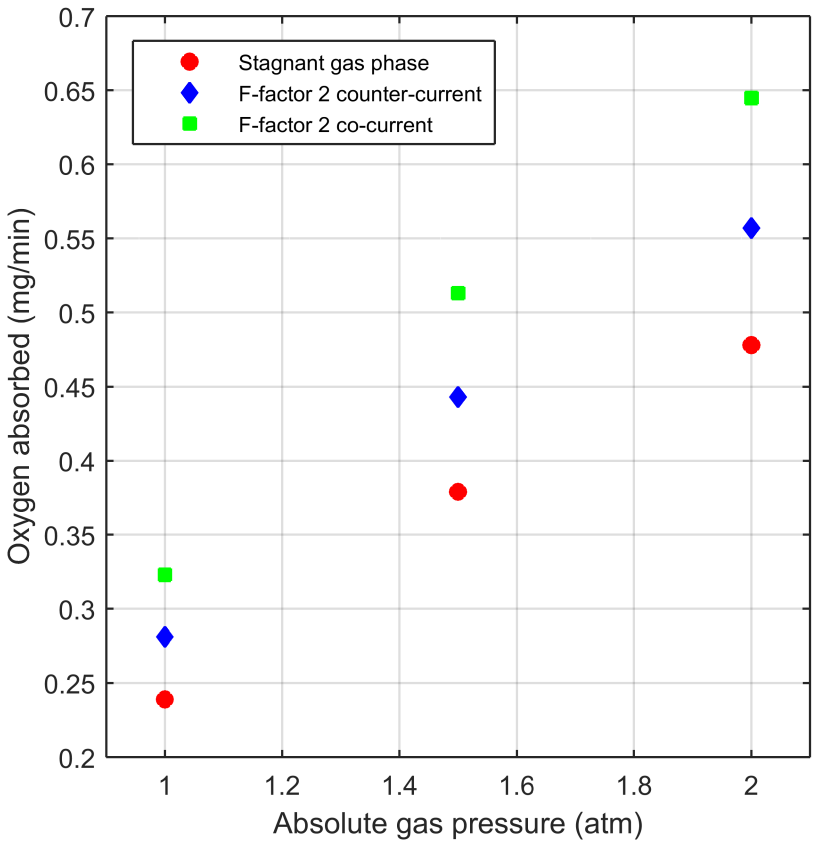

Figure 6.5: Oxygen absorption rate vs absolute gas pressure at pseudo-steady state conditions. The graph also shows the effect of the flow configuration and the gas velocity. 5 cm x 7 mm x 6 cm plate inclined 60° over the horizontal. The contact angle is 70°. Pure oxygen as the gas phase. Pure water as the liquid phase with a liquid load of 38 cm/s.

liquid break-up enhances the amount of interfacial area between the fluids and the mass transfer performance [203, 205].

6.4 Effect of liquid-solid contact angle

This section deals with the analysis of the influence of the contact angle between the liquid phase and the solid surface on the interfacial area. The contact angle is the result of the balance of the cohesion and adhesion forces. Cohesion is explained by the affinity

between the molecules constituting the liquid phase whereas adhesion is related to the affinity between the liquid molecules and those of the solid material. Water spreading is enhanced when adhesion to the solid surface is greater than cohesion. When this happens, the contact angle presents values below 90°, i.e. wetting conditions. Higher values of the contact angle mean that cohesion dominates over adhesion, i.e. non-wetting or hydrophobic conditions. Figure 6.6 shows images of the flow regime observed for both wetting and non-wetting conditions. The injection velocity taken to carry out the test is the same on both simulations and is equal to 38 cm/s. The image on the left corresponds to hydrophobic conditions, i.e. 100° and cohesion dominating over adhesion. As used in for previous analyses, a contact angle of 70° is set for the wetting conditions (image at the right-hand side).

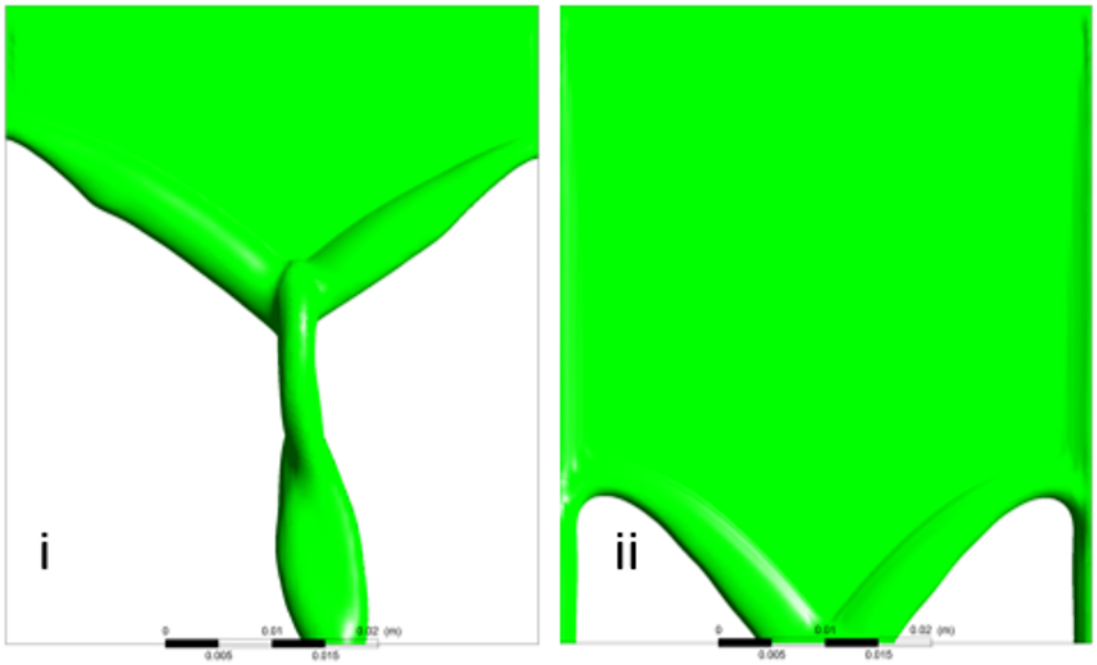

Figure 6.6: Snapshots of the flow regime at pseudo-steady state for both i) hydrophobic, and ii) hydrophilic conditions. 5 cm x 7 mm x 6 cm plate inclined 60° over the horizontal. Pure oxygen as the gas phase. Pure water as the liquid phase with a liquid load of 38 cm/s. F-factor 2 with counter-current disposition. Gas phase absolute pressure 1.5 atm..

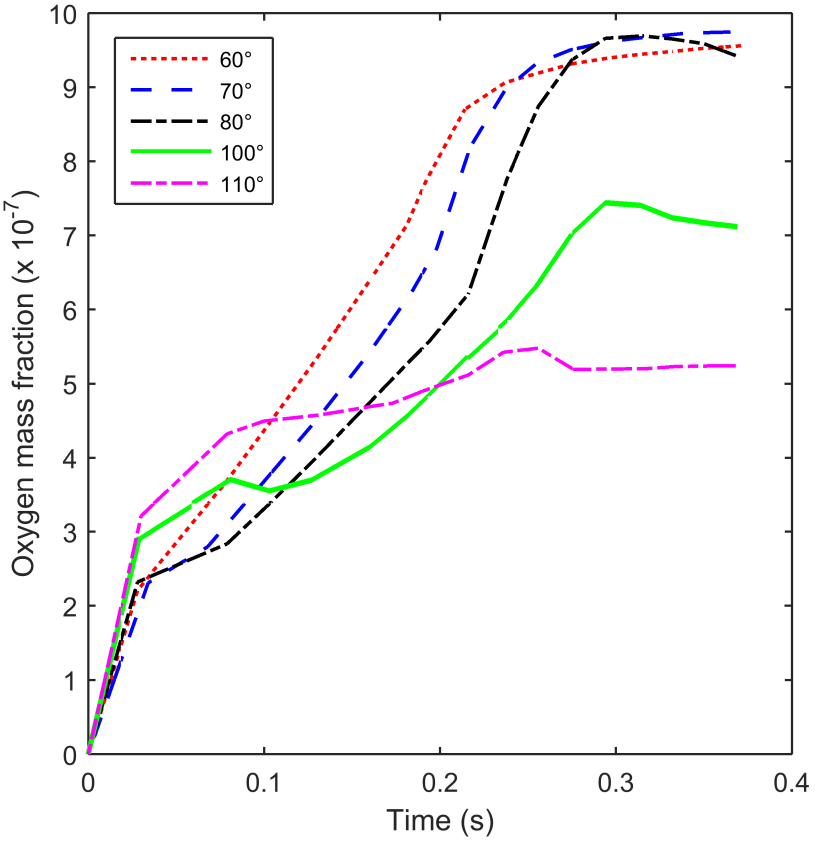

Figure 6.7: Transient behaviour of the mass transfer for different values of the contact angle. 5 cm x 7 mm x 6 cm plate inclined 60° over the horizontal. Pure oxygen as the gas phase. Pure water as the liquid phase with a liquid load of 38 cm/s. F-factor 2 with counter-current disposition. Gas phase absolute pressure 1.5 atm.

The images show an important decrease in the amount of wetted area upon non-wetting conditions. The first remarkable characteristic is that the lateral rivulets disappear. The plate corners are the areas where the effects of capillarity are more pronounced. Therefore, the lateral rivulets disappear when a hydrophobic contact angle is set in the simulation parameters. The area covered by a fully developed liquid film also diminishes. The results confirm that hydrophilic conditions can enhance the liquid spreading hence the mass transfer performance.

Figure 6.7 shows the transient behaviour of the averaged oxygen mass fraction for

different values of the contact angle tested; i.e. the liquid injection velocity is kept constant at 38 cm/s. It can be observed that there is no substantial influence of the contact angle on the oxygen mass fraction for wetting conditions once the pseudo-steady state is reached. However, an important decay is found for the hydrophobic cases. This difference is caused by the decrease in the interfacial area discussed earlier in this section.

Since the contact angle depend on the material of the structured packing, this conclusion highlights the importance of the selection of the correct material for the manufacturing process of the structured packing.

6.5 Conclusions

The study presented in Chapter 5 has been extended to assess the influence of various operating parameters on the mass transfer rate from the gas phase to the liquid phase. The study begins with the influence of the liquid viscosity. This parameter affects the diffusivity of the solute in the liquid film as described by the Wilke-Chang equation. The results show the expected tendency according to the theory, which is a diminution on the mass transfer rate as viscosity increases. Two aqueous MEA solutions used in industry and pure water are utilised as liquids to run the simulations, showing a huge diminution on the non-reactive absorption rate for the amine solutions compared to the case of pure water due to the difference in the viscosity between MEA and water. In addition, two values of the liquid injection rate were also tested, both presenting the same tendency. The velocity affects the absorption rate through the increase in the liquid spreading, hence greater absorption rates at greater velocities. The general conclusion is that increasing the viscosity of the liquid phase has a detrimental effect on the non-reactive mass absorption rate of the system.

The second parameter included in this study is the gas phase pressure. Pressure affects

the absorption process via a change in the solubility. A greater solubility implies a higher solute concentration at the interface, which causes a higher concentration gradient, hence enhanced absorption source terms. Three different values of the gas pressure have been tested, showing the beneficial impact it has on the absorption rate. An improvement of up to 60% is found for a 0.5 atm increment on the gas pressure. Normally, absorption columns in post-combustion CCS facilities work at atmospheric pressure. An increment in the gas pressure could be beneficial for the mass transfer performance as it is suggested in the present study but some experimental work should be carried out in this regard. A more detailed study assessing the economics and risks would be necessary to determine the suitability of a pressurised absorption column.

The chapter follows with the influence of the gas phase velocity and the flow configuration. Co- and counter-current configurations are considered, both showing enhanced absorption rate when compared to the stagnant gas case. Therefore, implementing momentum to the gas phase is shown to be beneficial regardless of the flow configuration. Co-current disposition causes the flattening of the liquid film, augmenting the interfacial area and improving the mass transfer rate. Counter-current disposition tends to hold the liquid within the domain, which is also beneficial by virtue of a higher contact time between phases. Co-current simulations present the best results for the mass transfer performance. However, amine scrubbers work normally at counter-current disposition. This difference is attributed to the fact that the ideal case of an inclined plate is considered in this study whereas, in an actual structured packing column, counter-current flow causes an important liquid break-up, which gives rise to enhanced values of the interfacial area.

The influence of the contact angles has also been included, showing results for wetting and non-wetting conditions. Contact angle depends on both the cohesion of the liquid molecules and the adhesion forces between the liquid and the solid surface. The results show an important dependence on the contact angle, with wetting conditions offering an

improved liquid spreading over the plate and higher absorption rates. Since the contact angle depends on the material with which the packing is manufactured, it can be concluded that the selection of the solid material is crucial for the good performance of the absorption column.

From all the parameters included in this study, contact angle and gas pressure are the most influential. This chapter closes the study of the hydrodynamics and the mass transfer without chemical reaction at small-scale. The study of the reaction kinetics of the CO_2-MEA system at small-scale is included in Chapter 7.

Chapter 7

Reactive mass transfer at small-scale

This chapter constitutes a further step in the development of the CFD model. In the previous two chapters the liquid maldistribution phenomenon has been studied at small-scale, along with the absorption without chemical reaction and the effect of several operating parameters. In this chapter, the study of the hydrodynamics of aqueous MEA gravity-driven liquid films is extended. The transient development and the velocity profiles of the aqueous MEA liquid films are analysed, showing important differences with respect to the case of pure water. Later, the UDF is expanded in order to include also the mass source terms that describe the consumption/creation of reactants/products of the chemical reaction between the CO_2 and the MEA. This chapter complements chapters 5 and 6 and closes the modelling at small-scale.

The application of the UDF to describe the CO_2-MEA chemical system at small-scale gives the possibility of analysing some aspects that would be difficult to accomplish with experimental techniques. The analysis of the concentration profiles within the liquid film is one of those aspects.

The reaction between the CO_2 and the MEA follows the fast pseudo-first order behaviour. This is characterised by the fast kinetics of the reaction. The timescale governing

the diffusion of the solute into the liquid film is slower, which results in the molecules of CO_2 being immediately consumed once they cross the gas-liquid interface. Therefore, the chemical reaction only takes place in the interface. One of the objectives of the present chapter is to reproduce this fact. The CO_2 concentration profiles are presented and compared to the hypothetical case in which the chemical reaction is suppressed in order to highlight the capability of the present model to describe this aspect.

Another interesting aspect regarding the reactive mass transfer is the analysis of the enhancement factor and the liquid-side mass transfer coefficient. The enhancement factor is a measure of the gain in the absorption rate that takes place in reactive mass transfer when compared to non-reactive conditions. The enhancement factor depends on the concentration of MEA in the aqueous solution. Results describing the relationship between the amine concentration and both the enhancement factor and the liquid-side mass transfer coefficient are presented in this chapter. The conclusion taken from these results is that, on the one hand, the chemical reaction leads to an increase in the absorption rate, justifying the selection of reactive mass transfer against non-reactive mass transfer for post-combustion CCS, and on the other hand, that higher amine concentrations are beneficial to the reactive absorption process.

7.1 Hydrodynamics of aqueous MEA solutions

First, the hydrodynamics of the aqueous MEA solution are analysed. In the previous chapters, pure water has been used as the liquid phase and oxygen has been used as the gas being absorbed by the liquid. This allows assessing only the absorption without chemical reaction. The transient behaviour of the aqueous MEA liquid film, which shows a slower development than the oxygen-water system due to the difference in viscosity, and the analysis of the velocity profiles is presented.

One of the conclusions from the previous chapters is that hydrodynamics play an essential role in the mass transfer performance of the system. The interfacial area is appointed as the most influential parameter affecting mass transfer, hence the importance of also studying the hydrodynamics of the CO_2-MEA system [117]. The discussion in this section begins with the transient development of the wetted area and ends with the analysis of the liquid film thickness and velocity profiles.

7.1.1 Transient development of the interfacial area

The evolution of the wetted area can be observed in figure 7.1 for three different amine solutions and pure water with the same liquid injection velocity, i.e. 38 cm/s. The evolution of pure water has also been included to easily establish the comparison between the amine solutions and a low viscosity fluid such as water. The graph shows a substantial difference between the evolution of pure water and the aqueous MEA solutions.

Generally, the liquid development becomes slower with the increase in viscosity that the use of the MEA solutions carries. The system can take from 1.0 s (MEA 30% wt., 7.9 cP) to 1.2 s (MEA 40% wt., 10.2 cP) and 1.5 s (MEA 50% wt., 12.5 cP) to reach the pseudo-steady conditions depending on the amine contents whereas pure water needs 0.3 s to reach them. There is also a substantial difference between the development of the MEA solutions and the case of pure water. However, the difference among the three solutions is smaller. The variation in viscosity between the water, i.e. dynamic viscosity of 1 cP, and the MEA, i.e. 24 cP, is what causes this difference. The slower development of the liquid film for higher values of the viscosity is also explained by means of the velocity profiles introduced later in this chapter. Although the velocity at the inlet is the same for the three cases, the velocity profiles change during the development of the liquid film and depend on the value of the dynamic viscosity. A higher viscosity imply smaller

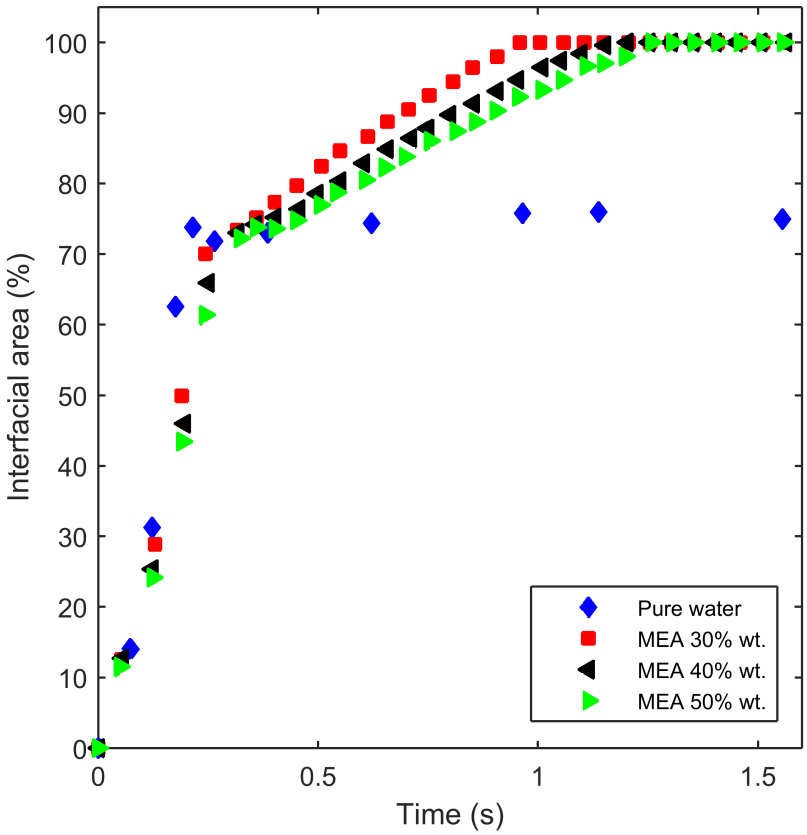

Figure 7.1: Transient development of the interfacial area for three amine solutions (30%, 40%, and 50% wt. aqueous MEA). 3 cm x 7 mm x 6 cm plate inclined 60° over the horizontal. The contact angle is 70°. The liquid injection velocity is 38 cm/s. CO_2 at atmospheric pressure as the gas phase.

velocities hence the slower development seen in the figure.

The development of the liquid film presents three stages that can be visualised in figure 7.2. The latter shows snapshots of the liquid film development for the MEA 30% wt. solution and 38 cm/s liquid injection velocity. The first stage of the development lasts approximately 0.3 s. It corresponds to the left-hand side image and is characterised by a rapid increase of the wetted area caused by both the extension of the rivulets and the advance of the front wave. This section lasts until the three rivulets reach the outlet. In the second stage, i.e. central image, the rate of change of the wetted area decreases. In

this stage, only the advance of the front wave takes place, being the increase of the wetted area due only to this contribution. This stage finishes when the liquid covers the whole plate. The third stage begins after approximately at 1 s flow time. The high viscosity of the amine solutions causes the appearance of the second stage, which cannot be observed in the case of pure water.

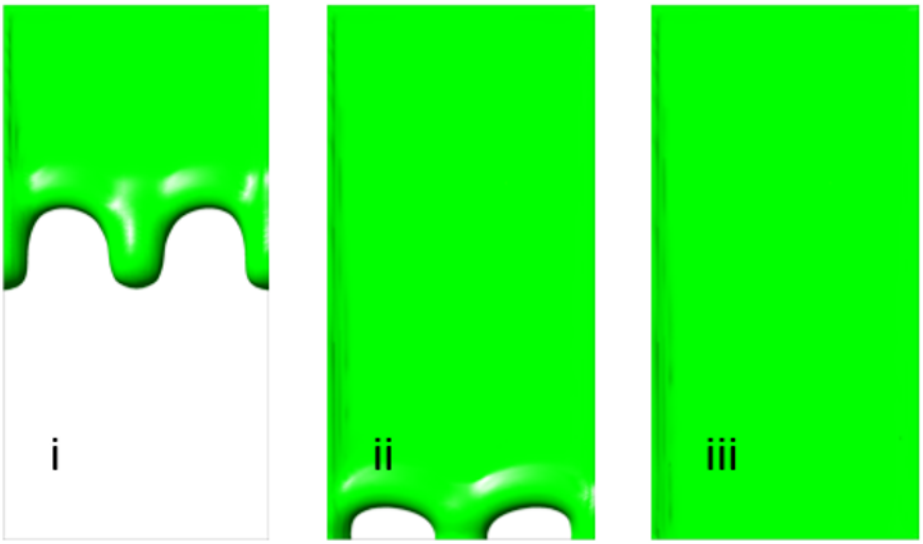

Figure 7.2: Images of the development of the 30% wt. MEA solution liquid film at i) 0.1 s, ii) 0.7, and iii) 1.5 s. 3 cm x 7 mm x 6 cm plate inclined 60° over the horizontal direction. The contact angle is 70°. The liquid load is 38 cm/s.

During the development of the liquid film and until the three fluids reach the pseudo-steady state, the greatest values of the wetted area correspond to the lowest values of viscosity. In fact, during the first stage of the liquid development, the bigger amount of the wetted area corresponds to the case of pure water. However, pure water does not cover the whole plate whereas the amine solutions have proved to do so at all the concentrations tested.

As has been discussed already, the amount of wetted area is one of the most influential parameters affecting the mass transfer performance of the reactor and it is important to

maximise it as much as possible. From the results presented in this section, the increase in the liquid viscosity is beneficial due to the increase in the wetted area, hence improving the mass transfer process.

7.1.2 Velocity profiles

A comparison plot for the velocity profiles of the three different solutions at the same liquid injection velocity, i.e. 38 cm/s, is presented in figure 7.3. The liquid film thickness increases with the viscosity of the fluid as can be seen in the horizontal axis of the graph. The increase in the thickness is substantial, going from 0.7 mm for the MEA 30% wt. solution to 0.8 mm for the MEA 50% wt, representing a 15% change with the base case of the MEA 30% wt. solution. A 15% increase in the liquid film thickness would imply the same increase in the liquid hold-up if the assumption of the perfectly developed film is taken. This would also imply a substantial increment of the weight of the column and of the wet pressure drop. The velocity is represented in the vertical axis, showing that thicker liquids give slower velocities. Both tendencies are justified with Nusselt's theory [178].

The fact that thicker liquids have lower velocities is also in accordance with the results represented in figure 7.1, in which it is shown that it takes more time for the liquid film to reach the pseudo-steady state as its viscosity increases. As a conclusion, increasing the amine concentration produces a slower development of the liquid film, which eventually finishes covering up the entire plate. Contrarily, water needs to be injected at higher velocities to reach the full film flow. This could be interesting from an industrial point of view since an increase in the interfacial area implies better mass absorption performances. On the other hand, higher viscosities give thicker liquid films hence bigger values of the liquid hold-up.

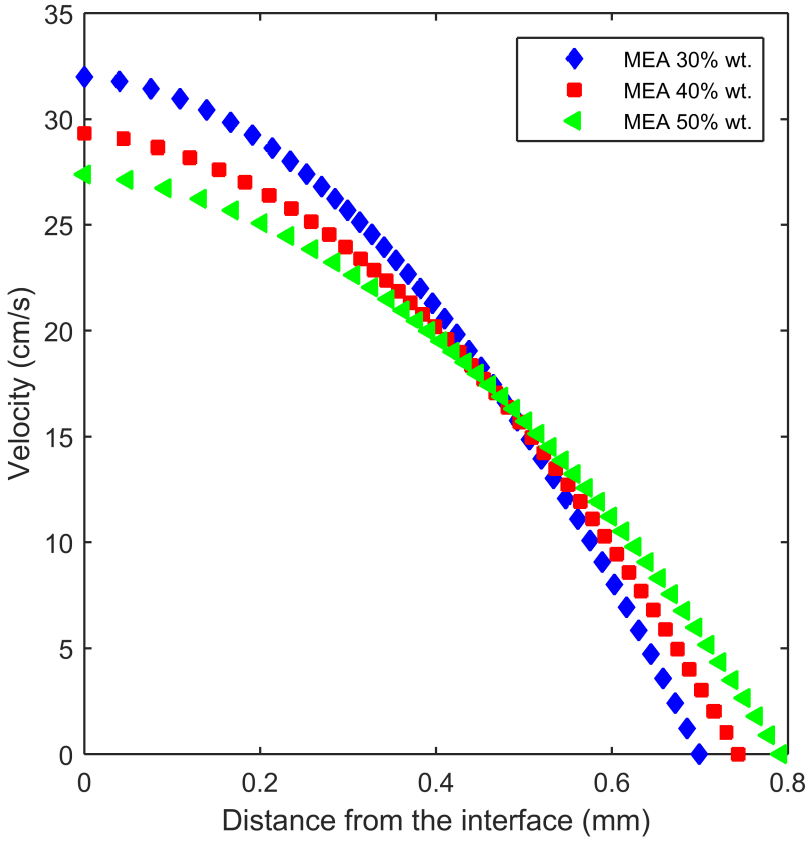

Figure 7.3: Velocity profiles for the three amine solutions (30%, 40%, and 50% wt. aqueous MEA). 3 cm x 7 mm x 6 cm plate inclined 60° over the horizontal. The contact angle is 70°. The liquid injection velocity is 38 cm/s. CO_2 at atmospheric pressure as the gas phase. 3 cm x 7 mm x 6 cm plate inclined 60° over the horizontal. The profiles are taken at the centre of the computational domain.

7.2 Effect of MEA concentration on the enhancement factor

Figure 7.4 shows the values obtained for the enhancement factor for the three different amine solutions considered at two liquid injection velocities (38 cm/s and 45 cm/s). As can be seen, the increase in the concentration of amine in the solution gives rise to an increase in the enhancement factor, which relate to higher reaction rates. The order of

magnitude of the enhancement factor from the CFD simulations is in agreement with reported data from the literature [196]. This behaviour can be explained by means of the kinetic theory which states that a chemical reaction occurs. According to the kinetic theory, a chemical reaction occurs when the collision of the molecules of the reactants takes place. A higher presence of amine molecules in the solution leads necessarily to a higher probability of collision.

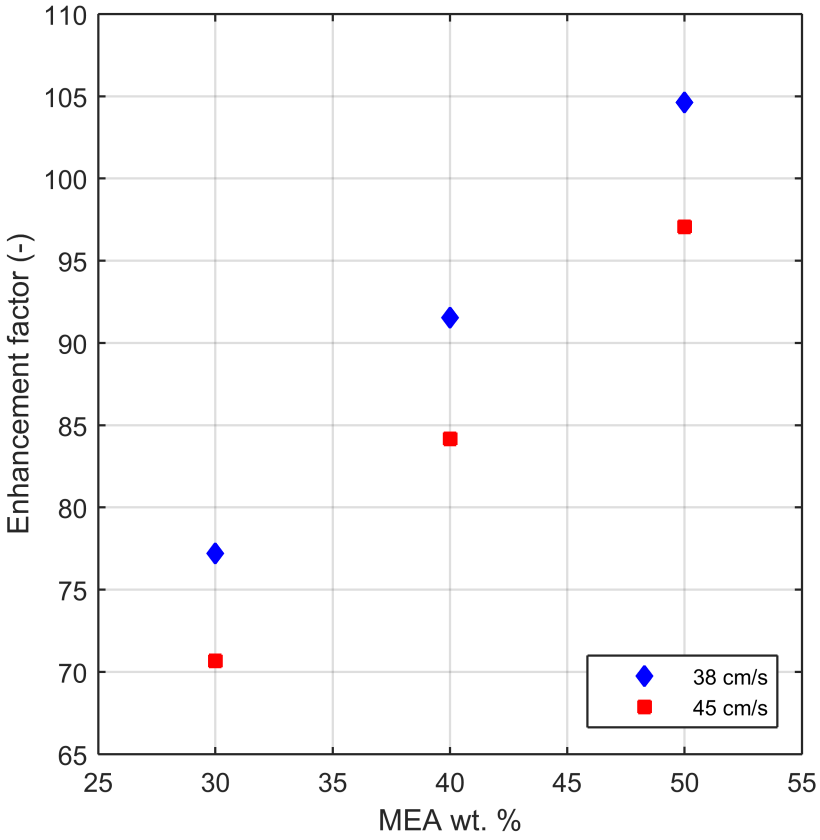

Figure 7.4: Values of the enhancement factor for the three amine solutions (30%, 40%, and 50% wt. aqueous MEA). 3 cm x 7 mm x 6 cm plate inclined 60° over the horizontal. The contact angle is 70°. Two values of the liquid injection velocity are considered (38 cm/s and 45 cm/s). CO_2 at atmospheric pressure as the gas phase.

As an additional explanation to the tendency shown in figure 7.4, a direct relationship between the enhancement factor and the liquid film thickness is also reported in the litera-

ture [197]. An increase in the liquid film thickness comes necessarily from an increase in the viscosity of the liquid phase through equation (3.106). Therefore, it can be concluded that the enhancement factor should increase with the amine concentration.

The liquid load can also influence the enhancement factor as observed in the figure. The values of the liquid injection velocity studied are 38 cm/s and 45 cm/s. If a single value of the amine concentration is considered, there is a reduction of the enhancement factor for higher liquid loads. The reduction is constant and approximately equal to 8% for the three different amine concentrations tested. This reduction is caused by the decrease in the exposure time that a larger liquid load implies. The exposure time affects the liquid-side mass transfer coefficient through equation (3.78). A decrease in the exposure time implies an increase in the liquid-side mass transfer coefficient, which in turn causes a decrease in the Hatta number, i.e. equation (3.89). The diminution in the Hatta number implies necessarily the reduction in the enhancement factor.

In conclusion, results show that richer amine solutions relate to higher enhancement factor values. As explained in Section 2.3.2, in the present work the enhancement factor is approximately equal to the Hatta number, i.e. equation (3.89), because a fast pseudo-first order is considered. Increasing the Hatta number involves a positive impact on the mass transfer performance and a better CO_2 absorption rate, i.e. equation (3.88). In other words, increasing the concentration of MEA in the solution favours the absorption of CO_2. On the other hand, as discussed in section 7.1, it is detrimental to the pressure drop as the thickness of the liquid film increases. Therefore, a trade-off in the amine concentration is required to balance those converse effects.

7.3 Effect of MEA concentration on the mass transfer coefficient

A variation in the amine concentration also affects the liquid side mass transfer coefficient as shown in figure 7.5. An inverse relationship between the variables is observed.

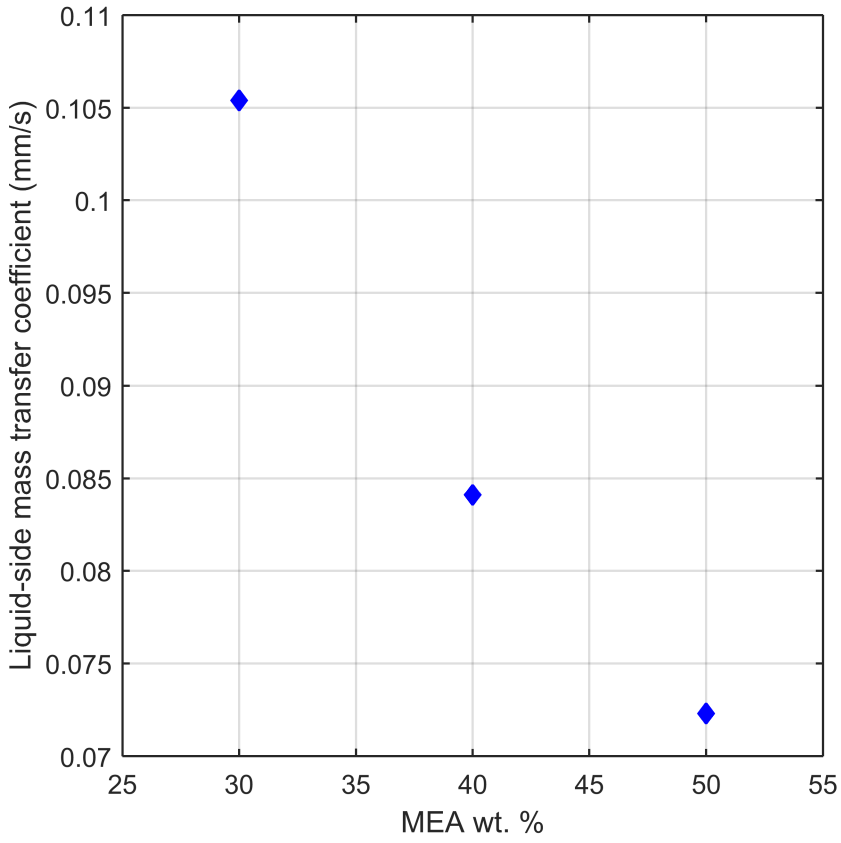

Figure 7.5: Values of the liquid-side mass transfer coefficient for the three amine solutions (30%, 40%, and 50% wt. aqueous MEA). 3 cm x 7 mm x 6 cm plate inclined 60° over the horizontal. The contact angle is 70°. CO_2 at atmospheric pressure as the gas phase.

The increment in the viscosity associated to richer amine solutions affects the diffusivity of the solute within the liquid film, reducing the liquid-side mass transfer coefficient. This is caused by the latter being proportional to the squared root of the diffusivity ac-

cording to equation (3.78). However, the same increase in the MEA concentration has the beneficial effect of increasing the reaction rate.

As a general conclusion, an increase in the amine concentration carries higher values of the enhancement factor, which can be interesting from an industrial point of view due to the beneficial impact on the absorption performance of the structured packing column. On the other hand, the effect of the injection velocity on the enhancement factor has also been tested, concluding that an increase in the velocity of the liquid has a detrimental impact. Since the liquid load has also been proved to result in a better absorption, i.e. through better liquid spreading, further work should be carried out in order to assess whether or not an increase in this parameter is beneficial to the whole process.

7.4 Effect of MEA concentration on the species profiles

The influence of the MEA contents on the CO_2 concentration profiles within the liquid film is analysed in figure 7.6. The three cases have been obtained for a liquid injection velocity of 38 cm/s. The graph represents the distance from the interface in the horizontal axis. Therefore, the vertical axis on the left-hand side would physically correspond to the gas-liquid interface whereas the surface of the metallic plate would lie on the right-hand side of the graph.

The values of the concentration profiles are greater for low MEA concentrations. These results can be explained by the fact that a higher amine concentration carries an increase in the reaction rate, hence a faster consumption of the CO_2 and lower concentrations within the liquid film. Secondly, the MEA concentration influences directly the value of the enhancement factor. Greater amine concentrations mean higher enhancement factors, hence an increased absorption rate through the gas-liquid interface. A sufficiently large mass transfer through the interface can only happen if the concentration gradient of

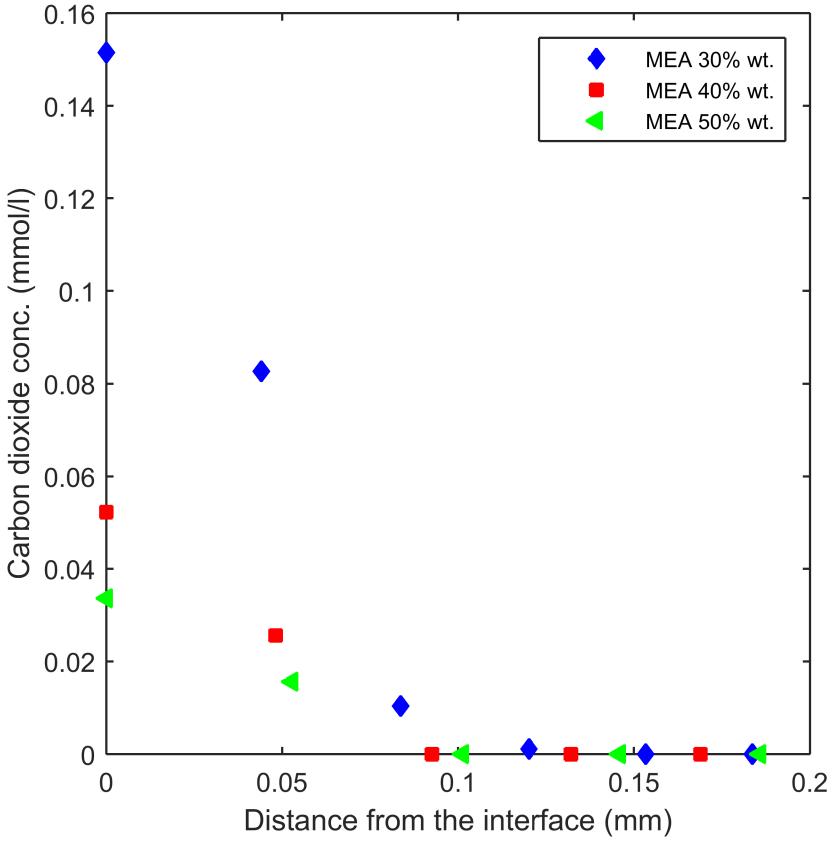

Figure 7.6: CO_2 concentration profiles for the three amine solutions (30%, 40%, and 50% wt. aqueous MEA). 3 cm x 7 mm x 6 cm plate inclined 60° over the horizontal. The contact angle is 70°. Pure CO_2 at atmospheric pressure as the gas phase. The liquid injection velocity is 38 cm/s. The profiles are obtained at the centre of the computational domain.

CO_2 between the interface and the liquid bulk is high enough. Therefore, an important value of the concentration gradient is only possible when the concentration of CO_2 in the liquid film is low.

In the figure 7.6 the CO_2 concentration is equal to zero at approximately four computational cells beginning from the interface. The maximum distance from the interface represented in the graph has been set to 0.2 mm, since the concentration continues to be equal to zero as the data series progresses to the right-hand side of the graph. The fact

that the chemical reaction takes place only in the interface by virtue of the high Hatta number is thus well represented. To further highlight this point, the figure 7.7 shows the comparison between the cases with and without chemical reaction.

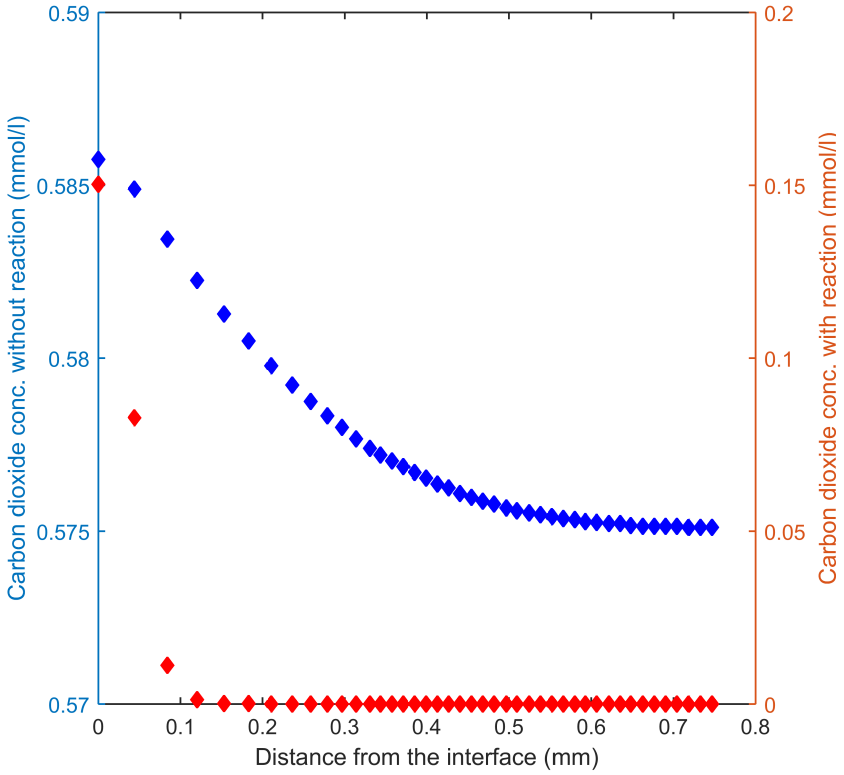

Figure 7.7: CO_2 concentration profiles with and without chemical reaction for 30% wt. aqueous MEA solution. 3 cm x 7 mm x 6 cm plate inclined 60° over the horizontal. The contact angle is 70°. Pure CO_2 at atmospheric pressure as the gas phase. The liquid injection velocity is 38 cm/s. The profiles are obtained at the centre of the computational domain.

For the mass transfer data series without chemical reaction, it can be observed that the CO_2 reaches the whole thickness of the liquid film. This series of data has been obtained by deactivating the source terms that define the creation or consumption of species due to the chemical reaction. The mass source terms that describe the absorption through the interface are defined in the region with a liquid volume fraction equal or higher than 0.5.

Therefore, the mass of the solute is created in the vicinity of the interface and progresses into the bulk of the liquid by diffusion.

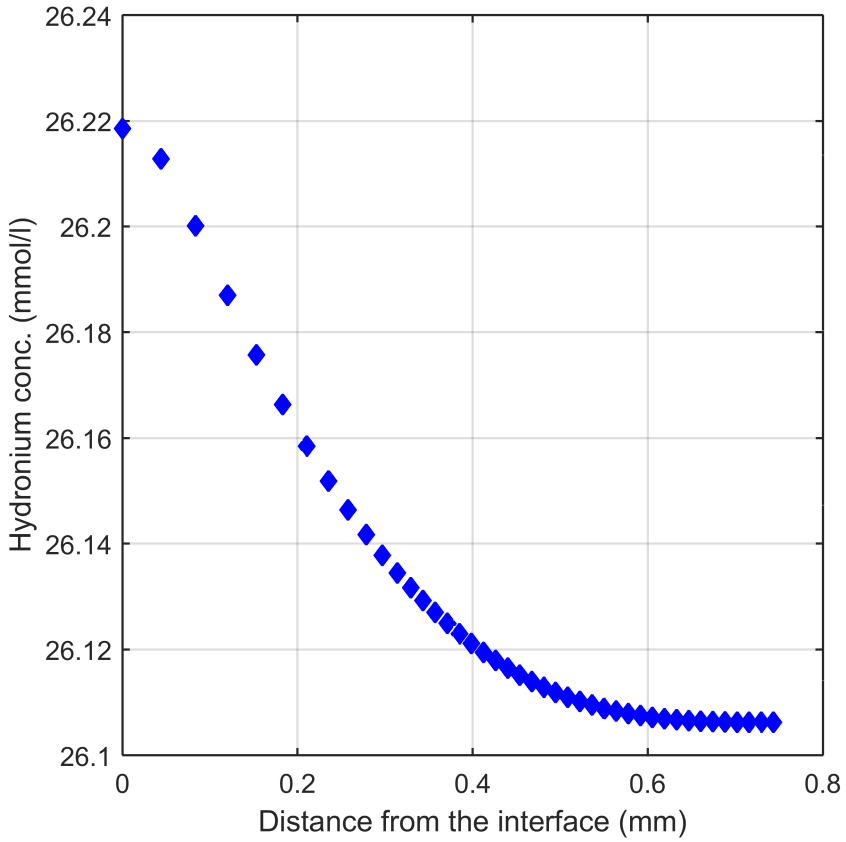

Figure 7.8: H_3O concentration profile for 30% wt. aqueous MEA solution. 3 cm x 7 mm x 6 cm plate inclined 60° over the horizontal. The contact angle is 70°. Pure CO_2 at atmospheric pressure as the gas phase. The liquid injection velocity is 38 cm/s. The profiles are obtained at the centre of the computational domain.

Conversely to the non-reactive mass transfer case, the source terms describing the consumption/production of reactants/products have been activated in the simulation set-up to obtain the data series for reactive mass transfer. These sources are defined in the computational cells that form the entire liquid film and not only in the interface. This gives the possibility of representing the absorption process in a more realistic way, that is to say, allowing the system to consume automatically any CO_2 molecule able to reach the

liquid bulk.

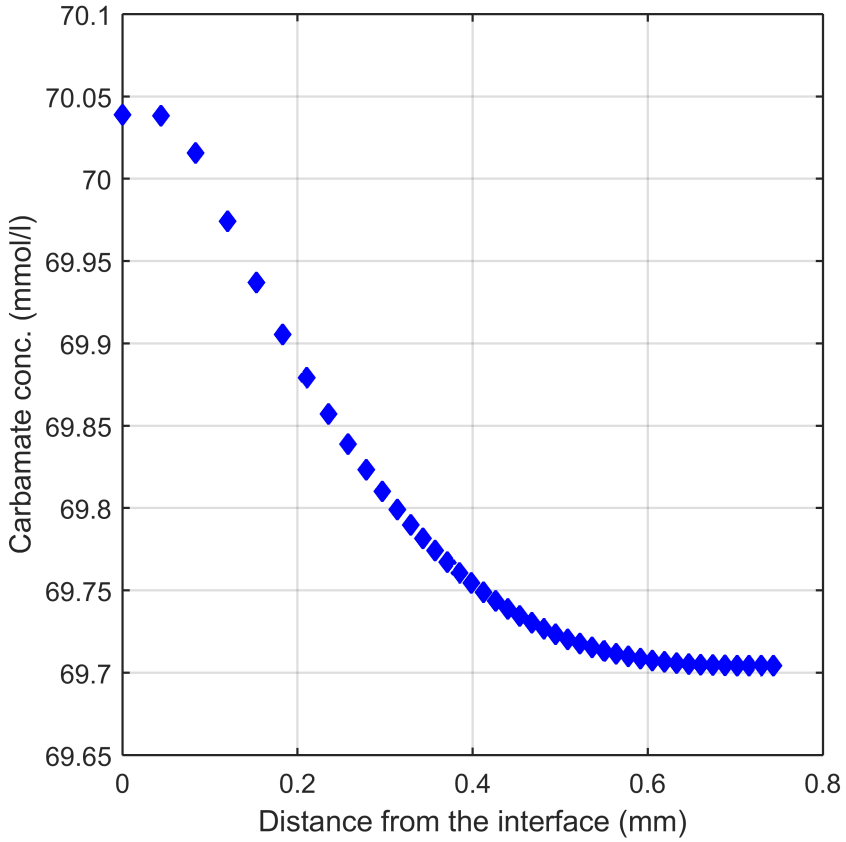

Figure 7.9: Carbamate concentration profile for 30% wt. aqueous MEA solution. 3 cm x 7 mm x 6 cm plate inclined 60° over the horizontal. The contact angle is 70°. Pure CO_2 at atmospheric pressure as the gas phase. The liquid injection velocity is 38 cm/s. The profiles are obtained at the centre of the computational domain.

The reaction kinetics of the carbamate formation reaction are fast enough to accomplish the consumption of the CO_2 in the liquid bulk. The chemical reaction takes place thus, in the interface. As a result, the penetration distance of the solute is approximately 0.1 mm. The maximum value of the concentration for the case without chemical reaction is 0.586 mmol/l whereas with chemical reaction is 0.15 mmol/l. The fact that lower values of the CO_2 concentration are found for the reactive mass transfer case are also in accordance with the fact that the CO_2 molecules are immediately consumed by the reaction

once they get into the liquid phase.

Figure 7.8 and 7.9 show the concentration profiles for the hydronium and the carbamate, respectively. These species are products of the carbamate formation reaction, i.e. equation (2.5), and their concentration was initially equal to zero. When the system reaches the equilibrium, the generation of these two species only takes place at those computational cells where the concentration of CO_2 is different from zero. As seen in the graph, a concentration different from zero exists within the whole liquid film thickness, which suggests that these two species have been generated in the interface and subsequently diffused into the liquid bulk in a similar way as the CO_2 when the mass source terms that describe the chemical reaction are deactivated.

7.5 Effect of reversibility and instantaneity

The main reaction considered in the CO_2-MEA system is the carbamate formation. The carbamate formation reaction kinetics are fast as indicated by the high value of the Hatta number. Upon these circumstances, the reaction approximates an irreversible fast pseudo-first order behaviour. Moreover, when there is also a high amine concentration in the liquid film, the system is said to approach an instantaneous behaviour.

According to this, the reversibility has been neglected in the UDF and the assumption that the enhancement factor is equal to the Hatta number has been taken. In order to check the validity of these assumptions, two simulations are run considering the reversibility and the value of the enhancement factor corresponding to the instantaneous case, i.e. equation (3.86). The correlation reported by Kale et al [156] is used to calculate the equilibrium constant.

The CO_2 concentration profiles for the three cases are presented in figure 7.10, where it can be observed that the difference between the data series is small. The results for both

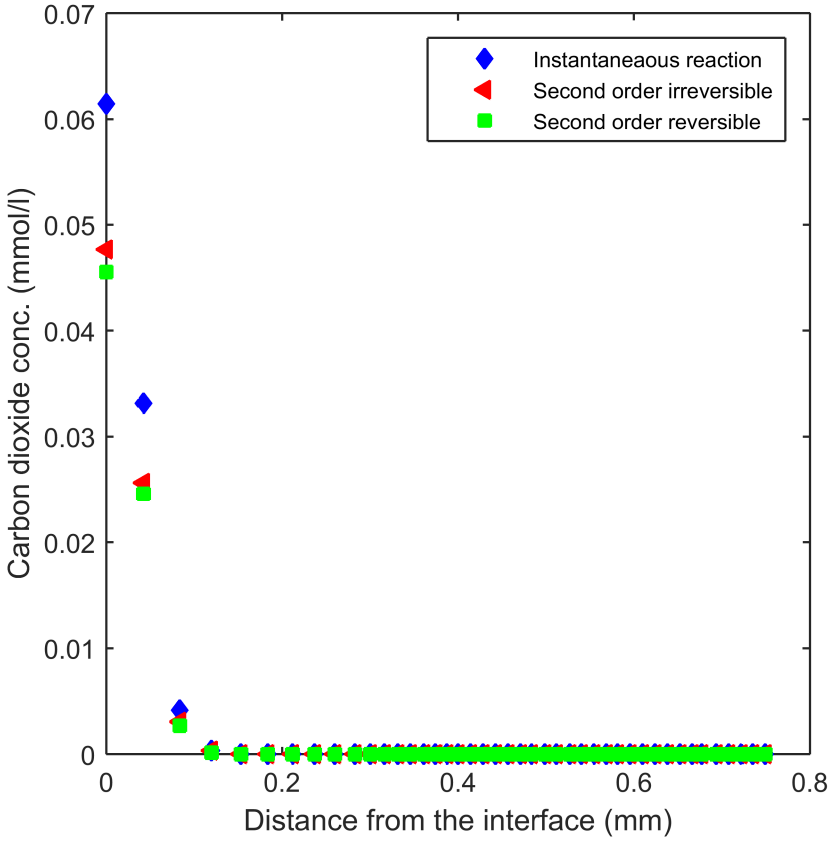

Figure 7.10: Carbamate concentration profile for 30% wt. aqueous MEA solution. 3 cm x 7 mm x 6 cm plate inclined 60° over the horizontal. The contact angle is 70°. Pure CO_2 at atmospheric pressure as the gas phase. The liquid injection velocity is 38 cm/s. The profiles are obtained at the centreline of the computational domain, at 1 cm from the liquid inlet.

reversible and irreversible second order match each other, which is a proof of the validity of the assumption of irreversibility. The data series corresponding to the instantaneous reaction presents slightly higher values of the CO_2 concentration due to the higher value of the enhancement factor when the reaction is considered as instantaneous, i.e. equation (3.86).

7.6 Conclusions

The results presented in this chapter focus on the implementation of the chemistry between the CO_2 and the MEA solution. The analysis of the hydrodynamics of aqueous amine solutions is carried out first in order to assess the transient behaviour of the MEA aqueous solutions and the velocity profiles within the liquid film.

The chapter begins with the analysis of the transient development of the liquid film. The formation of the liquid flow over the plate proves to be slower than in the case of pure water, due to the higher viscosity of the amine solution. The amine concentrations considered reach full film flow whereas, for the case of water, the rivulet flow appears at the same injection velocity. The liquid film thickness is the next aspect considered in the study. Higher amine concentrations give rise to thicker films, which in turn affects the liquid hold-up.

The chapter carries on describing the various aspects of the reactive mass transfer process. The discussion begins with the relationship between the MEA concentrations and both the enhancement factor and the liquid-side mass transfer coefficient. The model is able to reproduce the increase in the enhancement factor that a higher amine concentration implies. Also, the influence on the liquid side mass transfer coefficient is also analysed.

The analysis of the concentration profiles of the species involved in the carbamate formation reaction follows. The first conclusion is that the model is able to reproduce the fact that the carbamate formation reaction takes place only at the gas-liquid interface.

The influence of the amine concentration on the carbon dioxide profiles is also assessed, reaching the conclusion that lower concentration values are observed as the amine concentration increases. The concentration profiles of the hydronium and the carbamate are also included.

Finally, evidence of the validity of the assumption of neglecting the reversibility of

the reaction is presented. The results show that there is little difference between the CO_2 concentration profiles with and without considering the reversibility. The instantaneous behaviour of the reaction is also tested. The model is proved valid to reproduce the chemistry of the CO_2-MEA system, and can be used to test the performance of different amine solutions at small-scale. However, further work should be carried out in order to implement the model in commercial geometries.

Chapter 8

Meso-scale modelling with interface tracking

The implementation of the VOF interfacial tracking method at meso-scale is analysed in this chapter on a set of 4 REUs of the commercial structured packing MontzPak B1-250M. The purpose of this chapter is to expand the capabilities of meso-scale simulations, which so far have been essentially utilised for the study of dry pressure drop. The tracking of the free surface between the liquid and the gas phase in structured packings has been usually restricted in the literature to simulations at small-scale. Implementing the interface tracking method at meso-scale allows getting a more realistic insight about the multiphase flow inside structured packings. The results presented in this chapter focus on the study of:

- Interfacial area: the interfacial area has been appointed as the most influential parameter affecting the mass transfer performance [117]. Apart from having capital importance on the absorption process, the results show that the assumption of a perfectly developed liquid film falling along the metallic surface is not accurate enough. Irregular shapes in the liquid phase are observed due to the intricate geom-

etry of the structured packing.

- Liquid hold-up: is the volume of liquid phase per unit volume of structured packing when the absorber is working at steady-state conditions. The liquid hold-up influences the pressure drop along the column, since it modifies the velocity of the gas. Its study and accurate representation is then key to accurately model the pressure drop.

The effect of other operating parameters such as the viscosity of the liquid phase and the contact angle between the liquid and the solid surface of the packing are also assessed. The effect of the viscosity is assessed considering the variation of the MEA contents in the liquid solution. The contact angle has been recently studied in the literature by Haroun et al [117] (the values included in their work are 10°, 30°, and 70°), concluding that it can cause a significant variation on the interfacial area.

8.1 Liquid flow transient behaviour

Figure 8.1 shows the transient development of the multiphase flow within the structured packing at different liquid loads. The images include an isometric 3D view and cross-sectional liquid volume fraction plots at different time steps in order to visualise the development of irregularities in the liquid flow. The liquid load is obtained using an isosurface with a value of the volume fraction of 0.5. Results plotted in Figure 8.1 show a behaviour which is far from the formation of a perfectly developed falling liquid film. This result challenges the assumption that has been used in the literature to calculate the liquid hold-up and to predict the pressure drop [105, 199].

After an initial accumulation of liquid in the contact points, gravity acts causing the detachment of droplets and rivulets. The detached droplets reach the contact point un-

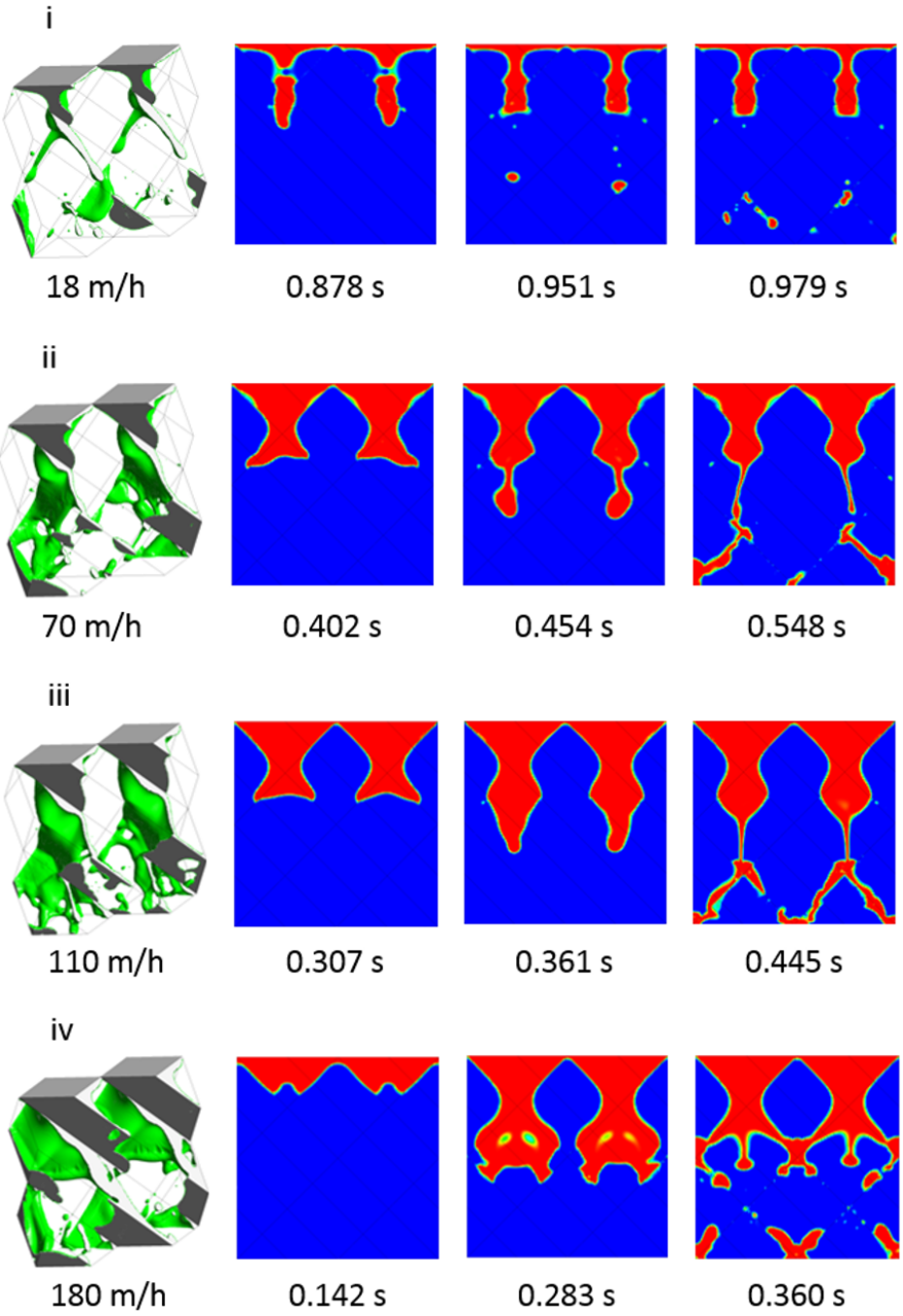

Figure 8.1: Transient development of the liquid flow at different liquid loads for the water-air system. Isometric view and volume fraction profiles. The liquid injection velocity is indicated in the bottom of each graph. Stagnant gas phase at atmospheric pressure. The isometric plots correspond to pseudo-steady state conditions.

derneath, causing the break-up of the liquid into smaller droplets and elongated shapes attached to the surface of the packing. The existence of similar liquid structures was already discussed by Bradtmöller et al [198], who found three different shapes named: film flow, contact point (C-P) areas and flooded regions. The film flow regime consists of elongated and thin liquid formations attached to the surface whereas C-P liquid areas and flooded regions are round, however there is a size difference between them. In the round formations the effect of the surface tension dominates over the shear stress that appears in the film flow areas due to viscosity and the adhesion to the solid surface.

It has been also observed that the pseudo-steady state conditions have been reached earlier as the liquid load increases. The point at which pseudo-steady state is reached varies from approximately 1 s for the case with a liquid load of 18 m/h to around 0.4 s for the liquid load of 180 m/h. The criterion to establish the pseudo-steady state conditions is the time at which there is no substantial change in both the liquid hold-up and the interfacial area. After the visualisation of the development of the liquid flow, the first two characteristics obtained from the implementation of the interface tracking method are the liquid hold-up and the interfacial area, which are analysed in the following sections.

As a conclusion, the characteristics of the liquid flow inside the packing lies far from the formation of the perfectly developed liquid film. As discussed in the following sections, the break-up of the liquid into irregular formations is preferable to the formation of the perfectly developed liquid film since the former results in bigger amounts of interfacial area available for mass transfer.

8.2 Liquid hold-up

The liquid hold-up influences other aspects of the absorber such as the characteristics of the support structure, i.e. due to the weight that the presence of liquid poses, and the

pressure drop.

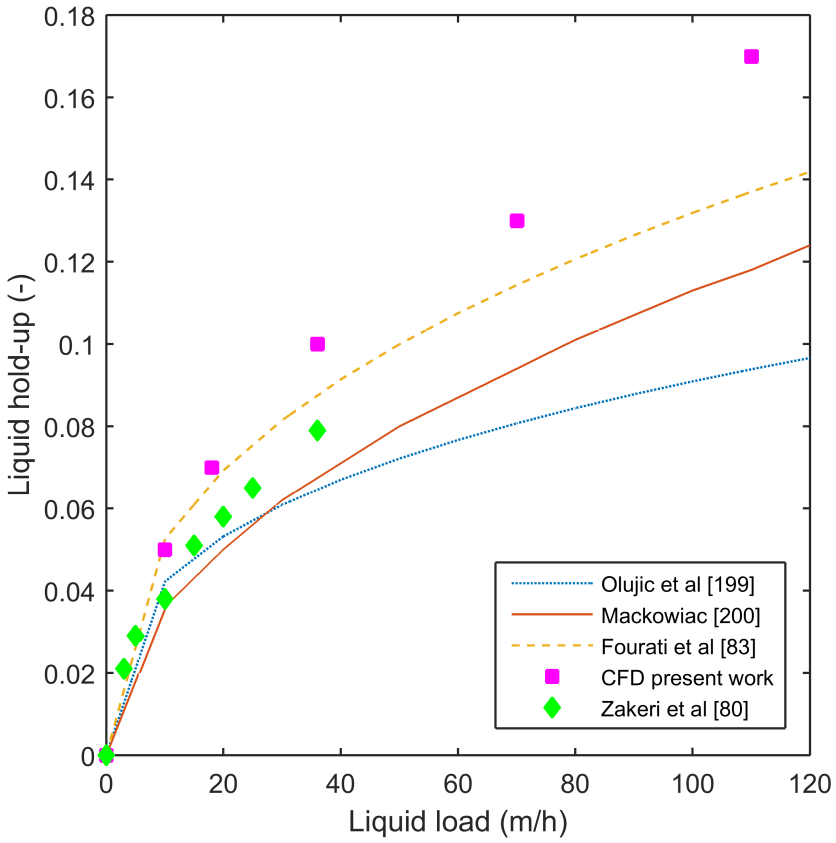

Figure 8.2: Liquid hold-up vs liquid load at pseudo steady state conditions. Stagnant gas phase at atmospheric pressure.

Since the interface tracking is restricted to 2D small-scale simulations in the literature, liquid hold-up has been usually calculated as the liquid film thickness times the specific area of the packing. This assumes that a perfectly developed liquid film is formed on the packing walls. As discussed in the previous section, the actual behaviour that takes place inside the structured packing lies far from this assumption. Figure 8.2 presents the results obtained for the liquid hold-up as a function of the liquid load. The results are compared with correlations previously published [80, 83, 199, 200]. The majority of the correlations found in the literature for the liquid hold-up reach values up to 120 m/h due to the size of

the experimental facilities, whereas the values found in industry lie in the range between 25 m/h and 250 m/h [117]. The general tendency in the experimental correlations as well as in the present simulations is that the liquid hold-up increases for the whole range of values represented. It is also observed that the rate of change of the liquid hold-up is steeper at low liquid loads whereas it gets slower as the amount of liquid per unit time injected into the domain increases.

The graph highlights the differences in the values of the liquid hold-up predicted by the different series of data, especially as the liquid load goes over 20 m/h. The simulations match the experimental results for values up to 20 m/h but begin to differ as the liquid load increases, presenting the highest difference with respect to the series of Olujić et al [199], which assumes the perfectly developed liquid film over the entire packing wall. As a general conclusion, the tendency is well represented. The simulations – as do the experimental correlations – overestimate the values obtained with the assumption of the perfectly developed liquid film in the industrial range of values, i.e. 25–250 m/h [117]. A substantial difference in liquid distribution along the column was observed by Fourati et al [83]. This difference is not considered in the correlations used to compare the present model. Therefore, higher values of the liquid hold-up are found at the top of the column, where the liquid distributors discharge. In fact, the present simulations reproduce the REUs placed in that area, which could be the cause of the overestimation observed in this study.

8.3 Interfacial area

The interfacial area is defined as the gas-liquid contact area per unit volume of packing. Figure 8.3 shows the effect of the Reynolds number on the interfacial area. The Reynolds number is calculated considering the velocity of the liquid at the inlet and the correspond-

ing liquid film thickness, i.e. Nusselt theory, as the characteristic length.

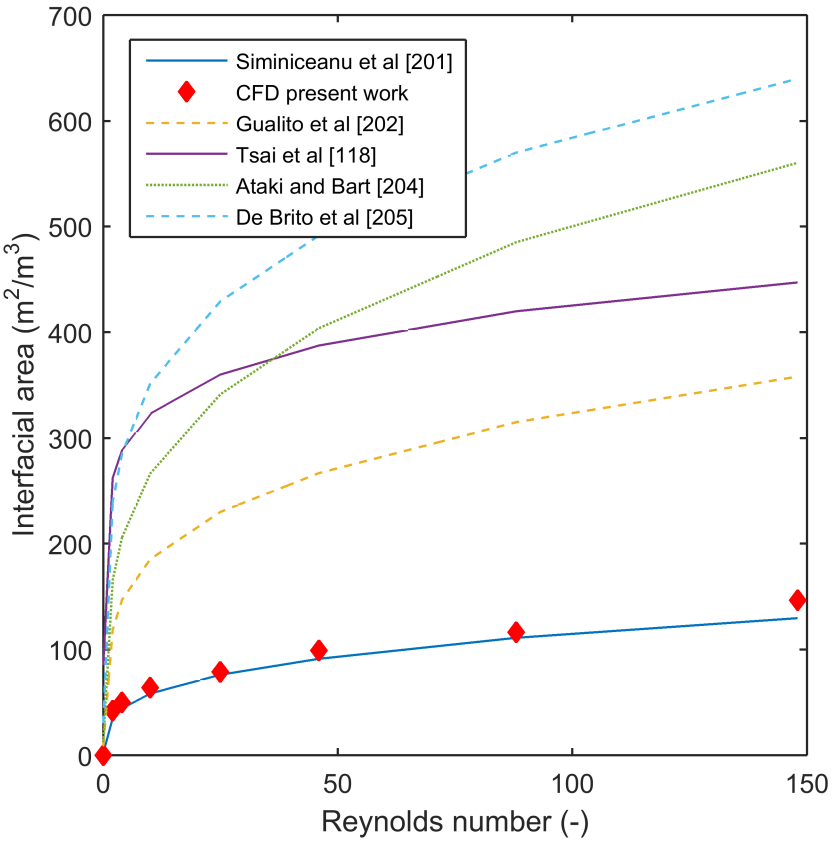

Figure 8.3: Interfacial area vs liquid load at pseudo steady state conditions. Stagnant air at atmospheric pressure as the gas phase.

Results show that the effective area increases with the liquid load. Analogously to what happened with the liquid hold-up, all the correlations included in the graph agree that the rate of change of the effective area is greater at lower values of the Reynolds number.

Nevertheless, high disparity among the different experimental series is observed. The simulations accomplished in this work give rise to values of effective area below the specific area of the packing. Although larger values would be expected, this behaviour was already proposed by Bravo and Fair [203]. These authors established that the value of

the effective area is composed by both the wetted area and the additional contribution of suspended droplets, ripples on the liquid film surface, etc. In the present simulations, the strict interfacial area between the gas and liquid phases has been considered, which could explain the difference between the simulations and the experimental data. The prediction from the present model matches the correlation developed by Siminiceanu et al [201]. In their work, the authors used a structured packing with a specific area of 750 m^2/m^3, which indicates that the results from their correlations are also lower than those predicted in the rest of correlations used in this study [118, 202, 204, 205].

The conclusion is that the tendency of the interfacial area as a function of the injected liquid flow rate is well represented in the model. The values obtained are underpredicted by the model but the discrepancies in the correlations found in the literature are also significant.

8.4 Pressure drop

The study of the pressure drop is divided in two parts: dry and wet pressure drop. Dry pressure drop predictions have been the purpose of meso-scale simulations in previous studies reported in the literature [97]. The dry pressure drop has been used as a way of obtaining a fast, qualitative evaluation of the pressure drop occurring inside the column since it constitutes an energy penalty within a CCS facility. After its calculation, an easy estimation of the wet pressure drop can be obtained using the correction factors included in the work of Fernandes et al [105], i.e. perfectly developed liquid film assumed, which can be described in the following steps:

- First, single phase simulations including only the gas are performed to obtain the dry pressure drop as a function of the gas load. The results are compared to experimental and previous CFD work found in the literature.

- Once the dry pressure drop is obtained, the correction factor reported by Fernandes et al [105] is used to obtain the corrected gas velocity. The difference between the previous work in the literature and the present thesis is that, instead of using the assumption of the perfectly developed liquid film, the liquid hold-up obtained with the simulations in the previous sections is used to calculate the wet pressure drop.

- After its correction, the new value of the gas velocity is introduced in the graph of the dry conditions to obtain the wet pressure drop.

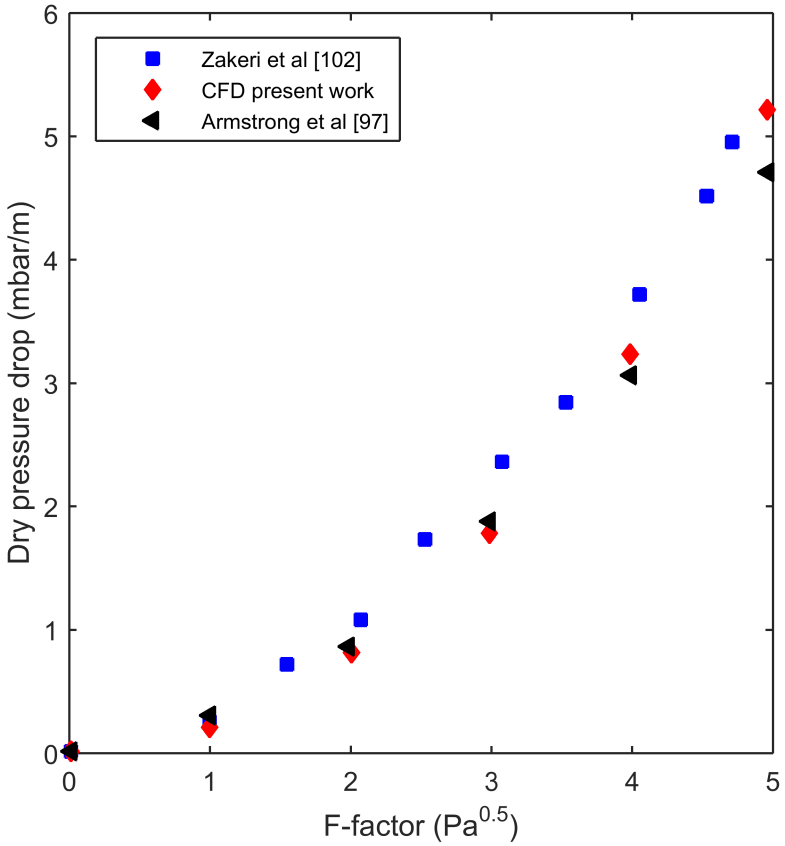

Figure 8.4: Comparison between the dry pressure obtained with this model and the data available in the literature. Air at atmospheric pressure as the gas phase.

Figure 8.4 shows the comparison between the dry pressure drop per unit length calcu-

lated with the present simulations, the simulations reported by Armstrong et al [97] and the experimental work of Zakeri et al [102].

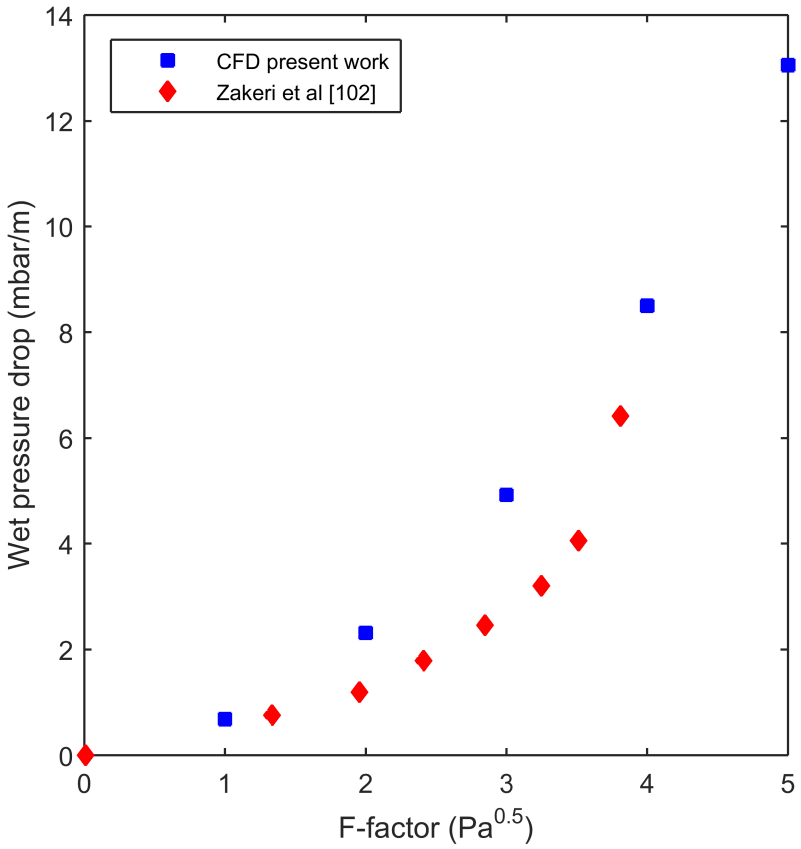

Figure 8.5: Comparison between the wet pressure obtained with this model and the data available in the literature. Air at atmospheric pressure as the gas phase. The experimental series is obtained with a liquid load of 35 m/h. The present CFD data are obtained with a liquid load of 36 m/h.

The three series of data have been obtained with air as the gas phase – constant density –, hence the F-factor (equation 6.1), can be considered as an alternative way of calculating the gas flow rate into the domain. The standard k-ε model is used for the turbulence. The graph shows that both simulations practically match the experimental results, although there are slight differences at the highest values of the F-factor. The parabolic tendency between both parameters is well predicted, reproducing the fact that the dry pressure drop

is a function of the squared velocity.

The results of the wet pressure drop are presented in figure 8.5. It can be observed that the wet pressure is overpredicted. Using the liquid hold-up predicted by this model to calculating the wet pressure drop is the cause of the overprediction. Although there is an important difference between both the experimental and the results obtained with the liquid hold-up prediction of this model, the tendency is reproduced and the model can be used to compare the wet pressure drop performances between different structured packing geometries.

8.5 Effect of the viscosity on the effective area

The effect of the liquid viscosity is assessed varying the percentage of MEA in the liquid solution. Figure 8.6 presents the influence of the percentage of MEA on the effective area.

The graph shows a decreasing tendency. However, the influence of the liquid viscosity is not very important, with the biggest difference below 10% with the base case of pure water, i.e. viscosity equal to 1 cP. The difference between the MEA 30% wt. case and pure water is 1.5%.

Some controversy has been found in the literature regarding the influence of the viscosity on the effective area. Tsai et al. [118] concluded that the viscosity has practically no effect. Other authors found that the viscosity has a strong effect on the liquid hold-up, with a direct relationship [206]. Rizzuti et al [207] also observed a strong influence of the viscosity whereas Bradtmöller et al [198] reported that the effect is different depending on the type of liquid formation considered. As a conclusion, the tendency presented in this section is in agreement with the results reported by Tsai et al [118], which show a small effect of the viscosity on the interfacial area. The graph shows a decreasing tendency. According to the present results an increase in the MEA contents of the solution could

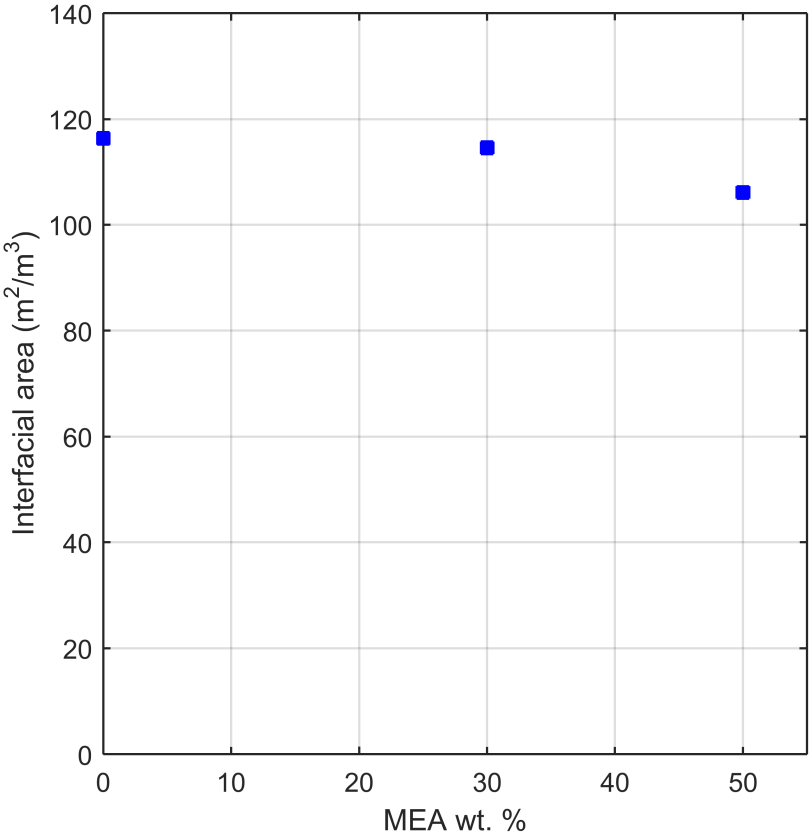

Figure 8.6: Effect of varying the MEA contents within the solution on the interfacial area. Stagnant air at atmospheric pressure as the gas phase. The MEA has a dynamic viscosity of 24 cP and a density of 1002 kg/m^3. The liquid load is 180 m/h.

be detrimental for the performance of the process. However, it has also been stated that increasing the amine contents causes a significant enhancement in the absorption rate.

8.6 Effect of the contact angle on the effective area

Figure 8.7 shows the effect of the contact angle on the variation of the effective area. The general tendency is that the effective area grows with lower values of the contact angle. The three cases examined are run with a liquid load of 180 m/h and a 30% wt.

MEA aqueous solution. The contact angles considered are 10°, 40°, and 70°, which cover different degrees of adhesion between the liquid phase and the structured packing walls.

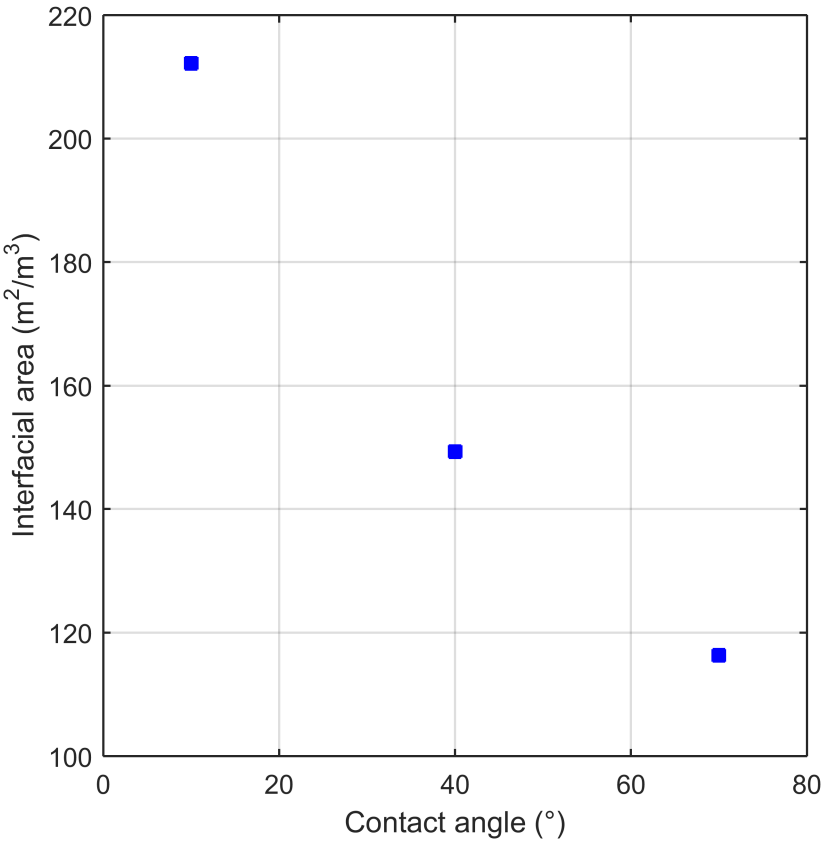

Figure 8.7: Effect of varying the contact angle on the interfacial area. Stagnant air at atmospheric pressure as the gas phase. 30% wt. MEA water as liquid phase. The liquid load is 180 m/h.

Low values of the contact angle mean better wetting conditions by virtue of the prevalence of the adhesion forces over cohesion. Moreover, the improvement in the wetting conditions can be considered as substantial since the result obtained with a contact angle of 10° doubles the interfacial area obtained with an angle of 70°. This tendency has already been reported in the literature [117, 208]. These results highlight the importance of a good choice of the material used to manufacture the structured packing since the con-

tact angle between the liquid and the solid is a function of both the properties of the liquid phase and the solid wall.

The analysis of the influence of the distortive and cohesive forces on the amount of wetted area has been usually presented in the literature using the Weber number, which takes into account the gravity and the surface tension [82]. The results presented in this section suggest that not only gravity plays an important role on the spreading of the liquid phase over the plate, but also the liquid-solid adhesion proves to have a similar effect, resulting in better wetting conditions as the contact angle diminishes.

8.7 Conclusions

The capabilities of meso-scale modelling have been extended to gain a more realistic treatment by including the tracking of the interface between the fluids. Therefore, other important parameters of the absorber performance, apart from the dry pressure drop, such as the liquid hold-up and the interfacial area have also been represented.

First, the transient development of the liquid flow inside the set of REUs is visualised by means of 3D isometric views and cross-sectional plots of the volume fraction. The images show the formation of irregularities on the liquid flow that lie far from the assumption of a perfectly formed falling liquid film, i.e. this assumption has been used in the literature to predict the wet pressure drop performance as a function of the liquid load. The flow development is characterised by a high importance of the capillarity effect at the initial time steps and at particular areas of the domain such as the contact points between the confronted packing sheets. An accumulation of liquid in the surroundings of the upper contact points happens in the beginning. The volume of the droplets in this area increases until the effect of gravity is important enough to cause the detachment of the droplets. Once detached, the liquid droplets impact on the surface of the packing causing a further

liquid break-up that results in a bigger number of droplets and rivulets. The formation of these irregularities is responsible of the fact that the actual interfacial area is greater than the specific area of the packing, which is considered as a beneficial effect.

The liquid hold-up, measured as the volume of liquid per unit volume of the packing has been correctly reproduced, with an increasing tendency as a function of the liquid load. The rate of change is greater for smaller liquid loads whereas it tends to be lower as the liquid load increases. The liquid hold-up is generally overpredicted with respect to the experiments from the literature. The interfacial area is the next aspect studied. The correct tendency is also reproduced. The results show a rapid increase at low values of the liquid load and an ulterior stabilisation.

The study of the influence of two important operating parameters such as the liquid viscosity, i.e. expressed as the MEA weight percentage within the liquid solution, and the contact angle has also been included. The influence of the viscosity has been observed to be small compared to that of the contact angle. The results reported in the literature about the influence of the viscosity have shown contradictory conclusions in this regard. The results presented in this chapter show that the viscosity has almost no influence on the amount of effective area, with a slight decreasing tendency. The contrary effect is obtained for the contact angle, which is proved to have a significant influence. The adhesion between the liquid and the solid wall of the packing acts in a similar way as gravity in the analysis of the wetted area as a function of the Weber number, i.e. helping the wetting process. Both types of forces, e.g. adhesion and gravity, have then the opposite effect to surface tension.

Consequently, this chapter presents a methodology to compare actual packing geometries in terms of liquid hold-up, interfacial area, pressure drop, and non-reactive mass transfer. Further work should be considered in order to implement the reaction kinetics of the CO_2 absorption process.

Chapter 9

Final remarks

This thesis deals with the development and application of a CFD model to the multiphase flow inside a structured packing reactor. The simulations are run with the commercial software ANSYS® Fluent v14.0, a general purpose commercial CFD code that includes the VOF method for interfacial tracking. Although being a general purpose code, it offers the possibility of expanding its capabilities by using UDFs, which are subroutines written in C language to account for other flow characteristics that do not come standard in the software. In the case of the present thesis, the UDF focuses on the implementation of the reactive mass transfer that takes place between the CO_2 and the aqueous MEA solution in a post-combustion CCS absorber.

9.1 Contributions to knowledge

The contributions to knowledge presented in this thesis are listed as follows:

1. The implementation of the mass source term in a single set of conservation equations applied to both the gas and the liquid phase results in the appearance of an extra source term in the momentum equation as seen in Chapter 3, wherein the gen-

eral conservation equation solved in the present model is derived. Analogously to what is observed in any variable mass system, the equation shows two acceleration terms: one is caused by the velocity variation and the other by the mass variation. This constitutes the main contribution of the thesis at the theoretical level.

2. As observed, there is a lack of grid convergence studies in multiphase CFD simulations. A grid convergence study based on the Richardson extrapolation is presented in this work with a double focus. On the one hand, the search for an optimum grid resolution for this application, which helps tackling the problem that this calculations are computationally expensive. On the other hand, the lack of experimental data to which compare the CFD simulations gives rise to the necessity of proving the reliability of the present work.

3. At the level of results, the capabilities of the three scales in which the modelling is divided are expanded in this work. More final remarks regarding this aspect are discussed in the following section 9.2.

9.2 Summary of modelling results

The modelling of CCS post-combustion absorbers is divided into three different scales: small-, meso- and large-scale. The division of the modelling in scales has been reported in the literature and responds to the fact that it is not possible to carry out a complete CFD study of all the aspects involved in the multiphase flow with the current computational capacity available.

In this work, the main contribution at small-scale is that the interface tracking method has been implemented in 3D domains, along with the absorption mass transfer with and without chemical reaction.

The advantage of combining the mass transfer source terms with the interface tracking method in 3D domains is the possibility of studying the influence of the liquid load, hence the liquid maldistribution, on the interfacial area available and the mass transfer performance. The results on hydrodynamics show the formation of three different regimes: tricking, rivulet and full film flow, depending on the balance between gravity and surface tension (the Weber number) for the case of pure water. The general conclusion is that the interfacial area between both phases increases with the liquid load. The three aforementioned regimes are consecutively formed as the liquid load increases. The results show that the mass transfer is highly influenced by the interfacial area. Generally, the more interfacial area is available, the better the mass transfer. However, the results also show that once the full film flow is achieved, increasing the liquid flow rate has a detrimental effect on the mass absorption rate caused by the reduction on the exposure time. Therefore, the relationship between the mass absorption rate and the liquid load leads to a maximum.

The non-reactive model, i.e. oxygen-water system, is further used to investigate the effect of several operating parameters on the absorption performance. Gas pressure and velocity, contact angles, flow configuration and amine contents are assessed.

An increase in the amine percentage within the solution proves to hinder the absorption process through its influence on the diffusivity. This tendency is reversed for the case of reactive mass transfer. Gas pressure has a beneficial impact on the absorption process due to its effect on solubility. Gas pressure affects the solubility through Henry's law. Therefore, an increase in the solubility means a higher concentration gradient between the gas-liquid interface and the liquid bulk, which in turn results in an enhanced mass transfer rate. Gas velocity and flow configuration also affect the interfacial area available for mass transfer. Both co- and counter-current configurations present a better absorption performance if compared to the case of stagnant gas phase, being the co-current the most advantageous case. Co-current flow tends to spread the liquid film over the packing,

which results in better wetting conditions. Counter-current tends to hold the liquid within the domain, which translates in more exposure time. Increasing the gas velocity also shows a beneficial impact. The contact angle results from the balance between adhesion and cohesion forces. Better adhesion conditions result in an enhanced liquid spreading over the plate. In this way, adhesion behaves in the same manner as gravity in the analysis of the wetted area as a function of the Weber number. The effect of adhesion forces highlights the importance of a good selection of the material with which the structured packing is manufactured.

The hydrodynamics of the MEA solutions are also described, showing important differences with respect to the case of pure water due to the difference in viscosity. Instead of one of the three afore-mentioned liquid regimes, the amine tends to reach always the full film flow but at a slower pace. In short, for the liquid loads tested, pure water does not cover the entire liquid plate whereas the amine solutions reach this condition. Also, for low liquid loads, the amine forms rivulets instead of a fully covered plate but still the wetted area is bigger than for pure water. The slow development of amine liquid films, with respect to pure water films, is explained by the lower velocities observed. Also, thicker films have been observed in the amines, which also mean higher liquid hold-up hence more pressure losses through the column.

Later, the UDF code is extended to also include the source terms to describe the variation on the mass fraction of both the reactants and the products of the reaction between the CO_2 and the MEA solution.

The model reproduces the fact that the chemical reaction takes place only at the gas-liquid interface. The CO_2 concentration profiles show that the concentration decreases from a maximum value at the interface to zero in 0.1 mm, i.e. the liquid film thickness is approximately 0.7 mm, depending on its amine contents. In order to compare the effect of the mass source terms describing the consumption/creation of reactants/products within

the amine solution, the CO_2 concentration has also been obtained disabling the source terms associated to the presence of the chemical reaction. By doing so, a value of the CO_2 concentration different from zero can be found in the entire thickness of the liquid film. Also, the concentration profiles of the rest of the species involved in the reaction, i.e. hydronium and carbamate, are presented. The concentration profiles of the reaction products show the expected shape for the diffusion process. The study of the variation of the enhancement factor with the amine contents follows. The results show an increasing tendency of the absorption gain with the MEA concentration for the reactive absorption case. This result leads to the conclusion that a high amine concentration is preferable.

At meso-scale the main innovation presented in this work is the implementation of the interfacial tracking, i.e. VOF method, in sections of the structured packing material. This allows studying important flow characteristics such as liquid hold-up and interfacial area as well as the formation of liquid irregularities within the flow that have already been detected with experimental methods. Although some attempts have been reported in the literature at the time of submitting this thesis, liquid hold-up, interfacial area and, in general the study of the liquid maldistribution phenomenon have been restricted to simulations at small-scale. Therefore, the application of interface tracking methods should be extended to meso-scale in order to represent liquid hold-up and interfacial area.

The results show that both liquid hold-up and interfacial area are well reproduced by the model, showing a direct relationship with the liquid load that was expected in the light of previous experimental work and small-scale simulations. The tendency shows a rapid increase of both characteristics for low values of the liquid load, with a subsequent stabilisation. It is shown that the formation of a perfectly developed liquid film over the walls of the structured packing does not occur. However, this assumption has been used in the literature to obtain the wet pressure drop performance of the packing.

Later on, the dry pressure drop of the MontzPak B1-250M is obtained and compared

to experimental work published in the literature. Subsequently, instead of assuming the perfectly developed liquid film over the packing, the wet pressure drop is obtained using the liquid hold-up calculated obtained with the present model.

9.3 Future work

The future work should focus on further expanding the capabilities of the different modelling scales in order to get closer to an integral simulation method able to describe all the characteristics of the multiphase flow within a structured packing column. In particular, the reactive mass transfer modelling lacks a denser mesh in the interface, which would bring more accurate results. The implementation of an adaptive mesh refinement method could better describe the concentration gradients taking place in this area.

Finally, the possibility of coupling both CFD and process simulations is discussed in the introduction. This approach would provide an integral insight on the behaviour of a CCS post-combustion facility, allowing to check how the variation of any of the parameters at any of the CFD scales could affect the other pieces of equipment in the facility.

Appendix A

User-defined function

/* This UDF calculates physical mass transfer of CO2 from the gas phase to the liquid phase and accounts for the reactive system: finite-rate chemical reactions: CO2 + OH- <–> HCO3- CO2 + MEA + H2O <–> H3O+ */

```
# include "udf.h"
# include "mem.h"
# include "math.h"
# include "metric.h"
# include "sg.h"
# define solubility 1.064445e-03
/* N2O analogy Sema and Penttila */
# define diffusivity 0.405e-09
# define pi 3.1416
/*This part of the code was developed to calculate the effective area as the modulus of the gradient of the volume fraction*/
DEFINE_ ADJUST(myadjust,d)
{
```

```
if(ROOT_ DOMAIN_ P(d))
{
cell_t c;
Thread *t;
Domain *sd = DOMAIN_ SUB_ DOMAIN(d,1);
Alloc_ Storage_ Vars(sd,SV_ VOF_ RG,SV_ VOF_ G,SV_ NULL);
Scalar_ Reconstruction(sd, SV_ VOF,-1,SV_ VOF_ RG,NULL);
Scalar_ Derivatives(sd,SV_ VOF,- 1,SV_ VOF_ G,SV_ VOF_ RG,& Vof_ Deriv_
Accumulate);
thread_ loop_ c(t,d)
if(FLUID_ THREAD_ P(t))
{
Thread *pt = THREAD_ SUB_ THREAD(t,1);
begin_ c_ loop(c,t)
{
C_ UDMI(c,t,5) = NV_ MAG(C_ VOF_ G(c,pt));
}
end_ c_ loop(c,t)
}
Free_ Storage_ Vars(sd,SV_ VOF_ RG,SV_ VOF_ G,SV_ NULL);
}
}
/*This part of the code calculates the source terms that describe the non-reactive ab-
sorption through the interface*/
DEFINE_ LINEARIZED_ MASS_ TRANSFER(mass_ transfer_ udf, c, mixture_
thread, from_ phase_ index, from_ species_ index, to_ phase_ index, to_ species_ index,
```

```
lin_ from, lin_ to)
    {
    Thread  gas = THREAD_ SUB_ THREAD(mixture_ thread, from_ phase_ index);
    Thread  liq = THREAD_ SUB_ THREAD(mixture_ thread, to_ phase_ index);
    enum UDMI_ indexi1, i2, i3, i4, i5, i6, i7, i8, i9, i10, i11, i12, i13;
    double mass_ weight[5] = 18., 44., 61., 19., 61.;
    int i;
    real cell_ pos[3];
    real mass_ source = 0., eff_ area = 0., coeff = 0., tot_ con = 0., Sherwood = 0., vel_
mol = 0., exp_ time;
    real onee;
    real rate, kfor, keq, ci_ reac, ci_ prod, sourceh2o, sourceco2, sourcemea, sourceh3o,
sourcezwitterion, hatta_ sq, enhancement, MEAcon, solute_ mol_ weight, av_ mol_ mass,
sum, tot_ con_ 2;
    mass_ source = 0.;
    sourceh2o = 0.;
    sourceco2 = 0.;
    sourcemea = 0.;
    sourceh3o = 0.;
    sourcezwitterion = 0.;
    hatta_ sq = 0.;
    MEAcon = 0.;
    enhancement = 0.;
    solute_ mol_ weight = 0.;
    av_ mol_ mass = 0.;
    sum = 0.;
```

```
tot_ con_ 2 = 0.;
if (CURRENT_ TIME > 0.)
{
if (( C_ VOF(c, liq) < 1.0) & & (C_ VOF(c, liq) >0))
{ real mag = C_ UDMI(c,mixture_ thread,5);
C_ CENTROID(cell_ pos, c, mixture_ thread);
eff_ area = mag;
vel_ mol = pow((pow(C_ U(c, liq), 2) + pow(C_ V(c, liq), 2) + pow(C_ W(c, liq), 2)), 0.5);
exp_ time = (0.1-(cell_ pos[1])) / vel_ mol;
coeff= 2 * pow(diffusivity/pi/exp_ time, 0.5);
/* This is the total concentration of components in the liquid phase in kmol m-3 */
tot_ con= (C_ YI(c, liq, 0) * 1002 / mass_ weight[0]) + (C_YI(c, liq, to_ species_ index) * 1002 / mass_ weight[1]) + (C_ YI(c, liq, 2) * 1002 / mass_ weight[2]) + (C_ YI(c, liq, 3) * 1002 / mass_ weight[3]) + (C_ YI(c, liq, 4) * 1002 / mass_ weight[4]);
MEAcon = C_ YI(c, liq, 2) * 1002 / mass_ weight[2];
sum = (C_ YI(c, liq, 0) / mass_ weight[0]) + (C_ YI(c, liq, to_ species_ index) / mass_ weight[1]) + (C_ YI(c, liq, 2) / mass_ weight[2]) + (C_ YI(c, liq, 3) / mass_ weight[3]) + (C_ YI(c, liq, 4) / mass_ weight[4]);
av_ mol_ mass = 1 / sum; solute_ mol_ weight = mass_ weight[1];
hatta_ sq = 24984*diffusivity*MEAcon/coeff/coeff; enhancement = pow(hatta_ sq + 1, 0.5);
tot_ con_ 2 = solute_ mol_ weight * tot_ con;
mass_ source = enhancement  coeff  eff_ area  tot_ con_ 2  (solubility - C_ YI(c, liq, to_ species_ index))  av_ mol_ mass / mass_ weight[1];
Sherwood = coeff cell_ pos[0] / diffusivity;
```

```
} if ((C_ VOF(c, liq) <= 1.0) & & (C_ VOF(c, liq) >0))
{
ci_ reac = pow(C_ R(c, mixture_ thread), 2)  C_ YI(c, liq, 2)  C_ YI(c, liq, to_ species_ index) / mass_ weight[to_ species_ index] / mass_ weight[2];
/* Littel take into account the concentration of MEA and CO2 */
ci_ prod = pow(C_ R(c, mixture_ thread), 2) * C_ YI(c, liq, 3) * C_ YI(c, liq, 4) / mass_ weight[3] / mass_ weight[4];
keq = 0.000118;
kfor = 24984; /* m3 kmol-1 s-1 from Kale et al. 2013 */
rate = kfor  ci_ reac; / -(kfor / keq)  ci_ prod;  /
if (C_ YI(c, liq, 0) >= 0.) /* The species with index 0 is water liquid */
{
sourceh2o = -rate * mass_ weight[0]; } else
{
sourceh2o = 0.;
}
if (C_ YI(c, liq, to_ species_ index) >=0.)  sourceco2 = -rate * mass_ weight[to_ species_ index];  else  sourceco2 = 0.;
if (C_ YI(c, liq, 2) >=0.)  sourcemea = -rate * mass_ weight[2];  else  sourcemea = 0.;
if (C_ YI(c, liq, 3) >=0.)  sourceh3o = rate * mass_ weight[3];  else  sourceh3o = 0.;
if (C_ YI(c, liq, 4) >=0.)  sourcezwitterion = rate * mass_ weight[4]; }
else
{
sourcezwitterion = 0.;
}
```

```
}
}
C_ UDMI(c, mixture_ thread, i1) = eff_ area;
C_ UDMI(c, mixture_ thread, i2) = coeff;
C_ UDMI(c, mixture_ thread, i3) = tot_ con_ 2;
C_ UDMI(c, mixture_ thread, i4) = mass_ source;
C_ UDMI(c, mixture_ thread, i5) = Sherwood; C_ UDMI(c, mixture_ thread, i7) =
sourceh2o;
C_ UDMI(c, mixture_ thread, i8) = sourceco2;
C_ UDMI(c, mixture_ thread, i9) = sourcemea;
C_ UDMI(c, mixture_ thread, i10) = sourceh3o;
C_ UDMI(c, mixture_ thread, i11) = sourcezwitterion;
C_ UDMI(c, mixture_ thread, i12) = rate;
C_ UDMI(c, mixture_ thread, i13) = enhancement;
return mass_ source;
}
/*This part of the code represents a velocity profile*/
DEFINE_ PROFILE(velocity,t,i)
real y; real x[ND_ ND]; face_ t f;
begin_ f_ loop(f,t)  F_ CENTROID(x,f,t); y=x[1]; F_ PROFILE(f,t,i) = -27510 ×
pow(y,2) + 146 * y + 0.326;  end_ f_ loop(f,t)
/*This part of the code presents the mass source terms that describe the consump-
tion/creation of reactants/products*/
DEFINE_ SOURCE(water_ liquid, c, mixture_ thread, dS, eqn)  return C_ UDMI(c,
mixture_ thread, 6);
```

DEFINE_ SOURCE(carbon_ dioxide, c, mixture_ thread, dS, eqn) return C_ UDMI(c, mixture_ thread, 7);

DEFINE_ SOURCE(mea, c, mixture_ thread, dS, eqn) return C_ UDMI(c, mixture_ thread, 8);

DEFINE_ SOURCE(hydronium, c, mixture_ thread, dS, eqn) return C_ UDMI(c, mixture_ thread, 9);

DEFINE_ SOURCE(zwitterion, c, mixture_ thread, dS, eqn) return C_ UDMI(c, mixture_ thread, 10);

References

[1] Sorrell, S. 2015. Reducing energy demand: A review of issues, challenges and approaches. *Renewable and Sustainable Energy Reviews*, 47, pp. 74–82.

[2] Wennersten, S., Sun, Q. and Li, H. 2015. The future potential for Carbon Capture and Storage in climate change mitigation – an overview from perspectives of technology, economy and risk. *Journal of Cleaner Production*, 103, pp. 724–736.

[3] Khalilpour, R. 2014. Multi-level investment planning and scheduling under electricity and carbon market dynamics: Retrofit of a power plant with PCC (post-combustion carbon capture) processes. *Energy*, 64, pp. 172–186.

[4] van den Broek, M., Berghout, N. and Rubin, E.S. 2015. The potential of renewables versus natural gas with CO_2 capture and storage for power generation under CO_2 constraints. *Renewable and Sustainable Energy Reviews*, 49, pp. 1296–1322.

[5] Viebahn, P., Daniel, V. and Höller, S. 2012. Integrated assessment of carbon capture and storage (CCS) in the German power sector and comparison with the deployment of renewable energies. *Applied Energy*, 97, pp. 238–248.

[6] MacDowell, N., Florin, N., Buchard, A., Hallett, J., Galindo, A., Jackson, G., Adjiman, C.S., Williams, C.K., Shah, N. and Fennell, P. 2010. An overview of CO_2 capture technologies. *Energy and Environmental Science*, 3, pp. 1645–1669.

[7] Figueroa, J.D., Fout, T., Plasynski, S., McIlvried, H. and Srivastava, R.D. 2008. Advances in CO_2 capture technology – The U.S. Department of Energy's carbon sequestration program. *International Journal of Greenhouse Gas Control*, 2, pp. 9–20.

[8] Houghton, J.T., Ding, Y., Griggs, D.J, Noguer, M., van der Linden, P.J., Dai, X., Maskell, K. and Johnson, C.A. 2001. *Climate Change 2001: The scientific basis*. Cambridge: Cambridge University Press.

[9] Hofmann, D.J., Butler, J.H. and Tans, P.P. 2009. A new look at atmospheric carbon dioxide. *Atmospheric Environment*, 43, pp. 2084–2086.

[10] Odenberger, M. and Johnson, F. 2010. Pathways for the European electricity supply system to 2050 – The role of CCS to meet stringent CO_2 reduction targets. *International Journal of Greenhouse Gas Control*, 4, pp. 327–340.

[11] Chakroun, N.W. and Ghoniem, A.F. 2015. Techno-economic assessment of sour gas oxy-combustion water cycles for CO_2 capture. *International Journal of Greenhouse Gas Control*, 36, pp. 1–12.

[12] Fagerlund, F. Niemi, A., Bensabat, J. and Shtivelman, V. 2013. Design of a two-well field test to determine in situ residual and dissolution trapping of CO_2 applied to the Heletz CO_2 injection site. *International Journal of Greenhouse Gas Control*, 19, pp. 642–651.

[13] Fagerlund, F. Niemi, A., Bensabat, J. and Shtivelman, V. 2013. Interwell field test to determine in-situ CO_2 trapping in a deep saline aquifer: Modelling study of the effects of test design and geological parameters. *Energy Procedia*, 40, pp. 554–563.

[14] Rasmusson, K. Rasmusson, M., Fagerlund, F. Bensabat, J, Tsang, Y. and Niemi, A. 2014. Analysis of alternative push-pull-test-designs for determining in situ residual trapping of carbon dioxide. *International Journal of Greenhouse Gas Control*, 27, pp. 155–168.

[15] Yu, W. Lashgari, H.R., Wu, K. and Sepehrnoori, K. 2015. CO_2 injection for enhanced oil recovery in Bakken tight oil reservoirs. *Fuel*, 159, pp. 354–363.

[16] Wang, X., Alvarado, V., Swoboda-Colberg, N. and Kaszuba, J.P. 2013. Reactivity of dolomite in water-saturated supercritical carbon dioxide: Significance for carbon capture and storage and for enhanced oil and gas recovery. *Energy Conversion and Management*, 65, pp. 564–573.

[17] Farhat, K., Koplin, J., Lewis, D., Peterlin, S. and Simms, R. 2013. Financial assessment of CO_2 capture and storage with electricity trading in the U.S.: Role of interim storage and enhanced oil recovery. *Energy Procedia*, 37, pp. 7512–7525.

[18] Azzolina, N.A., Nakles, D.V., Gorecki, C.D., Peck, W.D., Ayash, S.C., Melzer, L.S., and Chatterjee, S. 2015. CO_2 storage associated with CO_2 enhanced oil recovery: A statistical analysis of historical operations. *International Journal of Greenhouse Gas Control*, 37, pp. 384–397.

[19] Karegar, M.A., Dixon, T.H., Malservisi, R., Yang, Q., Hossaini, S.A. and Hovorka, S.D. 2015. GPS-based monitoring of surface deformation associated with CO_2 injection at an enhanced oil recovery site. *International Journal of Greenhouse Gas Control*, 41, pp. 116–126.

[20] Boodlal, D. and Alexander, D. 2014. The impact of the clean development mechanism and enhanced oil recovery on the economics of carbon capture and geological storage for Trinidad and Tobago. *Energy Procedia*, 63, pp. 6420–6427.

[21] Soltanieh, M. Eslami, A.M. and Moradian, A. 2009. Feasibility study of carbon dioxide capture from power plants and other major stationary sources and storage in iranian oil fields for enhanced oil recovery (EOR). *Energy Procedia*, 1, pp. 3663–3668.

[22] Liang, W., Rongwong, W., Liu, H., Fu, K., Gao, H., Cao, F., Zhang, R., Sema, T., Henni, A., Sumon, K., Nath, D., Gelowitz, D., Srisang, W., Saiwan, C., Benamor, A., Al-Marri, M., Shi, H., Supap, T., Chan, C., Zhou, Q., Abu-Zahra, M., Wilson, M., Olson, W., Idem, R. and Tontiwachwuthikul, P. 2015. Recent progress and new developments in post-combustion carbon-capture technology with amine based solvents. *International Journal of Greenhouse Gas Control*, 40, pp. 26–54.

[23] Sreenivasulu, B., Gayatri, D.V., Sreedhar, I. and Raghavan, K.V. 2015. A journey into the process and engineering aspects of carbon capture technologies. *Renewable and Sustainable Energy Reviews*, 41, pp. 1324–1350.

[24] Razi, N., Bolland, O. and Svendsen, H. 2012. Review of design correlations for CO_2 absorption into MEa using structured packings. *International Journal of Greenhouse Gas Control*, 9, pp. 193–219.

[25] Babu, P., Linga, P., Kumar, R. and Englezos, P. 2015. A review of the hydrate based gas separation (HBGS) process for carbon dioxide pre-combustion capture. *Energy*, 85, pp. 261–279.

[26] Jansen, D., Gazzani, M., Manzolini, G., van Dijk, E. and Carbo, M. 2015. Pre-combustion CO_2 capture. *International Journal of Greenhouse Gas Control*, 40, pp. 167–187.

[27] Franz, J., Maas, P. and Scherer, V. 2014. Economic evaluation of pre-combustion CO_2-capture in IGCC power plants by porous ceramic membranes. *Applied Energy*, 130, pp. 532–542.

[28] Trapp, C., de Servi, C., Casella, F., Bardow, A. and Colonna, P. 2015. Dynamic modelling and validation of pre-combustion CO_2 absorption based on a pilot plant at the Buggenum IGCC power station. *International Journal of Greenhouse Gas Control*, 36, pp. 13–26.

[29] Babu, P., Kumar, R. and Linga, P. 2013. Pre-combustion capture of carbon dioxide in a fixed bed reactor using the clathrate hydrate process. *Energy*, 50, pp. 364–373.

[30] Koiwanit, J., Manuilova, A. Chan, C., Wilson, M. and Tontiwachwuthikul, P. 2014. A life cycle assessment study of a hypothetical Canadian oxy-fuel combustion carbon dioxide capture process. *International Journal of Greenhouse Gas*, 28, pp. 257–274.

[31] Gładysz, P. and Ziębik, A. 2015. Life cycle assessment of an integrated oxy-fuel combustion power plant with CO_2 capture, transport and storage – Poland case study. *Energy*, 92, pp. 328–340.

[32] Aneke, M. and Wang, M. 2015. Process analysis of pressurized oxy-coal power cycle for carbon capture application integrated with liquid air power generation and binary cycle engines. *Applied Energy*, 154, pp. 556–566.

[33] García-Gusano, D. Garraín, D., Herrera, I., Cabal, H. and Lechón, Y. 2015. Life cycle assessment of applying CO_2 post-combustion capture to the Spanish cement production. *Journal of Cleaner Production*, 104, pp. 328–338.

[34] Rabensteiner, M. Kinger, G., Koller, M., Gronald, G. and Hochenauer, C. 2015. Investigation of carbon dioxide capture with aqueous piperazine on a postcombustion pilot plant – Part I: Energetic review of the process. *International Journal of Greenhouse Gas Control*, 39, pp. 79–90.

[35] Rabensteiner, M. Kinger, G., Koller, M., Gronald, G. and Hochenauer, C. 2015. Investigation of carbon dioxide capture with aqueous piperazine on a postcombustion pilot plant – Part II: Parameter study and emission measurement. *International Journal of Greenhouse Gas Control*, 37, pp. 471–480.

[36] Zhu, L. Jiang, P. and Fan, J. 2015. Comparison of carbon capture IGCC with chemical-looping combustion and with calcium-looping process driven by coal for power generator. *Chemical Engineering Research and Design*, 104, pp. 110–124.

[37] Reynolds, A.J., Verheyen, T.V., Adeloju, S.B., Chaffee, A.L. and Meuleman, E. 2015. Evaluation of methods for monitoring MEA degradation during pilot scale post-combustion capture of CO_2. *International Journal of Greenhouse Gas Control*, 39, pp. 407–419.

[38] Brinkmann, T., Pohlmann, J., Bram, M., Zhao, L., Tota, A., Jordan Escalona, N., de Graaff, M. and Stolten, D. 2015. Investigating the influence of the pressure distribution in a membrane module on the cascaded membrane system for post-combustion capture. *International Journal of Greenhouse Gas Control*, 39, pp. 194–204.

[39] Zhao, S., Feron, P.H.M., Cao, C., Wardhaugh, L., Yan, S. and Gray, S. 2015. Membrane evaporation of amine solution for energy saving in post-combustion carbon capture: Wetting and condensation. *Separation and Purification Technology*, 146, pp. 60–67.

[40] Zhao, S., Cao, C., Wardhaugh, L., and Feron, P.H.M. 2015. Membrane evaporation of amine solution for energy saving in post-combustion carbon capture: Performance evaluation. *Journal of Membrane Science*, 473, pp. 274–282.

[41] Rezazadeh, F., Gale, W.F., Hugues, K.J., and Poukashanian, M. 2015. Performance viability of a natural gas fired combined cycle power plant integrated with post-combustion CO_2 capture at part-load and temporary non-capture operations. *International Journal of Greenhouse Gas Control*, 39, pp. 397–406.

[42] Luu, M.T., Manaf, N.A., and Abbas, A. 2015. Dynamic modelling and control strategies for flexible operation of amine-based post-combustion CO_2 capture systems. *International Journal of Greenhouse Gas Control*, 39, pp. 377–389.

[43] Wang, M., Lawal, A., Stephenson, P., Sidders, J. and Ramshaw, C. 2011. Post-combustion CO_2 capture with chemical absorption: A state-of-the-art review. *Chemical Engineering Research and Design*, 89, pp. 1609–1624.

[44] Wang, N., Mundstock, A., Liu, Y., Huang, A. and Caro, J. 2015. Amine-modified Mg-MOF-74/CPO-27-Mg membrane with enhanced H_2/CO_2 separation. *Chemical Engineering Research and Design*, 124, pp. 27–36.

[45] Li, J.R, Ma, Y., McCarthy, M.C., Sculley, J., Yu, J., Jeong, H.K., Balbuena, P.B. and Zhou, H.C. 2011. Carbon dioxide capture-related gas adsorption and separation in metal-organic frameworks. *Coordination Chemistry Reviews*, 255, pp. 1791–1823.

[46] Casas, N., Schell, J., Blom, R. and Mazzotti, M. 2013. MOF and UiO-67/MCM-41 adsorbents for pre-combustion CO_2 capture by PSA: Breakthrough experiments and process design. *Separation and Purification Technology*, 112, pp. 34–48.

[47] Adatoz, E., Avci, A.K. and Keskin, S. 2015. Opportunities and challenges of MOF-based membranes in gas separations. *Separation and Purification Technology*, 152, pp. 207–237.

[48] Hu, Z., Khurana, M., Seah, Y.H., Zhang, M., Guo, Z. and Zhao, D. 2015. Ionized Zr-MOFs for highly efficient post-combustion CO_2 capture. *Chemical Engineering Science*, 124, pp. 61–69.

[49] Yang, J., Wang, Y., Li, L., Zhang, Z. and Li, J. 2015. Protection of open-metal V(III) sites and their associated $CO_2/CH_4/N_2/O_2/H_2O$ adsorption properties in mesoporous V-MOFs. *Journal of colloid and Interface Science*, 456, pp. 197–205.

[50] Rochelle, G.T. 2009. Amine scrubbing for CO_2 capture. *Science*, 325, pp. 1652–1654.

[51] Biliyok, C. and Yeung, H. 2013. Evaluation of natural gas combined cycle power plant for post-combustion CO_2 capture integration. *International Journal of Greenhouse Gas Control*, 19, pp. 396–405.

[52] Yang, W., Yu, X., Mi, J., Wang, W. and Chen, J. 2015. Mass transfer performance of structured packings in a CO_2 absorption tower. *Chinese Journal of Chemical Engineering*, 23, pp. 42–49.

[53] Mores, P., Rodríguez, N., Scenna, N. and Mussati, S. 2012. CO_2 capture in power plants: Minimization of the investment and operating cost of the post-combustion process using MEA aqueous solution. *International Journal of Greenhouse Gas Control*, 10, pp. 148–163.

[54] Raynal, L., Bouillon, P.A., Gomez, A. and Broutin, P. 2011. From MEA to demixing solvents and future steps, a roadmap for lowering the cost of post-combustion carbon capture. *Chemical Engineering Journal*, 171, pp. 742–752.

[55] Manuilova, A., Koiwanit, J., Piewkhaow, L., Wilson, M., Chan, C.W. and Tontiwachwuthikul, P. 2014. Life cycle assessment of post-combustion CO_2 capture and CO_2-enhanced oil recovery based on the Boundary Dam Integrated Carbon Capture and Storage Demonstration Project in Saskatchewan. *Energy Procedia*, 63, pp. 7398–7407.

[56] Stéphenne, K. 2014. Start-up of world's first commercial post-combustion coal fired CCS project: Contribution of Shell Cansolv to SaskPower Boundary Dam ICCS Project. *Energy Procedia*, 63, pp. 6106–6110.

[57] Mitrović, M. and Malone, A. 2011. Carbon Capture and Storage (CCS) demonstration projects in Canada. *Energy Procedia*, 4, pp. 5685–5691.

[58] Idem, R., Supap, T., Shi, H., Gelowitz, D., Ball, M., Campbell, C. and Tontiwachwuthikul, P. 2015. Practical experience in post-combustion CO_2 capture using reactive solvents in large pilot and demonstration plants. *International Journal of Greenhouse Gas Control*, 40, pp. 6–25.

[59] Raynal, L. and Royon-Lebeaud, A. 2007. A multi-scale approach for CFD calculations of gas-liquid flow within large size column equipped with structured packing. *Chemical Engineering Science*, 62, pp. 7196–7204.

[60] Sun, B., He, L., Liu, B.T., Gu, F. and Liu, C.J. 2013. A new multi-scale model based on CFD and macroscopic calculation for corrugated structured packing column. *AIChE Journal*, 59, pp. 3119–3130.

[61] ANSYS Inc. 2013. *ANSYS Fluent Theory Guide*.

[62] Hirt, C. and Nichols, B. 1981. Volume of fluid (VOF) method for the dynamics of free boundaries. *Journal of Computational Physics*, 39, pp. 201–225.

[63] Ali, U., Best, T., Finney, K.N., Palma, C.F., Hugues, K.J., Ingham, D.B., and Pourkashanian, M. 2014. Process simulation and thermodynamic analysis of a micro turbine with post-combustion CO_2 capture and exhaust gas recirculation. *Energy Procedia*, 63, pp. 986–996.

[64] Biliyok, C., Lawal, A., Wang, M. and Seibert, F. 2012. Dynamic modelling, validation and analysis of post-combustion chemical absorption CO_2 capture plant. *International Journal of Greenhouse Gas Control*, 9, pp. 428–445.

[65] Kapetaki, Z., Brandani, P., Brandani, S. and Ahn, S. 2015. Process simulation of a dual-stage Selexol process for 95% carbon capture efficiency at an integrated gasification combined cycle power plant. *International Journal of Greenhouse Gas Control*, 39, pp. 17–26.

[66] Llano-Restrepo, M. and Araujo-Lopez, E. 2015. Modeling and simulation of packed-bed absorbers for post-combustion capture of carbon dioxide by reactive absorption in aqueous monoethanolamine solutions. *International Journal of Greenhouse Gas Control*, 42, pp. 258–287.

[67] Liu, X., Chen, J., Luo, X., Wang, M. and Meng, H. 2015. Study on heat integration of supercritical coal-fired power plant with post-combustion CO_2 capture process through process simulations. *Fuel*, 158, pp. 625–633.

[68] Ahn, H., Luberti, M., Liu, Z. and Brandani, S. 2013. Process simulation of aqueous MEA plants for post-combustion capture from coal-fired power plants. *Energy Procedia*, 37, pp. 1523–1531.

[69] Hanak, D.P., Biliyok, C., Yeung, H. and Białecki, R. 2014. Heat integration and exergy analysis for a supercritical high-ash coal-fired power plant integrated with a post-combustion carbon capture process. *Fuel*, 134, pp. 126–139.

[70] Hanak, D.P., Biliyok, C. and Manovic, V. 2015. Efficiency improvements for the coal-fired power plant retrofit with CO_2 capture plant using chilled ammonia process. *Applied Energy*, 151, pp. 258–272.

[71] Hanak, D.P., Biliyok, C. and Manovic, V. 2015. Rate-based model development, validation and analysis of chilled ammonia process as an alternative CO_2 capture technology for coal-fired power plants. *International Journal of Greenhouse Gas Control*, 34, pp. 52–62.

[72] Hanak, D.P., Kolios, A., Biliyok, C. and Manovic, V. 2015. Probabilistic performance assessment of a coal-fired power plant. *Applied Energy*, 139, pp. 350–364.

[73] Min, J.K. and Park, I.S. 2011. Numerical study for laminar wavy motions of liquid film flow on vertical wall. *International Journal of Heat and Mass Transfer*, 54, pp. 3256–3266.

[74] Valluri, P., Matar, O.K., Hewitt, G.F. and Mendes, M.A. 2005. Thin film flow over structured packings at moderate Reynolds numbers. *Chemical Engineering Science*, 60, pp. 1965–1975.

[75] Wehinger, G.D., Peeters, J., Muzaferija, S., Eppinger, T. and Kraume, M. 2013. Numerical simulation of vertical liquid-film dynamics. *Chemical Engineering Science*, 104, pp. 934–944.

[76] Luo, Y., Yang, H. and Lu, L. 2014. CFD simulation of the liquid flow on structured packing in the liquid desiccant dehumidifier. *Energy Procedia*, 61, pp. 180–183.

[77] Luo, S., Li, H., Fei, W. and Wang, Y. 2009. Liquid film characteristics on surface of structured packing. *Chinese Journal of Chemical Engineering*, 17, pp. 47–52.

[78] Subramanian, K., Paschke, S., Repke, J.U. and Wozny, G. 2009. Drag modelling in CFD simulation to gain insight of packed columns. *AIDIC Conference Series*, 9, pp. 299–308.

[79] Kohrt, M., Ausner, I., Wozny, G. and Repke, J.U. 2011. Texture influence on liquid-side mass transfer. *Chemical Engineering Research and Design*, 89, pp. 1405–1413.

[80] Zakeri, A., Einbu, A. and Svendsen, H.F. 2012. Experimental investigation of liquid holdup in structured packings. *Chemical Engineering Research and Design*, 90, pp. 585–590.

[81] Zhang, X., Yao, L., Qiu, L. and Zhang, X. 2013. Three-dimensional computational fluid dynamics modeling of two-phase flow in a structured packing column. *Chinese Journal of Chemical Engineering*, 21, pp. 959–966.

[82] Iso, Y., Huang, J., Kato, M., Matsuno, S. and Takano, K. 2013. Numerical and experimental study on liquid film flows on packing elements in absorbers for post-combustion CO_2 capture. *Energy Procedia*, 37, pp. 860–868.

[83] Fourati, M., Roig, V. and Raynal, L. 2012. Experimental study of liquid spreading in structured packings. *Chemical Engineering Science*, 80, pp. 1–15.

[84] Janzen, A., Steube, J., Aferka, S., Kenig, E.Y., Crine, M., Marchot, P. and Toye, D. 2013. Investigation of liquid flow morphology inside a structured packing using X-ray tomography. *Chemical Engineering Science*, 102, pp. 451–460.

[85] Alix, P. and Raynal, L. 2008. Liquid distribution and liquid hold-up in modern high capacity packings. *Chemical Engineering Research and Design*, 86, pp. 585–591.

[86] Suess, P. and Spiegel, L. 1992. Hold-up of mellapak structured packings. *Chemical Engineering and Processing: Process Intensification*, 31, pp. 119–124.

[87] Basden, M., Eldridge, R.B., Farone, J., Feng, E., Hussey, D.S. and Jacobson, D.L. 2013. Liquid hold-up profiles in structured packing determined via neutron radiography. *Industrial and Engineering Chemistry Research*, 52, pp. 17263–17269.

[88] Olujić, Ž. and Jansen, H. 2015. Large-diameter experimental evidence on liquid (mal)distribution properties of structured packings. *Chemical Engineering Research and Design*, 99, pp. 2–13.

[89] Hu, J., Yang, X., Yu, J. and Dai, G. 2014. Numerical simulation of carbon dioxide (CO_2) absorption and interfacial mass transfer across vertically wavy falling film. *Chemical Engineering Science*, 116, pp. 243–253.

[90] Haroun, Y., Legendre, D. and Raynal, L. 2010. Direct numerical simulation of reactive absorption in gas-liquid flow on structured packing using interface capture method. *Chemical Engineering Science*, 65, pp. 351–356.

[91] Haroun, Y., Legendre, D. and Raynal, L. 2010. Volume of fluid method for interfacial reactive mass transfer: Application to stable liquid film. *Chemical Engineering Science*, 65, pp. 2896–2909.

[92] Haelssig, J.B., Tremblay, A.Y., Thibault, J. and Etemad, S.G. 2010. Direct numerical simulation of interphase heat and mass transfer in multicomponent vapour-liquid flows. *International Journal of Heat and Mass Transfer*, 53, pp. 3947–3960.

[93] Said, W., Nemer, M. and Clodic, D. 2011. Modeling of dry pressure drop for fully developed gas flow in structured packing using CFD simulations. *Chemical Engineering Science*, 66, pp. 2107–2117.

[94] Larachi, F., Petre, C.F., Iliuta, I. and Grandjean, B. 2003. Tailoring the pressure drop of structured packings through CFD simulations. *Chemical Engineering and Processing: Process Intensification*, 42, pp. 535–541.

[95] Hosseini, S.H., Shojaee, S., Ahmadi, G. and Zivdar, M. 2012. Computational fluid dynamics studies of dry and wet pressure drops in structured packings. *Journal of Industrial and Engineering Chemistry*, 18, pp. 1465–1473.

[96] Fernandes, J., Simões, P.C., Mota, J.P.B. and Saatdjian, E. 2008. Application of CFD in the study of supercritical fluid extraction with structured packing: Dry pressure drop calculations. *Journal of Supercritical Fluids*, 47, pp. 17–24.

[97] Armstrong, L.M., Gu, S. and Luo, K.H. 2013. Dry pressure drop prediction within Montz-Pak B1-250.45 packing with varied inclination angles and geometries. *Industrial and Engineering Chemistry Research*, 52, pp. 4372–4378.

[98] Owens, S.A., Perkins, M.R. and Eldridge, R.B. 2013. Computational fluid dynamics simulation of structured packing. *Industrial and Engineering Chemistry Research*, 52, pp. 2032–2045.

[99] Ding, H., Li, J., Xiang, W. and Liu, C. 2015. CFD simulation and optimization of Winpak-based modular catalytic structured packing. *Industrial and Engineering Chemistry Research*, 54, pp. 2391–2403.

[100] Lautenschleger, A., Olenberg, A. and Kenig, E.Y. 2015. A systematic CFD-based method to investigate and optimise novel structured packings. *Chemical Engineering Science*, 122, pp. 452–464.

[101] Zivdar, M., Fard, M.H. and Prince, R.G.H. 2006. Evaluation of pressure drop and mass-transfer characteristics of a structured packing for production and separation of food flavours. *Food and Bioproducts Processing*, 84, pp. 200–205.

[102] Zakeri, A., Einbu, A. and Svendsen, H.F. 2012. Experimental investigation of pressure drop in structured packings. *Chemical Engineering Science*, 73, pp. 285–298.

[103] Rix, A. and Olujic, Z. 2008. Pressure drop of internals for packed columns. *Chemical Engineering and Processing*, 47, pp. 1520–1529.

[104] Boccardo, G., Augier, F., Haroun, Y., Ferré, D. and Marchisio, D.L. 2015. Validation of a novel open-source work-flow for the simulation of packed-bed reactors. *Chemical Engineering Journal*, 279, pp. 809–820.

[105] Fernandes, J., Lisboa, P.F., Simões, P.C., Mota, J.P.B. and Saatdjian, E. 2009. Application of CFD in the study of supercritical fluid extraction with structured packing: Wet pressure drop calculations. *Journal of Supercritical Fluids*, 50, pp. 61–68.

[106] Fourati, M., Roig, V. and Raynal, L. 2013. Liquid dispersion in packed column: Experiments and numerical modeling. *Chemical Engineering Science*, 100, pp. 266–278.

[107] Lappalainen, K., Manninen, M. and Alopaeus, V. 2009. CFD modeling of radial spreading of flow in trickle-bed reactors due to mechanical and capillary dispersion. *Chemical Engineering Science*, 64, pp. 207–218.

[108] Lappalainen, K., Gorshkova, E., Manninen, M. and Alopaeus, V. 2011. Characteristics of liquid and tracer dispersion in trickle-bed reactors: Effect on CFD modeling and experimental analyses. *Computers and Chemical Engineering*, 35, pp. 41–49.

[109] Edwards, D.P., Krishnamurthy, K.R. and Potthoff, R.W. 1999. Development of an improved method to quantify maldistribution and its effect on structured packing column performance. *Chemical Engineering Research and Design*, 77, pp. 656–662.

[110] Soulaine, C., Horgue, P., Franc, J. and Quintard, M. 2014. Gas-liquid flow modeling in columns equipped with structured packing. *AIChE Journal*, 60, pp. 3665–3674.

[111] Alekseenko, S.V., Markovich, D.M., Evseev, A.R., Bobylev, A.V., Tarasov, B.V. and Karsten, V.M. 2008. Experimental investigation of liquid distribution over structured packing. *AIChE Journal*, 54, pp. 1424–1430.

[112] Chen, J., Liu, C., Yuan, X. and Yu, G. 2009. CFD simulation of flow and mass transfer in structured packing distillation columns. *Chinese Journal of Chemical Engineering*, 17, pp. 381–388.

[113] Iliuta, I., Petre, C.F. and Larachi, F. 2004. Hydrodynamic continuum model for two-phase flow structured-packing-containing columns. *Chemical Engineering Science*, 59, pp. 879–888.

[114] Rahimpour, M.R., Saidi, M., Baniadam, M. and Parhoudeh, M. 2013. Investigation of natural gas sweetening process in corrugated packed bed column using computational fluid dynamics (CFD) model. *Journal of Natural Gas Science and Engineering*, 15, pp. 127–137.

[115] Pham, D.A., Lim, Y., Jee, H., Ahn, E. and Jung, Y. 2015. Porous media eulerian computational fluid dynamics (CFD) model of amine absorber with structured-packing for CO_2 removal. *Chemical Engineering Science*, 132, pp. 259–270.

[116] Asendrych, D., Niegodajew, P. and Drobniak, S. 2013. CFD modelling of CO_2 capture in a packed bed by chemical absorption. *Chemical and Process Engineering*, 34, pp. 269–282.

[117] Haroun, Y., Raynal, L. and Alix, P. 2014. Prediction of effective area and liquid hold-up in structured packings by CFD. *Chemical Engineering Research and Design*, 92, pp. 2247–2254.

[118] Tsai, R.E., Seibert, A.F., Eldridge, R.B. and Rochelle, G.T. 2009. Influence of viscosity and surface tension on the effective mass transfer area of structured packing. *Energy Procedia*, 1, pp. 1197–1204.

[119] Brinkmann, U., Janzen, A. and Kenig, E.Y. 2014. Hydrodynamic analogy approach for modelling reactive absorption. *Chemical Engineering Journal*, 250, pp. 342–353.

[120] Fei, Y., Black, S., Szuhánszki, J., Ma, L., Ingham, D.B., Stanger, P.J. and Pourkashanian, M. 2015. Evaluation of the potential of retrofitting a coal power plant to oxy-firing using CFD and process co-simulation. *Fuel Processing Technology*, 131, pp. 45–58.

[121] Edge, P.J., Heggs, P.J., Pourkashanian, M. and Stephenson, P.L. 2013. Integrated fluid dynamics-process modelling of a coal-fired power plant with carbon capture. *Applied Thermal Engineering*, 60, pp. 242–250.

[122] Lewis, W.K. and Whitman, W.G. 1924. Principles of gas absorption. *Industrial and Engineering Chemistry*, 16, pp. 1215–1220.

[123] Higbie, R. 1935. The rate of absorption of a pure gas into a still liquid during short periods of time. *Transactions of the American Institute of Chemical Engineers*, 31, pp. 365–389.

[124] Danckwerts, P.V. 1979. The reaction of CO_2 with ethanolamines. *Chemical Engineering Science*, 34, pp. 443–446.

[125] Perlmutter, D.D. 1961. Surface-renewal models in mass transfer. *Chemical Engineering Science*, 16, pp. 287–296.

[126] Wang, M.H., Ledoux, A. and Estel, L. 2013. Oxygen solubility measurements in a MEA/H_2O/CO_2 mixture. *Journal of Chemical and Engineering Data*, 58, pp. 1117–1121.

[127] Ramazani, R., Mazinani, S., Hafizi, A. and Jahanmiri, A. 2015. Equilibrium solubility of carbon dioxide in aqueous blend of monoethanolamine (MEA) and 2-1-piperazinyl-ethylamine (PZEA) solutions: Experimental and optimization study. *Process Safety and Environmental Protection*, 98, pp. 325–332.

[128] Ostonen, A., Ojala, L.S., Uusi-Kyyny, P., Penttilä, A. and Alopaeus, V. 2015. A comprehensive study of CO_2 solubility in aqueous 2-HEAA and MEA + 2-HEAA solutions – Measurements and modeling. *International Journal of Greenhouse Gas Control*, 42, pp. 296–306.

[129] Nouacer, A., Belaribi, F.B., Mokbel, I. and Jose, J. 2014. Solubility of carbon dioxide gas in some 2.5 M tertiary amine aqueous solutions. *Journal of Molecular Liquids*, 190, pp. 68–73.

[130] Chung, P.Y., Soriano, A.N., Leron, R.B. and Li, M.H. 2010. Equilibrium solubility of carbon dioxide in the amine solvent system of (triethanolamine + piperazine + water). *Journal of Chemical Thermodynamics*, 42, pp. 802–807.

[131] Tong, C., Perez, C.C., Chen, J., Marcos, J.C.V., Neveux, T. and Le Moullec, Y. 2013. Measurement and calculation for CO_2 solubility and kinetic rate in aqueous solutions of two tertiary amines. *Energy Procedia*, 37, pp. 2084–2093.

[132] Hamzehie, M.E., Fattahi, M., Najibi, H., Van der Bruggen, B. and Mazinani, S. 2015. Application of artificial neural networks for estimation of solubility of acid gases (H_2S and CO_2) in 32 commonly ionic liquid and amine solutions. *Journal of Natural Gas Science and Engineering*, 24, pp. 106–114.

[133] Uyan, M., Sieder, G., Ingram, T. and Held, C. 2015. Predicting CO_2 solubility in aqueous N-methyldiethanolamine solutions with ePC-SAFT. *Fluid Phase Equilibria*, 393, pp. 91–100.

[134] Baygi, S.F. and Pahlavanzadeh, H. 2015. Application of the perturbed chain-SAFT equation of state for modeling CO_2 solubility in aqueous monoethanolamine solutions. *Chemical Engineering Research and Design*, 93, pp. 789–799.

[135] Cheng, M.D., Caparanga, A.R., Soriano, A.N. and Li, M.H. 2010. Solubility of CO_2 in the solvent system (water + monoethanolamine + triethanolamine). *The Journal of Chemical Thermodynamics*, 42, pp. 342–347.

[136] Jiru, Y., Eimer, D.A. and Wenjuan, Y. 2012. Measurements and correlation of physical solubility of carbon dioxide in (monoethanolamine + water) by a modified technique. *Industrial and Engineering Chemistry Research*, 51, pp. 6958–6966.

[137] Monteiro, J.G.M.-S. and Svendsen, H.F. 2015. The N_2O analogy in the CO_2 capture context: Literature review and thermodynamic modelling considerations. *Chemical Engineering Science*, 126, pp. 455–470.

[138] Penttilä, A., Dell'Era, C., Uusi-Kyyny, P. and Alopaeus, V. 2011. The Henry's law constant of N_2O and CO_2 in aqueous binary and ternary amine solutions (MEA, DEA, DIPA, MDEA, and AMP). *Fluid Phase Equilibria*, 311, pp. 59–66.

[139] Gervasi, J., Dubois, L. and Thomas, D. 2014. Screening tests of new hybrid solvents for the post-combustion CO_2 capture process by chemical absorption. *Energy Procedia*, 63, pp. 1854–1862.

[140] Aines, R.D., Spaddaccini, C.M., Duoss, E.B., Stolaroff, J.K., Vericella, J., Lewis, J.A. and Farthing, G. 2013. Encapsulated solvents for carbon dioxide capture. *Energy Procedia*, 37, pp. 219–224.

[141] Vega, F., Navarrete, B., Cano, M. and Portillo, E. 2014. Development of partial oxy-combustion technology: New solvens applied to CO_2 capture in fossil-fuels power plants. *Energy Procedia*, 63, pp. 484–489.

[142] Ye, Q., Wang, X. and Lu, Y. 2015. Screening and evaluation of novel biphasic solvents for energy-efficient post-combustion CO_2 capture. *International Journal of Greenhouse Gas Control*, 39, pp. 205–214.

[143] Kay, J.P., Jensen, M.D. and Fiala, N.J. 2014. Pilot-scale evaluations of advanced solvents for postcombustion CO_2 capture. *Energy Procedia*, 63, pp. 1903–1910.

[144] Mangalapally, H.P., Notz, R., Asprion, N., Sieder, G., Garcia, H. and Hasse, H. 2012. Pilot plant study of four new solvents for post combustion carbon dioxide capture by reactive absorption and comparison to MEA. *International Journal of Greenhouse Gas Control*, 8, pp. 205–216.

[145] von Harbou, I., Mangalapally, H.P. and Hasse, H. 2013. Pilot plant experiments for two new amine solvents for post-combustion carbon dioxide capture. *International Journal of Greenhouse Gas Control*, 18, pp. 305–314.

[146] Halim, H.N.A., Shariff, A.M. and Bustam, M.A. 2015. High pressure CO_2 absorption from natural gas using piperazine promoted 2-amino-2-methyl-1-propanol in a packed absorption column. *Separation and Purification Technology*, 152, pp. 87–93.

[147] Caplow, M. 1968. Kinetics of carbamate formation and breakdown. *Journal of the American Chemical Society*, 90, pp. 6795–6803.

[148] Crooks, J.E. and Donnellan, J.P. 1989. Kinetics and mechanism of the reaction between carbon dioxide and amines in aqueous solution. *Journal of the Chemical Society, Perkin Transactions*, 2, pp. 331–333.

[149] Xiao, J., Li, C.W. and Li, M.H. 2000. Kinetics of absorption of carbon dioxide into aqueous solutions of 2-amino-2-methyl-1-propanol + monoethanolamine. *Chemical Engineering Science*, 55, pp. 161–175.

[150] Littel, R.J., Versteeg, G.F. and Van Swaaij, W.P.M. 1992. Kinetics of CO_2 with primary and secondary amines in aqueous solutions – I. Zwitterion deprotonation kinetics for DEA and DIPA in aqueous blends of alkanolamines. *Chemical Engineering Science*, 47, pp. 2027–2035.

[151] Han, B., Sun, Y., Fan, M. and Cheng, H. 2013. On the CO_2 capture in water-free monoethanolamine solution: An ab-inition molecular dynamics study. *The Journal of Physical Chemistry*, 117, pp. 5971–5977.

[152] Xie, H.B., Zhou, Y., Zhang, Y. and Johnson, J.K. 2010. Reaction mechanism of monoethanolamine with CO_2 in aqueous solution from molecular modeling. *The Journal of Physical Chemistry*, 114, pp. 11844–11852.

[153] Versteeg, G.F., van Dijck, L.A.J. and van Swaaij, W.P.M. 1996. On the kinetics between CO_2 and alkanolamines both in aqueous and non-aqueous solutions. An overview. *Chemical Engineering Communications*, 144, pp. 113–158.

[154] da Silva, E.F. and Svendsen, H.F. 2004. Ab initio study of the reaction of carbamate formation from CO_2 and alkanolamines. *Industrial and Engineering Chemistry Research*, 43, pp. 3413–3418.

[155] Aboudheir, A., Tontiwachwuthikul, P., Chakma, A. and Idem, R. 2003. Kinetics of the reactive absorption of carbon dioxide in high CO_2-loaded concentrated aqueous monoethanolamine solutions. *Chemical Engineering Science*, 58, pp. 5195–5210.

[156] Kale, C., Górak, A. and Schoenmakers, H. 2013. Modelling of the reactive absorption of CO_2 using mono-ethanolamine. *International Journal of Greenhouse Gas Control*, 17, pp. 294–308.

[157] Faramarzi, L., Kontogeorgis, G.M., Michelsen, M.L., Thomsen, K. and Stenby, E.H. 2010. Absorber model for CO_2 capture by monoethanolamine. *Industrial and Engineering Chemistry Research*, 49, pp. 3751–3759.

[158] Gaspar, J. and Fosbøl, P.L. 2015. A general enhancement factor model for absorption and desorption systems: A CO_2 capture case-study. *Chemical Engineering Science*, 138, pp. 203–215.

[159] Hamborg, E.S. and Versteeg, G.F. 2012. Absorption and desorption mass transfer rates in chemically enhanced reactive systems. Part I: Chemical enhancement factors. *Chemical Engineering Journal*, 188–189, pp. 555–560.

[160] Etemad, E., Ghaemi, A. and Shirvani, M. 2015. Rigorous correlation for CO_2 mass transfer flux in reactive absorption processes. *International Journal of Greenhouse Gas Control*, 42, pp. 288–295.

[161] Kucka, L., Müller, I., Kenig, E.Y. and Górak, A. 2003. On the modelling and simulation of sour gas absorption by aqueous amine solutions. *Chemical Engineering Science*, 58, pp. 3571–3578.

[162] Wilcox, J., Rochana, P., Kirchofer, A., Glatz, G. and He, J. 2014. Revisiting film theory to consider approaches for enhanced solvent-process design for carbon capture. *Energy and Environmental Science*, 7, pp. 1769–1785.

[163] Wang, Y., Shu, C. and Yang, L.M. 2015. An improved multiphase lattice Boltzmann flux solver for three-dimensional flows with large density ratio and high Reynolds number. *Journal of Computational Physics*, 302, pp. 41–58.

[164] Cooke, J.J., Armstrong, L.M., Luo, K.H. and Gu, S. 2014. Adaptive mesh refinement of gas-liquid flow on an inclined plane. *Computers and Chemical Engineering*, 60, pp. 297–306.

[165] Youngs, D.L. 1982. Time-dependent multi-material flow with large fluid distortion. In: Morton, K.W. and Baines, M.J. (eds.) *Numerical Methods for Fluid Dynamics*. New York: Academic. pp. 273–285.

[166] Kothe, D.B., Mjolsness, R.C. and Torrey, M.D. 1991. RIPPLE: a computer program for incompressible flows with free surfaces. *Los Alamos National Laboratory Rep*. LA–12007–MS.

[167] Rudman, M. 1997. Volume-tracking methods for interfacial flow calculations. *International Journal for Numerical Methods in Fluids*, 24, pp. 671–691.

[168] Brackbill, J.U., Kothe, D.B. and Zemach, C. 1992. A continuum method for modelling surface tension. *Journal of Computational Physics*, 100, pp. 335–354.

[169] Treybal, R.E. 1981. *Mass Transfer Operations*. 3rd edition. Singapore: McGraw-Hill.

[170] Sobieszuk, P. and Pohorecki, R. 2010. Gas-side mass transfer coefficients in a falling film microreactor. *Chemical Engineering and Processing*, 49, pp. 820–824.

[171] Haroun, Y., Raynal, L. and Legendre, D. 2012. Mass transfer and liquid hold-up determination in structured packing by CFD. *Chemical Engineering Science*, 75, pp. 342–348.

[172] Xu, Y.Y., Paschke, S., Repke, J.U., Yuan, J.Q. and Wozny, G. 2009. Computational approach to characterize the mass transfer between the counter-current gas-liquid flow. *Chemical Engineering and Technology*, 32, pp. 1227–1235.

[173] Yu, L.M., Zeng, A.W. and Yu, K.T. 2006. Effect of interfacial velocity fluctuations on the enhancement of the mass-transfer process in falling-film flow. *Industrial and Engineering Chemistry Research*, 45, 1201–1210.

[174] van Krevelen, D.W. and Hoftijzer, P.J. 1948. Kinetics of gas-liquid reactions. Part I: General theory. *Recueil des Travaux Chimiques des Pays-Bas*, 67, pp. 563–586.

[175] Hikita, H. and Asai, S. 1964. Gas absorption with (m, n)th order irreversible chemical reaction. *International Journal of Chemical Engineering*, 9, pp. 332–340.

[176] Sema, T., Naami, A., Fu, K., Edali, M., Liu, H., Shi, H., Liang, Z., Idem, R. and Tontiwachwuthikul, P. 2012. Comprehensive mass transfer and reaction kinetics studies of CO_2 absorption into aqueous solutions of blended MDEA-MEA. *Chemical Engineering Journal*, 209, pp. 501–512.

[177] Wilke, C.R. and Chang, P. 1955. Correlation of diffusion coefficients in dilute solutions. *AIChE Journal*, 1, pp. 264–270.

[178] Nusselt, W. 1916. Die Oberflächenkondensation des Wasserdampfes. *Zeitschrift des Vereines Deutscher Ingenieure*, 60, 541–546.

[179] Olujić, Ž. 1999. Effect of column diameter on pressure drop of a corrugated sheet structured packing. *Chemical Engineering Research and Design*, 77, 505–510.

[180] Blottner, F.G. 1990. Accurate Navier-Stokes results for the hypersonic flow over a spherical nosetip. *AIAA Journal of Spacecraft and Rockets*, 27, pp. 113–122.

[181] Roache, P.J. 1998. *Verification and validation in computational Science and engineering*. Albuquerque, New Mexico: Hermosa.

[182] Roache P.J., 1994. Perspective: A method for uniform reporting of grid refinement studies. *ASME Journal of Fluids Engineering*, 116, pp. 405–413.

[183] Richardson L.F., 1910. The approximate arithmetical solution by finite differences of physical problems involving differential equations, with an application to stresses in a masonry dam. *Transactions of the Royal Society of London*, 210, pp. 307–357.

[184] Ali, M.S.M., Doolan, C.J. and Wheatley, V. 2009. *Editors: Witt, P.J. and Schwarz, M.P.* Grid convergence study for a two-dimensional simulation of flow around a square cylinder at a low Reynolds number. *Conference proceedings of the 7th International Conference on CFD in the Minerals and Process Industries. Melbourne, Australia. 9–11 December*. CSIRO, pp. 1–6.

[185] Mehta U. 1998. Credible computational fluid dynamics simulations. *AIAA Journal*, 36, pp. 665–667.

[186] Benek J.A. and Kraft E.M, 1994. A method for uniform reporting of grid refinement studies. *ASME Journal of Fluids Engineering*, 116, pp. 405–413.

[187] Sindir M.M., Barson, S.L., Chan, D.C. and Lin, W.H. 1996. On the development and demonstration of a code validation process for industrial applications. *Conference proceedings of the 27th AIAA Fluid Dynamics Conference. New Orleans, Louisina. 17–20 June*.

[188] Coleman, H.W. and Stern, F. 1997. Uncertainties and CFD code validation. *ASME Journal of Fluids Engineering*, 119, 795–803.

[189] Hoffmann, A., Ausner, I., Repke, J.U. and Wozny, G. 2004. Fluid dynamics in multiphase distillation processes in packed towers. *Computer Aided Chemical Engineering*, 18, pp. 199–204.

[190] Hoffmann, A., Ausner, I., Repke, J.U. and Wozny, G. 2006. Detailed investigation of multiphase (gas-liquid and gas-liquid-liquid) flow behavior on inclined plates. *Chemical Engineering Research and Design*, 84, pp. 147–154.

[191] Iso, Y. and Chen, X. 2011. Development of numerical prediction of liquid film flows on packing elements in absorbers. *IHI Engineering Review*, 44, pp. 1–8.

[192] Zogg, M. 1972. Modified mass transfer coefficients for reasonable mass transfer calculations on laminar falling films. *Chemie Ingenieur Technik*, 44, pp. 930–936.

[193] Emmert, R.E. and Pigford, R.L. 1954. A study of gas absorption in falling liquid films. *Chemical Engineering Progress*, 50, pp. 87–93.

[194] Nicolaiewski, E.M.A. and Fair, J.R. 1999. Liquid flow over textured surfaces. 1. Contact angles. *Industrial and Engineering Chemistry Research*, 38, pp. 284–291.

[195] Shi, M.G. and Mersmann, A. 1985. Effective interfacial area in packed columns. *German Chemical Engineering*, 8, pp. 87–96.

[196] Liu, G.B., Yu, K.T., Yuan, X.G., Liu, C.J. and Guo, Q.C. 2006. Simulations of chemical absorption in pilot-scale and industrial-scale packed columns by computational mass transfer. *Chemical Engineering Science*, 61, pp. 6511–6529.

[197] Meldon, J.H. and Morales-Cabrera, M.A. 2011. Analysis of carbon dioxide absorption in and stripping from aqueous monoethanolamine. *Chemical Engineering Journal*, 171, pp. 753–759.

[198] Bradtmöller, C., Janzen, A., Crine, M., Toye, D., Kenig, E.Y. and Scholl, S. 2015. Influence of viscosity on liquid flow inside structured packings. *Industrial and Engineering Chemistry Research*, 54, pp. 2803–2815.

[199] Olujić, Ž., Jansen, H., Kaibel, B., Rietfort, T. and Zich, E. 2001. Stretching the capacity of structured packings. *Industrial and Engineering Chemistry Research*, 40, pp. 6172–6180.

[200] Maćkowiac, J. 1991. Pressure drop in irrigated packed columns. *Chemical Engineering and Processing: Process Intensification*, 29, pp. 93–105.

[201] Siminiceanu, I., Friedl, A. and Dragan, M. 2002. A simple equation for the effective mass transfer area of the Mellapak750Y structured packing. *Conference proceedings of the Scientific Conference Meeting "35 Years of Petroleum-Gas University Activity", Ploiești, Romania.*.

[202] Gualito, J.J., Cerino, F.J., Cardenas, J.C. and Rocha, J.A. 1997. Design method for distillation columns filled with metallic, ceramic or plastic structured packings. *Industrial and Engineering Chemistry Research*, 36, pp. 1747–1757.

[203] Bravo, J.L. and Fair, J.R. 1982. Generalized correlation for mass transfer in packed distillation columns. *Industrial and Engineering Chemistry Process Design and Development Journal*, 21, pp. 162–170.

[204] Ataki, A. and Bart, H.J. 2006. Experimental and CFD simulation study for the wetting of a structured packing element with liquids. *Chemical Engineering and Technology*, 29, pp. 336–347.

[205] De Brito, M.H., von Stockar, U., Bangerter, A.M., Bomio, P. and Laso, M. 1994. Effective mass-transfer area in a pilot plant column equipped with structured pack-

ings and ceramic rings. *Industrial and Engineering Chemistry Research*, 33, pp. 647–656.

[206] Sidi-Boumedine, R. and Raynal, L. 2005. Influence of the viscosity on the liquid hold-up in trickle-bed reactors with structured packings. *Catalysis Today*, 105, pp. 673–679.

[207] Rizzuti, L., Augugliaro, V. and Cascio, G.L. 1981. The influence of the liquid viscosity on the effective interfacial area in packed columns. *Chemical Engineering Science*, 36, pp. 973–978.

[208] Qi, R., Lu, L. and Qin, F. 2014. Model development for the wetted area of falling film liquid desiccant air-conditioning system. *International Journal of Heat and Mass Transfer*, 74, pp. 206–209.

[209] Könözsy, L., Ishmurzin, A., Mayer, F., Grasser, M., Wu, M. and Ludwig, A. 2009. Numerical investigation of grid influence on formation of segregation. *International Journal of Cast Metals Research*, 22, pp. 175–178.